Shock interaction patterns in carbon dioxide nonequilibrium flows over double-wedges

PhD Thesis

Catarina Garbacz

Supervisor: Dr. Marco Fossati

FASTT Lab, Aerospace Center of Excellence

Mechanical and Aerospace Engineering

University of Strathclyde, Glasgow

December 21, 2024

To my partner,

who everyday gives me more

than I could ever imagine possible.

"My main goal in life is to live
in a constant state of flow."
— Frazer Dougan

This thesis is the result of the author's original research. It has been composed by the author and has not been previously submitted for examination which has led to the award of a degree.

The copyright of this thesis belongs to the author under the terms of the United Kingdom Copyright Acts as qualified by University of Strathclyde Regulation 3.50. Due acknowledgment must always be made of the use of any material contained in, or derived from, this thesis.

Abstract

Shock interactions in nonequilibrium hypersonic CO_2-N_2 flows over double-wedge geometries are investigated in detail. Flow patterns resulting from shock interactions typically lead to shock impingement phenomena, which is characterized by localised high heating and pressure loads acting on the surface. Accurately predicting the flow physics involved in shock wave interference and associated surface loads is key to ensure the robust aerodynamic design of high-speed vehicles. While extensive research on shock interactions in air flows can be found in the literature, investigation of carbon-dioxide flows is scarce. This thesis aims to address the need for a thorough understanding of nonequilibrium shock interaction physics in the Martian atmosphere, driven by the growing interest of the aerospace community in exploring the planet.

Hypersonic vehicles operate in unique flow environments that are dominated by chemical and thermodynamic phenomena not observed at lower Mach numbers. Accurate simulation of these environments requires complex physical and numerical models to capture physical processes occurring the atomic scale that have a significant impact on surface flow properties. In this work, shock interaction patterns in nonequilibrium CO_2-N_2 flows are investigated by means of computational fluid dynamics. A coupled framework for simulating nonequilibrium hypersonic flows with any gas mixture is implemented by linking the SU2-NEMO software, a hypersonic CFD code, to the Mutation++ library, that provides thermodynamic, transport, chemistry, and energy transfer models, data, and algorithms allowing for the closure of the Navier-Stokes flow equations implemented in the CFD code. Park's two-temperature model is considered to model vibrational relaxation and finite-rate chemistry.

Patterns of shock interaction are characterised on the basis of Edney's pioneer classification. Results show that vibrational relaxation plays an active role in the mechanisms of shock interference for carbon-dioxide dominated flows, since the assumptions of simplified models (perfect

ideal and thermally perfect gas models) resulted in significant differences in terms of qualitative flow patterns as well as distributions of surface aerothermal loads. It is shown that the effect of decreasing the freestream Mach number on the pattern of shock interaction and surface properties follows the same trend resulting from increasing the angle of the second wedge and from simulating the flow with a gas model where less energy is absorbed by vibrational excitation, and contrary to the trend resulting from increasing the freestream temperature: flow separation regions and shock angles become larger, leading to more complex and stronger mechanisms of interaction. Results indicate there is a threshold of the Mach number and aft wedge angle below which, and above which, respectively, the flow becomes unsteady due to a strong coupling between the separated flow region and the entire shock system. Accounting for vibrational relaxation effects shows to stabilize the entire shock system, by delaying the threshold for which the mechanism of interaction would become unsteady if vibrational excitation were to be neglected. Conversely, the opposite trend is seen for when thermal equilibrium is assumed.

Contents

Abstract ii

List of Figures vi

List of Tables xiii

Nomenclature xv

Acknowledgments xix

1 Introduction 1

1.1 Context 1

1.2 Motivation, aim and research questions 8

1.3 Thesis layout 11

1.4 Publications related to the thesis 12

2 Literature review 15

2.1 Shock interaction patterns 15

2.2 Unsteady mechanisms of interaction 17

2.3 Impact of the physical model 18

2.4 Carbon dioxide flows 21

3 Modelling of nonequilibrium hypersonic flows 25

3.1 Physical modelling 25

3.1.1 Kinetic theory of gases 25

3.1.2 Governing equations 30

3.2 Numerical modelling 36

4 Inviscid shock interactions **40**

4.1 Domain, boundary conditions and simulation parameters 41

4.2 Grid independence studies 42

4.3 Impact of the freestream temperature 44

4.4 Nonequilibrium effects 51

5 Viscous laminar shock interactions **60**

5.1 Domain, boundary conditions and simulation parameters 61

5.2 Grid independence studies 62

5.3 Role of vibrational relaxation 65

5.3.1 Thermal equilibrium models 66

5.3.2 Nonequilibrium shock interaction patterns 67

5.3.3 Thermal nonequilibrium effects 71

5.3.4 Thermal equilibrium shock interaction patterns 74

5.4 Effect of Mach number 90

5.4.1 Shock pattern characterization for varying freestream Mach number . . 91

5.4.2 Thermal nonequilibrium effects 110

6 Final Remarks **114**

6.1 Summary of the numerical analysis 115

6.2 Conclusions 115

6.3 Future work 121

A SU2-NEMO and mutation++ library **123**

B Anisotropic mesh adaptation **125**

C Code validation **127**

C.1 Zero-dimensional thermal bath 127

C.2 Cylinder 129

C.3 Shock wave boundary layer interaction 132

C.4 Proximal cylinders 135
C.5 Proximal spheres 138
C.6 Free-flying ring 139
C.7 Bedford wing-body 140
C.8 Wedge 143
C.9 Double-cone 146

Bibliography **148**

List of Figures

1.1 Inviscid generic schematic of a hypersonic flow over a double-wegde. 2
1.2 Classification of shock interaction patterns by Edney. Adapted from [5]. 3
1.3 Shock-boundary layer interaction patterns. 4

3.1 Internal energy modes of the CO_2 molecule. 26
3.2 Diagram for the energy levels of the different thermal modes [74]. Index *i* refers to chemical species. 27
3.3 Different energy states according to molecular orientation [74]. 28

4.1 Double-wedge geometry, computational domain and boundary conditions. . . . 41
4.2 Original (left) and final adapted (right) mesh for the air-5 case with $T_\infty = 1000$ K. 44
4.3 Grid convergence plots for the nonequilibrium air-5 case with $T_\infty = 300$ K. . . 45
4.4 Grid convergence plots for the nonequilibrium air-5 case with $T_\infty = 1000$ K. . . 45
4.5 Grid convergence plots for the air case with a PIG model. 45
4.6 Grid convergence plots for the nonequilibrium CO_2-N_2 case with $T_\infty = 300$ K. 46
4.7 Grid convergence plots for the nonequilibrium CO_2-N_2 case with $T_\infty = 1000$ K. 46
4.8 Grid convergence plots for the CO_2-N_2 case with a PIG model. 46
4.9 Nonequilibrium air-5 flow over the 15°-45° double-wedge. Normalized pressure p/p_∞ (left), numerical schlieren (right); From top to bottom: $T_\infty = 300$ K, $T_\infty = 1000$ K. 48
4.10 Nonequilibrium air-5 flow over the 15°-45° double-wedge. Normalized pressure p/p_∞ and streamlines for $T_\infty = 300$ K. 48

4.11 Schematics of inviscid shock interaction patterns obtained for the nonequilibrium cases. 49
4.12 Nonequilibrium CO_2-N_2 flow over the 15°-45° double-wedge. Normalized pressure p/p_∞ (left), numerical schlieren (right); From top to bottom: $T_\infty = 300$ K, $T_\infty = 1000$ K. 50
4.13 Comparison of normalized surface pressure profiles for inviscid shock interactions. 51
4.14 Air (left) and CO_2-N_2 (right) flows over the 15°-45° double-wedge: normalized temperature contours; From top to bottom: PIG, $T_\infty = 300$ K, $T_\infty = 1000$ K. . . 52
4.15 Schematic of the inviscid nine-shock type V interaction pattern. 53
4.16 Air (left) and CO_2-N_2 (right) flows over the 15°-45° double-wedge: degree of thermal nonequilibrium; From top to bottom: $T_\infty = 300$ K, $T_\infty = 1000$ K. . . . 54
4.17 Air flow over the 15°-45° double-wedge: O (left) and NO (right) mass fraction contours; From top to bottom: $T_\infty = 300$ K, $T_\infty = 1000$ K. 56
4.18 CO_2-N_2 flow over the 15°-45° double-wedge: O (left) and CO (right) mass fraction contours, with $T_\infty = 1000$ K. 57

5.1 Zoomed views, in the corner between the two wedges, of the original (left) and final adapted (right) hybrid grids for the 15°-50°case simulated with a thermally perfect gas model. 63
5.2 Grid convergence plots for the 15°-50°case with the thermally perfect gas model. 64
5.3 Variation of specific heat at constant volume C_v and specific heat ratio γ of a CO_2:0.97, N_2:0.03 mixture with temperature for a thermally perfect gas model. 67
5.4 Numerical schlieren (left) and schematics (right) for shock interaction patterns obtained with a two-temperature model. 68
5.5 Comparison of surface aerothermal loads obtained with a two-temperature model for the different double-wedge geometries: (a) normalized pressure distribution, (b) heat flux distribution. 69
5.6 Degree of thermal nonequilibrium obtained for all geometries: 15°-40°, 15°-45°, 15°-50° and 15°-55° double-wedge. 72

5.7 Comparison of density gradients and shock interaction schematics obtained for a CO_2-N_2 flow over the 15°-40° double-wedge: perfect ideal gas (left), thermally perfect gas (middle) and nonequilibrium gas (right). 74
5.8 Comparison of surface aerothermal loads of (a) normalized pressure and (b) heat flux, for the 15°-40° double-wedge: perfect ideal gas, thermally perfect gas and nonequilibrium gas model. Green arrows indicate separation points. . . 75
5.9 Comparison of density gradients and shock interaction schematics obtained for a CO_2-N_2 flow over the 15°-45° double-wedge: perfect ideal gas (left), thermally perfect gas (middle) and nonequilibrium gas (right). 78
5.10 Comparison of surface aerothermal loads of (a) normalized pressure and (b) heat flux, for the 15°-45° double-wedge: perfect ideal gas, thermally perfect gas and nonequilibrium gas model. Green arrows indicate separation points. . . 78
5.11 Comparison of density gradients and shock interaction schematics obtained for a CO_2-N_2 flow over the 15°-50° double-wedge: perfect ideal gas (left), thermally perfect gas (middle) and nonequilibrium gas (right). 81
5.12 Comparison of surface aerothermal loads of (a) normalized pressure and (b) heat flux, for the 15°-50° double-wedge: perfect ideal gas, thermally perfect gas and nonequilibrium gas model. Green arrows indicate separation points. . . 81
5.13 Unsteady density gradients and shock interaction schematics obtained for a CO_2-N_2 flow over the 15°-55° double-wedge with a perfect ideal gas model. . . 84
5.14 Instant surface aerothermal loads for the 15°-55° double-wedge with a perfect ideal gas model: (a) normalized pressure distribution, (b) heat flux distribution. 85
5.15 Comparison of density gradients and shock interaction schematics obtained for a CO_2-N_2 flow over the 15°-55° double-wedge: thermally perfect gas (left) and nonequilibrium gas (right). 85
5.16 Comparison of surface aerothermal loads of (a) normalized pressure and (b) heat flux, for the 15°-55° double-wedge: perfect ideal gas (time averaged), thermally perfect gas and nonequilibrium gas model. Green arrows indicate separation points. 86

5.17 Contours of Mach number (top) and difference between translational and vibrational temperatures (bottom) for a CO_2-N_2 flow over the 15°-40°double-wedge with $M_\infty = 11$, $M_\infty = 9$ and $M_\infty = 7$. 92
5.18 Comparison of Mach number contour lines for different values of freestream Mach (7, 9, 11) for the 15°-40°geometry (left). Contours of pressure for a CO_2-N_2 flow over the 15°-40°double-wedge with $M_\infty = 7$ (right). 92
5.19 Comparison of surface quantities distribution for different freestream Mach numbers for the 15°-40°geometry. Normalised pressure (left), Stanton number (right). 94
5.20 Compression corner detailed view of the 15°-40°double-wegde with $M_\infty = 11$: translational temperature with sonic line. 96
5.21 Detailed analysis of translational and vibrational heat flux contributions (left) and temperatures (right) along the surface of the second wedge, for the 15°-40°double-wedge with $M_\infty = 11$. 96
5.22 Contours of Mach number (top) and difference between translational and vibrational temperatures (bottom) for a CO_2-N_2 flow over the 15°-45°double-wedge with $M_\infty = 11$, $M_\infty = 9$ and $M_\infty = 7$. White regions in the bottom row represent thermal equilibrium. Reproduced with permission from AIAA AVIATION Forum (2022). Copyright 2022 by the American Institute of Aeronautics and Astronautics [7]. 97
5.23 Comparison of Mach number contour lines for different values of freestream Mach (7, 9, 11) for the 15°-45°geometry.Reproduced with permission from AIAA AVIATION Forum (2022). Copyright 2022 by the American Institute of Aeronautics and Astronautics [7]. 98
5.24 Comparison of surface quantities distribution for different freestream Mach numbers for the 15°-45°geometry. Normalised pressure (left), Stanton number (right). Reproduced with permission from AIAA AVIATION Forum (2022). Copyright 2022 by the American Institute of Aeronautics and Astronautics [7]. 99

5.25 Contours of Mach number (top), difference between translational and vibrational temperatures (bottom) and pressure (bottom) for a CO_2-N_2 flow over the 15°-50°double-wedge with $M_\infty = 11$, $M_\infty = 9$ and $M_\infty = 7$. White regions in the bottom row represent thermal equilibrium. 100

5.26 Comparison of Mach number contour lines for different values of freestream Mach (7, 9, 11) for the 15°-50°geometry (left). Detailed view of the shock interaction region for the 15°-50°double-wegde with $M_\infty = 11$ (middle – translational temperature, right – pressure). 101

5.27 Comparison of surface quantities distribution for different freestream Mach numbers for the 15°-50°geometry. Normalised pressure (left), Stanton number (right). 103

5.28 Contours of Mach number (top) and difference between translational and vibrational temperatures (bottom) for a CO_2-N_2 flow over the 15°-55°double-wedge with $M_\infty = 11$ and $M_\infty = 9$. White regions in the bottom row represent thermal equilibrium. Reproduced with permission from AIAA AVIATION Forum (2022). Copyright 2022 by the American Institute of Aeronautics and Astronautics [7]. 104

5.29 Contours of Mach number for a CO_2-N_2 with $M_\infty = 7$ flow over the 15°-55°double-wedge. Reproduced with permission from AIAA AVIATION Forum (2022). Copyright 2022 by the American Institute of Aeronautics and Astronautics [7]. 104

5.30 Types of shock reflection found in the type V interaction pattern: RR at the left and MR at the right. 105

5.31 Comparison of Mach number contour lines for different values of freestream Mach (9, 11) for the 15°-45°geometry. Reproduced with permission from AIAA AVIATION Forum (2022). Copyright 2022 by the American Institute of Aeronautics and Astronautics [7]. 106

5.32 Close-up in the region of main interaction: $M_\infty = 11$ (top) and $M_\infty = 9$ (bottom) for a CO_2-N_2 flow over the 15°-55°double-wedge. Reproduced with permission from AIAA AVIATION Forum (2022). Copyright 2022 by the American Institute of Aeronautics and Astronautics [7]. 107
5.33 Instantaneous surface quantities distribution for the $M_\infty = 7$ flow over the 15°-55°geometry. Normalised pressure (left), Stanton number (right). Reproduced with permission from AIAA AVIATION Forum (2022). Copyright 2022 by the American Institute of Aeronautics and Astronautics [7]. 108
5.34 Comparison of surface quantities distribution for different freestream Mach numbers for the 15°-55°geometry. For $M_\infty = 7$, the time average is plotted. Normalised pressure (left), Stanton number (right). Reproduced with permission from AIAA AVIATION Forum (2022). Copyright 2022 by the American Institute of Aeronautics and Astronautics [7]. 109

A.1 Overview of the coupling between SU2-NEMO and the Mutation++ library - adapted from [30] 124

C.1 Air-5 thermal bath thermochemical nonequilibrium time-evolution. 128
C.2 Grids overview for the cylinder case [37]. 131
C.3 Surface quantities plot for the cylinder [37]. 131
C.4 Diagram of experimental configuration for axisymmetric shock wave boundary layer interaction [106]. 133
C.5 ASWBLI Mach contours over the compression corner [12]. 134
C.6 Boundary layer profile 6 cm before the compression corner [12]. Comparison with experimental [106] and numerical [107] results. 134
C.7 Normalized surface quantities across compression corner [12]. Comparison with experimental [106] and numerical [107] results. 135
C.8 Geometry configuration of the two-dimensional two-cylinder case [37]. 136
C.9 Anisotropic adapted grid: zoomed view near the aft cylinder [37]. 136
C.10 Temperature contours near the aft cylinder: structured (left) and unstructured mesh (right) [37]. 137

C.11 Lift coefficient of the aft cylinder for a vertical displacement of 0.3 meters [37]. 137
C.12 Drag coefficient of the aft cylinder for a vertical displacement of 0.3 meters [37]. 137
C.13 Geometry configuration of the three-dimensional two-sphere case [37]. 138
C.14 Detailed visualization of the final anisotropic grid used for the two-sphere case [37]. 139
C.15 Schlieren and Mach contours of the two-sphere case for the final grid [37]. . . . 139
C.16 Experimental Schlieren (left) and superposition of experimental and numerical Schlieren in green (right) at the shock-shock interaction region [37]. 140
C.17 Grid adaptation for a ring with 45° angle of attack [113]. 141
C.18 Ring aerodynamic coefficients for different angles of attack [113]. 141
C.19 Bedford wing-body: Section planes for visualisation along X and Y planes [34]. 142
C.20 Schematic of features encountered in the flowfield surrounding the Bedford vehicle [34]. 142
C.21 Original and adapted meshes [34]. 143
C.22 Bedford wing-body Mach number contours at 20deg incidence and Mach 4. Y-axis sections (left), X-axis sections (right) [34]. 144
C.23 Bedford wing-body at Mach 4: comparison of aerodynamic coefficients with wind tunnel data [34]. 144
C.24 Wedge geometry. 145
C.25 Comparison of normalized shock standoff distance between numerical and experimental data. 146
C.26 Geometrical configuration for the double-cone (dimensions in mm). 147
C.27 Contours of Mach number for the CO_2 flow over the double-cone. 149
C.28 Graphical comparison of numerical schlieren contours with experimental data [27]. 149
C.29 Comparison of surface heat flux predictions with experimental data. 150

List of Tables

4.1 Simulation parameters for inviscid shock interactions over the 15°-45° double-wedge. 42
4.2 Number of grid nodes used in the final mesh of each test-case. 44
4.3 Inviscid shock interactions: summary of shock interaction patterns. 59

5.1 Simulation parameters for study I. 61
5.2 Simulation parameters for study II. 62
5.3 Number of grid nodes used in the final mesh of each test-case for study 1. . . . 65
5.4 Number of grid nodes used in the final mesh of each test-case for study II. . . . 65
5.5 Viscous shock interactions, study I: summary of shock interaction patterns. . . 91
5.6 Viscous shock interactions, study II: summary of shock interaction patterns. . . 113

C.1 Air-5 thermal bath initial conditions. 128
C.2 Atomic oxygen percentage at 10^{-8} s. 129
C.3 Freestream and wall values for the cylinder case. 130
C.4 Grid details for the cylinder case. 130
C.5 ASWBLI freestream conditions. 133
C.6 Freestream and wall values of the two-cylinder case. 136
C.7 Freestream and wall values for the two-sphere case. 138
C.8 Grid details for the two-sphere case. 138
C.9 Free-flying ring freestream conditions. 140
C.10 Bedford freestream conditions. 143
C.11 Freestream conditions for the wedge simulation. 145

C.12 Double-cone freestream conditions. 147

Nomenclature

Constants

k_B	Boltzmann constant
R_u	universal gas constant

Roman symbols

a	speed of sound
c	mass fraction
e	energy per unit mass
$\mathbf{F}$	vector of numerical fluxes
g	degeneracy
h	enthalpy per unit mass
J	mass diffusion flux
L	wedge length
M	Mach number , $M = \frac{u}{a}$
N	population distribution of energy level
$\mathbf{n}$	unit normal vector
p	pressure
q	heat flux
Q	partition function
$\mathbf{Q}$	vector of source terms
$\mathbf{R}$	vector of residuals
Re	Reynolds number, $Re = \frac{\rho u L}{\mu}$

St	Stanton number, $St = \frac{q}{\rho_\infty u_\infty C_{p,tr}(T_w - T_{tr})}$
T	temperature
t	time
u	velocity
$\mathbf{U}$	vector of conservative variables
V	Diffusion velocity
Y	mass fraction

Greek symbols

γ	specific heat ratio
δ	normal distance from the wall
ε	chemical species energy
θ	wedge angle
λ	thermal conductivity
μ	viscosity
ρ	density
τ	relaxation time
$\bar{\tau}$	viscous stress tensor
ω	chemical source term
Ω	vibro-electronic energy source term

Subscripts and superscripts

c	convective
$elec$	electronic
j	energy level
k	internal energy mode
rot	rotational
s	species
tr	trans-rotational
tra	translational
v	viscous
ve	vibro-electronic
vib	vibrational
$react$	reaction
∞	freestream

Acknowledgments

The work presented in this thesis would not have been possible without the personal and professional support of many others. First and foremost, I would like to acknowledge my supervisor, Professor Marco Fossati, for trusting me with the opportunity to tackle this challenge and choosing me as the right candidate for a fully-funded PhD on the topic of hypersonic aerodynamics. I thank him for his constant guidance and for keeping a close eye on my progress, for teaching me what it means to produce research work with excellence, for his insistence on attention to detail, for encouraging me to consider alternative and creative solutions to problems, and for giving me the freedom to have my own work structure. His contribution as a supervisor has been remarkable.

I would also like to thank the ACE lab and the MAE department. I had the pleasure to conduct my research work in a joyful environment where collaboration and open scientific discussion are not only encouraged, but also the norm. It was an honor to become part of this bigger picture and leave my footprint on the department's legacy. On a more personal note, I owe a lot of my continued persistence, and mental sanity, to my colleague friends. Their daily presence in my life made the office feel like home and has been the best reminder not to take life too seriously and to never forget to laugh, especially in the most difficult times. There are way too many people to name one by one, but I would like to particularly acknowledge the ones that were there since/at the start and most helped me during my first steps as a PhD student: Gaetano and Gianluca.

During my PhD, I was very lucky to collaborate with researchers and PhD students working on similar topics, from different institutions all over the world. Fostering knowledge exchange, this opportunity elevated my research to a point which would not have been achievable without all this team work involved. I would specifically like to acknowledge the SU2 community for

providing technical support while I was at the stage of getting familiar with numerical tools. I would like to acknowledge Dr. Juan Alonso, Dr. Walter Maier and PhD candidate Jacob Needels from the University of Stanford for working together with me in the challenging development of the SU2-NEMO code. My thanks also goes to Professor Thierry Magin, Dr. James B. Scoggins and PhD candidate Michele Capriati, from the Von Karman Institute of Fluid Dynamics, in Belgium. They have provided me with valuable feedback on how to work with the Mutation++ library, a numerical tool that made my research possible. The help and good will of researcher Adrien Loseille from INRIA is also worthy of acknowledgment, for providing me with a powerful mesh adaptation software that also greatly enhanced the quality of my work.

The second last acknowledgment goes to all my people, outside of the work context, that I could not live without, let alone finish a PhD. My friends have always shown immense pride in me and my work, and supported me wholeheartedly - I want to leave a special thank you for all that. I would like to specifically acknowledge my good friend and ex-flatmate, Michael Connolly, who was with me through thick and thin during the first years of this project, and always kept reminding me "any progress is progress". Finally, my last thank you goes to my family. This will be the shortest acknowledgment because words could never make justice for everything they have given me. *Obrigada Mãe, Pai e Carlos.*

Chapter 1

Introduction

1.1 Context

Shock interactions

The design of future spacecraft for sustained hypersonic flight or atmospheric reentry requires a detailed understanding of the aerothermodynamic environment that the vehicle will experience. Interference of shock waves and boundary layers can occur near compression corners such as the ones found near control surfaces, wing–fuselage junction, or inlet of propulsive systems. A critical issue associated with this phenomenon is the localised high heating and pressure loads acting on the vehicle's surface as a result of the various shock interference patterns. These loads affect the vehicle's performance and airworthiness, and may impose additional thermal protection system requirements that increase the vehicle's weight. The inability to completely capture the physical phenomenon can lead to catastrophic failure, such as the case of the NASA X-15 [1], where unanticipated shock impingement and associated heating caused structural failure. Predicting shock–shock (SSIs) and shock wave - boundary layer interactions (SWBLIs) is still a fundamental problem in fluid mechanics. This thesis specifically concerns the problem of shock interactions in carbon dioxide flows, which are relevant to the atmosphere of Mars.

Double-wedge flows

The double-wedge geometry (illustrated in Fig. 1.1) has been extensively used in the literature to investigate the detailed physics involved in SSIs and SWBLIs. Due to its geometric simplic-

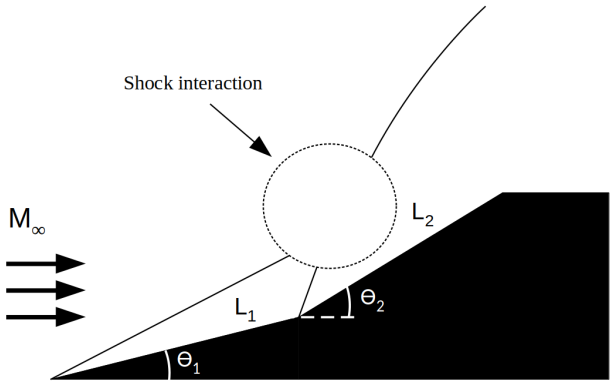

Figure 1.1: Inviscid generic schematic of a hypersonic flow over a double-wegde.

ity and because it is often found in actual vehicle design, the double-wedge flow is a useful representation of idealized cases of hypersonic flow over compression corners [2, 3]. In particular, the double-wedge depicts the generic shape of deflected aerodynamic control surfaces, fuselage/canopy area or hypersonic intakes. The interaction between a shock formed by the fuselage and the shock generated at the wing of a vehicle can also be modelled as a flow over a double-wedge [4]. Although the double-wedge geometry is quite simple, the resulting hypersonic flow environment is not, typically exhibiting complex flow mechanisms such as strong bow shocks, boundary layers, separation zones, flow recirculation, shock impingement, shear layers as well as interaction between these different flow features.

When the hypersonic freestream flow encounters the fore wedge's leading edge, an oblique shock forms, deflecting the streamlines according to the wedge's angle. Likewise, another oblique shock is generated at the compression corner between the two wedges. The type of interaction that occurs (see Fig. 1.1) depends on specific non-dimensional parameters, which for inviscid flow and perfect ideal gas are the Mach number M_∞, the ratio of specific heats γ, the ratio of the first wedge face length to the second wedge face length L_2/L_1, and the two wedge angles θ_1 and θ_2 [3]. In the case of viscous flow, the Reynolds number Re_∞ will also influence the pattern of interaction. When high-temperature effects such as finite-rate chemistry and thermal nonequilibrium are present, the freestream temperature is an additional critical parameter, since it has a significant impact on nonequilibrium processes. In the latter case, the mixture, rather than the specific heat ratio, would be used to characterise the gas dynamics [4].

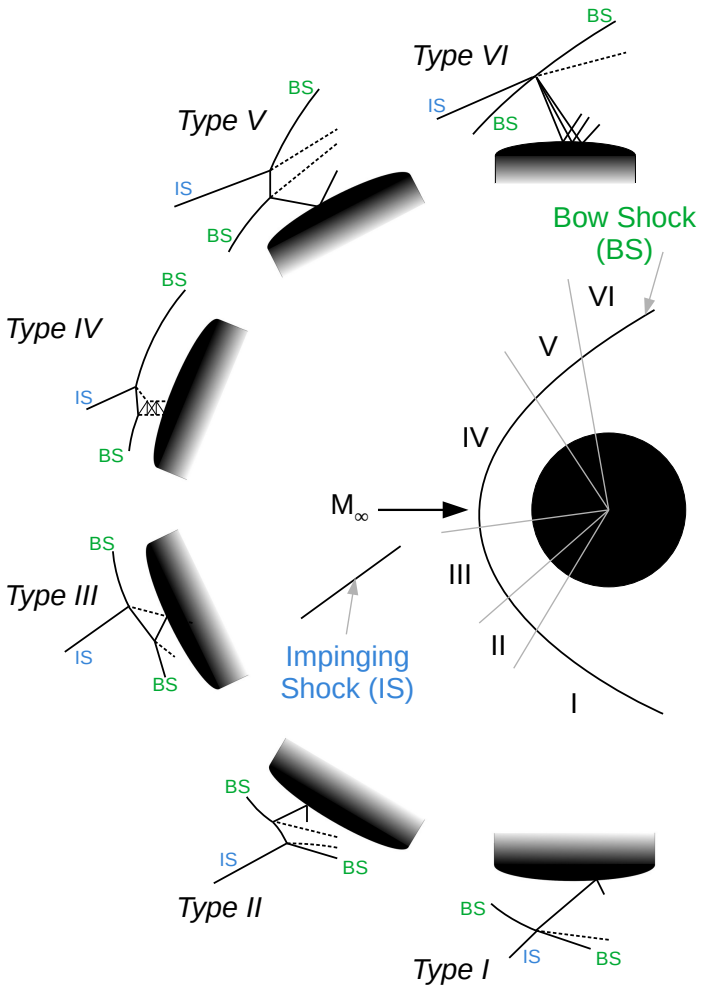

Figure 1.2: Classification of shock interaction patterns by Edney. Adapted from [5].

The classification of different interaction mechanisms into flow pattern types is a result of the pioneering work of Edney [6]. Edney conducted systematic experiments on the impingement of an oblique shock on a bow shock in front of a cylinder. By changing the orientation of the impinging shock, distinct wave patterns were identified. The same shock interaction patterns can be found in flows over double-wedges. Figure 1.2 shows the schematics associated

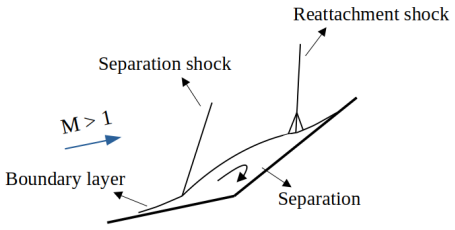

(a) Corner separation shock pattern - recirculation bubble and shock wave system.

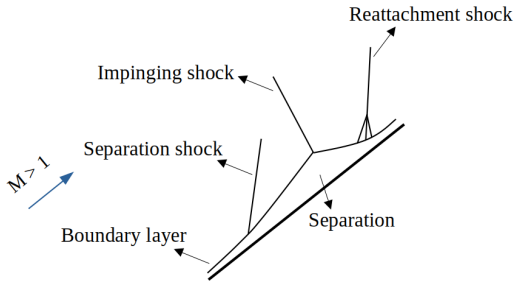

(b) Shock impingement pattern - shock wave system in the case of boundary layer separation due to shock impingement on the surface.

Figure 1.3: Shock-boundary layer interaction patterns.

with the six different types of inviscid shock interaction pattern.

The previous classification refers to an inviscid flow model. When viscous effects are present, the flow patterns become increasingly complex. Shock waves and contact discontinuities are no longer discontinuities, but take the form of high-gradient regions, which may have an substantial impact on how the flow develops. Viscous effects generate additional flow features such as boundary layers, recirculation zones, vortices, etc. The interaction between the different shock waves and the flow features arising from viscous effects leads to intricate flow physics that results in localized severe peaks of pressure and heat flux along the surface.

In this thesis, two pattern types of SWBLI are defined and illustrated in Fig. 1.3. In Fig. 1.3a, a schematic of the corner separation shock pattern is shown. The shock wave generated in the compression corner interacts with the boundary layer that develops along the surface of the fore wedge. The adverse pressure gradient resulting from the presence of the second wedge causes the flow to travel upstream in the subsonic portion of the boundary layer, leading to flow separation ahead of the corner. The flow then reattaches at a certain location on the aft wedge surface and a recirculation bubble is formed below the slip line. This bubble acts as a new wedge, since the supersonic flow over the slip line is forced to adopt the new velocity direction. Besides the presence of a separation/detachment shock wave, reattachment of the boundary layer leads to a series of compression waves that may coalesce and form another shock. The shock wave interaction over the double-wedge may also result in shock impingement on the surface, as illustrated in Fig. 1.3b. In the shock impingement pattern, as the impinging shock

interacts with the boundary layer (SWBLI), it introduces an adverse gradient of pressure. If this interaction is strong enough, it may cause the boundary layer to separate in the vicinity of the impingement point, generating additional separation and reattachment shocks [7]. At the reattachment point, the boundary layer becomes very thin and the pressure is high, resulting in a region of very high aerodynamic heating [8]. Furthermore, depending on the different parameters playing a role, the mechanism of shock interaction may become unsteady. Periodic mechanisms of shock interaction have been reported in various works and are typically a result of the coupling between the recirculation region, the shock impingement induced separation and movement of the bow shock/triple-point [4,9–11]. Sources of unsteadiness in shock interactions can also arise from instability of the shear layers.

The numerical prediction of double-wedge flows is made challenging owing to a number of factors. First, the presence of nonequilibrium finite-rate processes that arise due to the highly-energetic molecular collisions affects both fluid bulk and transport properties. To accurately predict aerodynamic and thermal loads resulting from the mechanisms of shock interaction, robust computational models are required to capture the coupling between fluid bulk motion, chemical kinetics and thermodynamic processes [12]. Second, sufficiently fine grid spacing is necessary to ensure that all the following elements are addressed:

- the flow field resulting from shock wave interference typically results in relatively large regions of nearly uniform flow that are separated by very high-gradient flow features (shock waves, shear layers, slip lines), thus a large range of different flow scales must be resolved;
- accurately resolving the triple-point is crucial, since it plays a large part in the primary mechanism of interaction and can determine the resulting flow pattern;
- a large number of grid points is also required in the vicinity of the reattachment point, since this is the location where peak pressure and heating occur.

Lastly, the separated zone continuously evolves as a result of the recirculating flow, taking a long time to reach steady state relative to the flow characteristic time. As a result, a large amount of physical time needs to be simulated. The combination of all these requirements make

the hypersonic double-wedge flow a complex fluid mechanics problem, despite its geometrical simplicity [13].

Nonequilibrium CO_2 flow

In the hypersonic regime, when a high-speed vehicle collides with a planet's atmosphere, it is subjected to a strong deceleration. Shock waves are formed at different parts of the spacecraft and convert a very large amount of freestream kinetic energy into translational energy of the gas, resulting in a high-enthalpy gas environment. Through molecular collisions, some of the translational energy is transferred into the remaining internal energy modes of the gas (rotational, vibrational, electronic excitation) causing the translational energy to relax [14].

The Martian atmosphere has a composition of 97% CO_2 and 3% N_2 by volume. Other species (primarily Argon) also exist in smaller amounts, but can usually be neglected [15]. The CO_2 molecule has a triatomic structure, that significantly differs from the diatomic ones encountered in air (N_2, O_2) with respect to the behaviour of the vibrational degrees of freedom and subsequent energy redistribution among the various internal modes. More specifically, less energy is required to excite the vibrational degrees of freedom in CO_2 molecules, which is translated in a lower characteristic vibrational temperature relative to the case of an air mixture. Furthermore, if the molecules are sufficiently excited in terms of vibrational motion, they may dissociate into CO and O_2 molecules, and finally O atoms. If bound electrons are sufficiently excited to higher electronic states, ionization reactions may also occur, forming a plasma. When the number of molecular interactions occurring during the characteristic flow time is small, the gas may be in a state of thermal and/or chemical nonequilibrium. Nonequilibrium effects substantially influence the intensity and shape of shock waves, and therefore also the flow mechanisms taking place in regions of shock interaction. Most of the existing literature on the topic focuses on the Earth's atmosphere, thus only considering air or nitrogen flows. Space missions to Mars have recently increased the need for a better understanding of carbon dioxide-dominated atmospheres, which this thesis aims to study.

Research approaches

Continued research efforts have been carried out to tackle the problem of nonequilibrium shock interference but, due to its complexity and multi-physics nature, it is not yet fully understood. The accurate prediction of shock interactions remains a significant challenge in the design and optimization of high-speed vehicles. There are three available research approaches for the investigation of hypersonic flow physics: flight tests, ground-based experiments and numerical simulation.

Flight tests are critical in validating the predictions and insights gained from ground-based experiments and numerical simulations, as they refer to the real flight environment and are able to capture the complexities and nuances that may not be fully replicated with the other two approaches. Nevertheless, flight testing is very costly on Earth's atmosphere and not possible or extremely limited on other planets [16].

Experimental facilities and ground testing play a crucial role in providing valuable insights and data on the environment that the vehicle will realistically experience. They are, however, expensive and unable to fully reproduce the extreme hypersonic flow conditions that lead to the real-gas effects associated to high-enthalpy flows (vibrational excitation and chemical reactions). Replicating real atmospheric and flight data of such flows requires the duplication of the most important similitudes to describe high-enthalpy flow - Mach number, Reynolds number, binary scaling product $\rho - L$ (ρ is the freestream density and L is the characteristic length) and total enthalpy - which is not easy to achieve, especially for longer test durations [17]. A number of experimental campaigns has been conducted to better understand the physics of hypersonic shock interference in air or nitrogen flows [18, 19]. The majority of experimental studies on CO_2 flows, however, deal with blunt bodies [20–26], for which the physics is fundamentally different. Experimental research on carbon dioxide shock interactions is still scarce [27].

Investigation of hypersonic flow through numerical simulation involves solving complex equations that describe a multi-physics problem, including fluid dynamics, thermodynamics, heat transfer and chemistry. Modelling fluid dynamics in the nonequilibrium gas state arising due to the high enthalpy of the flow adds its own challenges to the numerical approach. Accurate numerical predictions require the development and implementation of physical models that capture all the relevant underlying phenomena and coupling mechanisms, as well as dedicated

numerical methods to ensure solver stability, robustness and efficiency [12]. Particularly for the problem of shock interaction, a large length of scales must be resolved and fine grids with appropriate spacing are necessary. Moreover, the fidelity of numerical results can only be ascertained by comparing with experiments. On the other hand, computational methods play a key role in reducing the number of experiments needed to achieve preliminary vehicle designs, since numerical simulation tools are usually more affordable and efficient in predicting the flow environment surrounding the vehicle and associated aerothermal loads acting on surface of the vehicle.

1.2 Motivation, aim and research questions

The hypersonic flow regime concerns a particular class of flows that develop around aerodynamic bodies travelling through gases at speeds much faster than the speed of sound, translating into flight Mach numbers greater than 5. In low-enthalpy hypersonic flows, the gas behaviour can be described as a perfect gas [17], whereas under high-enthalpy conditions nonequilibrium real-gas effects such as vibrational excitation and chemical reactions occur behind strong shocks and affect the gas behaviour [17, 28]. This research project addresses the problem of understanding and predicting shock wave interference in high-enthalpy nonequilibrium carbon dioxide flows. The exploration of Mars has lead carbon-dioxide to be a key chemical species to be studied in hypersonic fluid dynamics, particularly in the context of the applied problem of high-speed vehicle design. Accurately predicting surface properties in the vicinity of regions susceptible to shock impingement through numerical simulation requires thoroughly understanding shock interaction flow physics and the role of nonequilibrium processes on the mechanism of interaction. The complex internal structure of the CO_2 polyatomic molecule and associated internal energy exchange mechanisms are known to play a significant role on mixture properties and thermodynamic processes in high-enthalpy flows. Previous research efforts have focused mostly on investigating shock interactions in air flows and the literature pertaining CO_2 flows is scarce [27, 29].

Research aim. The aim of the present work is the characterization and classification of shock interaction structures in hypersonic carbon-dioxide flows over double-wedges, while also investigating associated aerodynamic/thermal surface loads and the role of nonequilibrium effects. The scope of the thesis focuses on high-enthalpy flow, inviscid and viscous laminar, in thermochemical nonequilibrium with no ionization.

Achieving the previously stated aim is a complex task owing to a number of various challenges. Below follows a list of some of the identified challenges and associated research questions this thesis attempts to address.

Challenge 1. The role of nonequilibrium effects in the establishment of shock interaction mechanisms and resulting surface loads in carbon-dioxide dominated flows is expected to differ from what has been found for air flows, given the different molecular characteristics. The first challenge pertains to understanding the role of thermal and chemical nonequilibrium effects in carbon-dioxide shock interaction physics. The task is notably challenging due to the need to model the coupling between fluid bulk motion, chemical kinetics and thermodynamic processes, since nonequilibrium finite-rate processes arising due to highly-energetic molecular collisions affect fluid macroscopic properties.

Research question 1. Equilibrium shock interaction patterns in inviscid flow modelled with a perfect ideal gas model are determined by the following non-dimensional parameters: freestream Mach number M_∞, the ratio of specific heats γ and the geometrical shape (wedge angles ratio θ_1/θ_2 and wedge lengths ratio L_1/L_2) [3]. In the case of a nonequilibrium flow, the mixture temperature governs finite-rate chemistry and thermal relaxation processes. The first research question this works attempts to address is: *"What is the impact of the freestream temperature on the nonequilibrium processes playing a role in inviscid shock interference carbon-dioxide flows and its influence on the resulting patterns of interaction, and how does it compare to air flows?"*

Challenge 2. The complexity of shock interference mechanisms greatly increases when viscous effects are considered. The changes in the shock structure and the presence of a boundary layer

in the vicinity of the wall result in new flow features such as shear layers (instead of contact discontinuities), recirculation flow regions and shock-boundary layer interactions. Due to the constitutive relations defining transport properties (mass diffusion, viscosity and thermal conductivity) as a function of the temperature, thermal nonequilibrium processes are expected to have an impact on the shape and intensity of the viscous flow features away from the wall, as well as surface pressure and heat flux distributions. Capturing the interaction between vibrational relaxation effects and viscous flow features is a challenging but necessary task to understand nonequilibrium carbon-dioxide viscous shock interactions.

Research question 2.1. The three vibrational modes characterising the CO_2 polyatomic molecule lead to vibrational energy relaxation processes that can significantly affect the flow dynamics, surface pressure and heat transfer. Depending on how strong the deviations are from equilibrium, thermal nonequilibrium effects associated to vibrational relaxation can significantly affect the mechanisms of shock interaction. The second research question posed in this thesis is: *"What is the impact of vibrational relaxation processes on the viscous shock interactions patterns of hypersonic carbon-dioxide flows and associated surface properties?"*

Research question 2.2. Both the freestream Mach number and the double-wedge shape, particularly the aft wedge angle, are known to play a significant role in determining shock angles, size of the recirculation regions and transition of shear layers to instability in hypersonic flows. The latter features establish the mechanism of viscous shock interference and are therefore paramount in definiting the resulting pattern of interaction. The third research question to be addressed in this work is: *"How does the flow physics of carbon-dioxide nonequilibrium shock interactions and associated surface loads change as a consequence of changes in the freestream Mach number and aft wedge angle?*

To address the above research questions, a computational analysis is carried out to simulate nonequilibrium shock interference in carbon-dioxide hypersonic flows by means of CFD (Computational Fluid Dynamics) methods, a numerical approach to model continuum flow. The open-source CFD code SU2-NEMO [12] (NonEquilibrium MOdels), suited for the simulation

of chemically reactive and non-equilibrium flows, is linked to the Mutation++ library [30], allowing for closure of the governing equations by means of coupling with appropriate thermochemistry models. Multi-temperature models, which provide a compromise between computational efficiency and physical accuracy, are used to address the aerothermochemistry effects.

1.3 Thesis layout

The content of the dissertation is structured as follows:

Chapter 2 presents a detailed literature review on the topic relevant to this thesis. An overview of the different studies on shock interaction patterns is provided. Recent studies to better understand unsteady mechanisms of interaction, including sources of unsteadiness and coupling between various flow features, are examined. A review on research efforts assessing the impact of the physical model is presented, considering inviscid vs. viscous flow, different gas mixtures and levels of fidelity. Lastly, literature works specific to the modelling of hypersonic carbon dioxide flows are reviewed;

Chapter 3 focuses on the modelling of hypersonic flows. On the physical modelling, we introduce the kinetic theory of gases based on the quantization of internal degrees of freedom of a molecule. Additionally, the assumptions made in this study and associated governing equations are presented. On the numerical modelling, we provide an overview of the numerical approach used for performing CFD simulations;

Chapter 4 investigates shock interaction patterns in inviscid hypersonic carbon dioxide flows over double-wedges. The freestream temperature is changed to evaluate the impact of different degrees of nonequilibrium on the shock interactions patterns. Furthermore, results are compared to the ones obtained with a mixture of air for the same conditions, to examine the role of the mixture;

Chapter 5 contains a detailed analysis of viscous laminar shock interactions. The types of

interaction are characterized with respect to different double-wedge geometries. The first part of the chapter focuses on understanding the role of thermal nonequilibrium, by comparing simulations results with more simplified equilibrium gas models (thermally perfect gas and perfect ideal gas). The second part of the chapter evaluates the response of shock interaction patterns to different values of the freestream Mach number;

Chapter 6 summarizes conclusions and provides suggestions for further research.

1.4 Publications related to the thesis

The results presented in this dissertation have led to the following publications in international journals and conference proceedings [4, 7, 31–33]:

Conference proceedings

- C. Garbacz, M. Fossati, W. T. Maier, J. J. Alonso, J. B. Scoggins, T. D. Economon, T. Magin. *Numerical study of shock interference patterns for gas flows with thermal nonequilibrium and finite-rate chemistry*. AIAA SciTech Forum, 6-10 January 2020, Orlando, FL. doi.org/10.2514/6.2020-1805
- C. Garbacz, F. Morgado, M. Fossati, J. B. Scoggins, T. Magin, M. Capriati. *Influence of thermochemical modelling of CO_2-N_2 mixtures on the shock interaction patterns at hypersonic regimes*. AIAA Aviation Forum, 2-6 August 2021, Virtual Event. doi.org/10.2514/6.2021-2849
- C. Garbacz, F. Morgado, M. Fossati. *Response of shock interaction patterns to different freestream conditions in carbon dioxide flows over double-wedges*. AIAA Aviation Forum, 27 June - 1 July, 2022, Chicago, IL. doi.org/10.2514/6.2022-3277

Journals

- C. Garbacz, W. T. Maier, J. B. Scoggins, T. D. Economon, T. Magin, J. J. Alonso and M. Fossati. *Shock interactions in inviscid air and CO_2–N_2 flows in thermochemical nonequilibrium*. Shock Waves Vol. 31, p. 239–253, 2021. doi.10.1007/s00193-021-00999-8

- C. Garbacz, F. Morgado, M. Fossati. *Effect of thermal nonequilibrium on the shock interaction mechanism for carbon dioxide mixtures on double-wedge geometries*. Physics of Fluids, Vol. 34, No. 2, p. 026108, 2022. doi.org/10.1063/5.0078233

- C. Garbacz, F. Morgado, M. Fossati. *Characterization of nonequilibrium shock interaction in CO_2-N_2 flows over double-wedges with respect to Mach number and geometry*. Physics of Fluids, Vol. 35, No. 6, p. 066120, 2023. doi.org/10.1063/5.0148436

The computational framework developed in this work served as the foundation for several other collaborative projects, the results of which are described in the following journal publications [34–37]:

- C. Garbacz, F. Morgado, M. Fossati, W. T. Maier, B. C. Munguía, J. J. Alonso, A. Loseille. *Parametric Study of Nonequilibrium Shock Interference Patterns over a Fuselage-and-Wing Conceptual Vehicle*. AIAA Journal, Vol. 59, No. 12, p. 4905-4916, 2021. doi.org/10.2514/1.J060470

- S. F. Gimelshein, I. J. Wysong, A. J. Fangman, D. A. Andrienko, O. V. Kunova, E. V. Kustova, C. Garbacz, M. Fossati and K. Hanquistt. *Kinetic and Continuum Modeling of High-Temperature Oxygen and Nitrogen Binary Mixtures*. Journal of Thermophysics and Heat Transfer, Vol. 36, No. 2, p. 399-418, 2022. doi.10.2514/1.T6258

- S. F. Gimelshein, I. J. Wysong, A. J. Fangman, D. A. Andrienko, O. V. Kunova, E. V. Kustova, F. Morgado, C. Garbacz, M. Fossati and K. M. Hanquist. *Kinetic and Continuum Modeling of High Temperature Air Relaxation*. Journal of Thermophysics and Heat Transfer, Vol. 36, No. 4, p. 1-23, 2022. doi.org/10.2514/1.J061071

- F. Morgado, C. Garbacz, M. Fossati. *Impact of Anisotropic Mesh Adaptation on the Aerothermodynamics of Atmospheric Reentry*. AIAA Journal, Vol. 60, No. 7, p. 3973-3989, 2022. doi.org/10.2514/1.J061071

The following publications present and discusses in detail the computational framework used in the aforementioned research efforts [12]:

- W. T. Maier, J. T. Needels, C. Garbacz, F. Morgado, J. J. Alonso and M. Fossati. *SU2-NEMO: An open-source framework for high-mach nonequilibrium multi-species flows*. Vol. 8, No. 7, Article number 193, Aerospace Journal, 2021. doi:10.3390/aerospace8070193

- W. T. Maier, J. T. Needels, J. J. Alonso, F. Morgado, C. Garbacz, M. Fossati, O. Tumuklu and K. Hanquist. *Development of Physical and Numerical Nonequilibrium Modeling Capabilities within the SU2-NEMO Code*. AIAA Aviation Forum, 12 - 16 June, 2023, San Diego, CA. doi.org/10.2514/6.2023-3488

Chapter 2

Literature review

2.1 Shock interaction patterns

The first systematic study on shock interference mechanisms was carried out by Edney [6], who conducted experiments on the impingement of an oblique shock over a bow shock in front of a cylinder. By changing the location of this intersection, distinct shock interference patterns were identified and classified into six different shock interaction types (illustrated in Fig. 1.2) using a classical shock-polar approach. The pioneering work of Edney was eventually adopted to classify shock interference patterns over other geometries such as the double-wedge case considered in this thesis. Inviscid flow over double-wedges under the perfect gas assumption was numerically studied by Olejniczak et al. [3] in order to identify the shock interaction patterns resulting from increasing the angle of the second wedge. Although there were differences between the flow that emerged for the double-wedge geometries and the cylinder cases, corresponding shock interactions for the steady shock interaction structures were found for types IV, V and VI. Olejniczak et al. additionally identified a shock interaction type IVr which did not occur in the original cylindrical shock classification system.

The transition between type VI and type V (transition type VI-V), as well as the six-shock and seven-shock configurations of type V, were investigated in more detail by Halder et al. [38]. Results obtained for normalized surface pressure matched reasonably well with theoretical values determined by shock jump relations and the point of transition between types VI and V, in terms of angle of the second wedge, agreed with values obtained by Olejniczak et al. [3]. Hu

et al. [39] have used shock polar analytical methods as well as computational fluid dynamics to study the inviscid flow topology occurring for a Mach 9 flow over a double-wedge. Two possible configurations of the type V interaction, the six-shock and seven-shock configuration, and the transition between them were numerically explored by changing the angle of the second wedge. For a relatively small first wedge angle of 15°, the transition between these two configurations, which corresponds to a transition between a regular and a Mach reflection (RR–MR transition), was found to induce hysteresis phenomena and unsteady oscillation of the shock wave pattern, associated to extremely high pressure load on the second wedge surface. For the relatively large first wedge angle $\theta_1 = 25°$, neither oscillation nor hysteresis occurred.

Various works have studied the influence of relevant parameters on the mechanism of shock interaction. The effect of geometrical parameters has been extensively studied in the literature [3, 9, 10, 40]. Exploring the changes in the flow as a result of increasing the angle of the second wedge has revealed that larger aft angles lead to a larger standoff distance of the bow shock and overall increasing complexity of the interaction mechanism, potentially leading to instability of the shear layers or unsteady interaction patterns [9]. Efforts have also been made in the attempt to better understand the influence of the gas mixture and/or specific heat ratio on the physics of shock interactions [41, 42]. Tumuklu et al. [41] compared the flow over a 30°-55°double-wedge for three different gas mixtures: air, nitrogen, and argon. The size of the separation region, the upstream movement of the triple-point, and the time for the flow to reach steady state revealed to be much less for air than for the case of nitrogen. The flow of argon exhibited the fastest movement of the triple-point relative to the other two mixtures. The role of the gas mixture was further investigated by Tumuklu et al. [42]. It was concluded that the relative magnitude of the specific heat ratio has a significant impact on the SWBLI. Specifically, the flow of argon resulted in a separation bubble with 1.8 times the size of the one for nitrogen and — due to the endothermic effects of finite-rate chemistry — the size of this region was 1.5 smaller for air than for nitrogen. The effect of the freestream temperature in hypersonic shock interactions where nonequilibrium effects play a role was investigated by Thirunavukkarasu and Ghosh [40]. Increasing the freestream temperature from 300 K to 900 K caused the shock interaction pattern over the double-wedge to drastically change, with a large impact on the bow shock standoff distance. Further, the influence of the freestream Mach number has been assessed in [40, 43].

A computational analysis of a flow of air over a double-wedge, with $M_\infty = 7.14$ and $M_\infty = 7.3$, revealed that increasing the freestream Mach number results in later flow separation and larger values of the heat flux peaks at reattachment and impinging shock regions, despite presenting the same qualitative distribution of the surface quantities [43]. In [40], the freestream Mach number was increased from 2.8 to 9. The resulting flow field was significantly affected, with the larger value of Mach number leading to reduced shock angles, increased real gas effects that further contribute to smaller shock standoff distances and a significant rise in pressure.

2.2 Unsteady mechanisms of interaction

Unsteady behaviour in flows over double-wedges was first reported by Ben-Dor et al. [44]. Hysteresis and self-induced oscillations giving rise to extremely high pressure loads were found in the type V shock interaction pattern for a range of angles of the second wedge. As aforementioned, Hu et al. [39] have reconsidered inviscid shock interactions on double-wedge geometries in the $M_\infty = 9$ hypersonic flow investigated in [3]. In this work, it was found that the RR–MR transition can induce unsteady oscillation of shock wave patterns, associated with the interaction of shock waves with the slip layers emanating from the triple points.

Several research studies have focused on the unsteady evolution of a hypersonic flow over a double-wedge, with the aim of further understanding oscillatory shock interaction patterns and associated sources of unsteadiness due to coupling between different flow features. Durna et al. [9] have numerically analysed a 2.1 MJ/kg low-enthalpy Mach 7 flow of nitrogen over four different double-wedge configurations, with a fore angle of 30°and the aft angle systematically increased from 45°to 60°. Increasing the aft angle resulted in significant differences in the flow physics. A strong coupling between the deformation of the boundary layer and the bow shock as well as transmitted shock was observed for the higher aft angles. It was found that there is a threshold value of the aft angle, between 45°and 50°, below which the flow reaches steady state and above which becomes periodic in time. Further work was carried out to investigate periodicity of the interactions for the higher aft angles of 50°, 55°and 60° [2]. By analysing density gradients, shock locations, separation angle and distributions of pressure and heat flux along the surface of the wedges, it was concluded that when the aft angle is increased, the pe-

riod of the flow shortens; the duration of impingement of the transmitted shock on the wedge surface decreases; the number of vortexes near the compression corner increases; the distance from the leading edge to the separation point shortens and the separation region becomes longer and thicker. Very recently, Kumar and De [11] investigated the origin and sustenance of the oscillatory shock interaction structures in a nitrogen flow over a 30°-55°double-wedge. The size of the separation bubble was shown to influence the overall shock interaction pattern, also determining whether the flow is steady or not. The presence of an incident shock just downstream of the expansion corner while the separation region is overstretched showed to be the parameter dictating a steady or periodic nature of the flow. It was concluded that different shock interaction patterns can be obtained by varying different geometrical parameters, however it is only when the incidence shock crosses the expansion corner, disturbing the process of relaxation of the separation region, that the flow repeats its previous cycle and becomes periodic. Extending the work by Durna et al. [9], Vatansever and Celik mirrored the numerical study for the case of high-enthalpy flows with a stagnation enthalpy of 8.0 MJ/kg13. It was seen that, as the aft angle is increased, the magnitudes of wall heat flux and surface pressure are enhanced, especially in the vicinity of the separation zone, as a result of stronger shock interactions. Additionally, it was observed that fluctuation magnitudes and time-averaged values of the surface loads were significantly larger on the surface of the second wedge.

2.3 Impact of the physical model

The ability of modern CFD tools to predict the flow physics taking place in regions of shock interaction relies on the development and implementation of models that capture different complex physical mechanisms, such as viscous effects, the thermodynamic behaviour of a given mixture, finite-rate chemistry, thermal nonequilibrium, and so on. Highly complex models such as the DSMC (Direct Simulation Monte Carlo) approach [45] extended for continuum flows, or the state-to-state approach [46], are able to explicitly describe physical processes resulting from particle (molecular and atomic) interaction and therefore capture nonequilibrium phenomena in a detailed manner. However, the associated computational cost is major drawback and its use for engineering applications is unrealistic. Macroscopic approaches with simplifying assumptions

for the physics occurring the microscopic level are a viable and affordable manner to simulate flows in thermochemical nonequilibrium. Depending on the level of simplification, using different models might have an effect on the physical results obtained from a CFD simulation. For this reason, it is crucial to have a thorough understanding of the impact of the physical model when simulation shock interactions.

Tchuen et al. [47, 48] have repeated the study of Olejniczak et al. [3] to incorporate viscous effects and thermochemical nonequilibrium, aiming at assessing the influence of accounting for these two mechanisms in the computational simulation. Leaving aside nonequilibrium effects, a comparison between the computation of viscous and inviscid hypersonic flow over a 15°-60°has been conducted. Even though a type IVr interaction is obtained with both models, the structure of the flowfield revealed to be locally very different. The triple-point slightly moves towards the second wedge when viscous effects are taken into account, and the boundary layer's presence dramatically alters the topology of the underexpanded isentropic flow downstream of the transmitted shock. The influence of viscosity is more visible on the second wedge, as pressure oscillations are dampen down by viscous dissipation.

In the same work [47, 48], Tchuen et al. confirmed the necessity of re-analysing shock interactions with thermochemical nonequilibrium when hypersonic conditions are considered. By comparison with the perfect gas model, it was concluded that real gas effects significantly influence the shock interaction structure and the surface pressure. In the case of flow of air over a 15°-45°double-wedge configuration, it was observed that taking into account nonequilibrium effects caused the interaction pattern to change from a type V to a type VI interaction [47]. A similar tendency was found for a 15°-60°configuration, for which the shock layer thickness decreased significantly, even though the wave structure remained the same [48]. Focusing instead on the transition type VI–V, Li et al. [49] also studied the effects of using a real gas model. It was found that the inclusion of nonequilibrium effects also has a non-neglibigle impact in this case, as it resulted in a delay of the shock interaction pattern transition, with respect to the critical value of the second wedge angle.

Focusing only on viscous interactions, Youssefi and Knight [50] conducted a numerical study to assess CFD capabilities in predicting shock wave laminar boundary layer interaction for the double-cone configuration when different assumptions for thermodynamics and chemical-

kinetics are employed. Four separate cases were simulated for air with stagnation enthalpies ranging from 5.44 MJ/kg to 21.77 MJ/kg and Mach numbers from 10.9 to 12.82 and results were compared against experimental data. A comparison between the equilibrium perfect gas model and a thermodynamic/thermochemical nonequilibrium model (considering one equation for mass and one equation for vibrational energy conservation per chemical species) revealed that the latter model underpredicts the size of the separation region for all cases except 21.77 MJ/kg, but that the pressure plateau in this region, as well as the location of peak pressure and heat flux at reattachment, agree well with the experiment. To better understand the discrepancies of previous studies when it comes to accurately predicting the size of the separation region, Hao and Wen [51] investigated the effects of modelling vibrational nonequilibrium in air flows using different assumptions: 1) a mixture of perfect gases with vibrational nonequilibrium of the mixture, 2) a mixture of perfect gases with vibrational nonequilibrium of separate modes and 3) a mixture of calorically perfect gases. Results showed that, in comparison with model 1), considering separate vibrational modes slightly increases the size of the separation bubble, whereas excluding vibrational excitation significantly enlarges it. It was seen that considering vibrational excitation generally results in a detached shock that is closer to the surface, which was attributed to the fact that this process absorbs the translational energy of the flow, which reduces the post-shock temperatures and increases density, leading to a smaller shock standoff distance. Khraibut and Gai [52] further investigated the impact of real gas effects in shock interactions. It was shown that real gas effects stabilize the entire flow and have a significant impact on the size of the separation bubble, whereas no impact is seen in the flow prior to separation. The study also revealed that, contrary to what was obtained with earlier perfect gas simulations, a steady state is reached when real gas effects are taken into account.

The thermodynamic model considered in a CFD simulation, whether it accounts for nonequilibrium effects or not, depends on parameters that describe the gas' molecular properties, and therefore on the mixture that is considered. Tumuklu et al. [41] investigated viscous laminar shock interactions in a Mach 7 flow over a 30°-55°double-wedge configuration using DSMC. They compared the behaviour of the flow for three different gas mixtures: air, nitrogen and argon. A comparison with experimental data revealed that the numerical model based on a macroscopic approach has succeeded in providing insight into the physics of complex nonequi-

librium flows, as a good agreement for both the unsteady shock wave system and surface heat flux distribution was obtained. Moreover, the size of the separation region, the upstream movement of the triple point and the time for the flow to reach steady state revealed to be much less for air than for the case of nitrogen. The flow of argon exhibited the fastest movement of the triple point relative to the other two mixtures. Later on, the role of the gas mixture on the shock interaction mechanism was further investigated by the same authors [42]. It was concluded that the relative magnitude of the specific heat ratio has a significant impact in SWBLIs. More specifically, the flow of argon resulted in a separation bubble with 1.8 times the size of the one for nitrogen and, due to the endothermic effects of finite-rate chemistry, the size of this region was 1.5 smaller for air than for nitrogen.

2.4 Carbon dioxide flows

The majority of studies aiming to expand the knowledge on the physics of shock interactions was carried out for mixtures of air, molecular nitrogen and molecular oxygen, and little work has been done for other gas mixtures [41, 42, 51, 53–55]. With recent space programs for missions to Mars, the research community has raised interest in its atmosphere, which is mainly composed of carbon dioxide. As stated by Tumuklu et al. [41, 42], the thermodynamic characteristics of a mixture play an important role in the behavior of shock interactions. The CO_2 chemical species is a triatomic molecule whose structure differs from the diatomic ones encountered in air (N_2, O_2) in terms of the behavior of the vibrational degrees of freedom and subsequent energy redistribution among the various internal modes. This results in a characteristic vibrational temperature that is lower than in the case of air, with a non-negligible impact on the nonequilibrium processes. To account for the additional complexity of the triatomic molecule and its impact on macroscopic flow properties, physical models with different levels of detail have been derived and used to simulate CO_2 hypersonic flows.

The two-temperature model has been used in several CFD studies to describe CO_2 vibrational relaxation [26, 56–58]. Using the two-temperature model developed for air with some extensions and modifications, Candler [56] studied a Martian atmospheric entry flow considering a CO_2-N_2 composition. Results showed that, due to the very fast vibrational relaxation of CO_2,

there is very little thermal non-equilibrium. Additionally, at energies below the threshold for CO dissociation, the flow is nearly in chemical equilibrium and, at higher energies, CO dissociation leads to strong chemical non-equilibrium. The two-temperature non-equilibrium model for CO_2 was developed by Park [59]. The application to a reentry simulation of a stagnation-line flow confirmed the conclusions drawn by Candler. Liao et al. [26] carried out validation work on the two-temperature model for CO_2, by comparing experimental measurements of shock stand-off distances over hypersonic spheres in a CO_2 flow to the corresponding numerical simulations. The flow translational temperature reached a maximum value of 5000 K and it was concluded that, under the studied conditions, the two-temperature model is applicable.

In the aforementioned research works, a single vibrational temperature is used to describe all modes of CO_2 vibrations. However, this approach does not take into consideration the complexity of polyatomic vibrational kinetics. On the basis of kinetic theory methods, more advanced and detailed multi-temperature models have been derived to account for the separation of different vibrational modes of the CO_2 molecule and the strong interaction between them [46,60,61]. Kustova and Nagnibeda developed a self-consistent closed description of a high-temperature nonequilibrium dissociating CO_2 flow sufficiently simple to be implemented in engineering applications [60]. The model takes into account three vibrational modes of CO_2 as well as intra- and inter-mode energy transitions. Based on the characteristic relaxation times of the intra- and inter-mode energy exchange processes of CO_2, the vibrational kinetics of the triatomic molecule can be approximated to depend on the vibrational temperature T_{12} of the combined symmetric+bending mode and the vibrational temperature T_3 of the asymmetric mode. In [46, 61], the previous three-temperature formulation has been generalized to the 5 component CO_2/CO/O_2/C/O mixture and applied to the two-dimensional CFD simulation of a viscous shock layer flow near a blunt-body. The obtained results have been compared against the two- and one-temperature approach for weak deviations of thermal equilibrium, corresponding to flow temperatures up to 12,000 K. It was concluded that discrepancies between the accurate three-temperature model and the simplified two-temperature are small just behind the shock front and negligible near the surface of the vehicle, justifying the validity of the latter model under the given conditions. Similar conclusions have been drawn by other authors [62–65].

Building on the three-temperature formulation, a five-temperature model has been derived to

introduce a vibrational temperature for each diatomic species in the mixture CO_2/CO/O_2/C/O [66, 67]. The model has been applied to the numerical simulation of the relaxation zone behind shock waves and results have been compared against the ones obtained with the three-temperature and two-temperature formulation [68]. The discrepancies of temperature values between the more accurate model and the three-temperature model did not exceed 2%, whereas the differences between the five-temperature approximation and the two-temperature one were more noticeable and reach 13%. These conclusions were drawn from a test-case for which the freestream conditions resulted in post-shock temperature of approximately 11,000 K.

The most rigorous and detailed method to describe chemical and vibrational kinetics is the state-to-state approach, where each vibrational state of a molecule is treated as an independent chemical species [69]. Despite the significant amount of research work focusing on the development of this approach, its application to CFD hypersonics is limited to the simulation of one-dimensional boundary layer/stagnation line flows [70–72], and two-dimensional inviscid flows using macroscopic bin approximations [73]. The state-to-state approach appears to be hardly realizable in engineering applications for the case of polyatomic gas mixtures, given the tremendous number of transport coefficients that must be calculated at the each step of a computational fluid dynamic code. Provided all the shortcomings of more detailed physical models when it comes to implementation in CFD codes, it has been overall shown that, for the simulation of hypersonic flows with weak deviations from equilibrium, a two-temperature model is adequate and offers a reasonable compromise between accuracy and computational cost.

Despite the considerable attention given to expanding physical modelling capabilities for hypersonic carbon dioxide flows, the literature discussing the identification of shock wave interference patterns and the associated aerothermal loads in the case of CO_2 flows is scarce. Windisch et al. [29] simulated the intersection between an oblique shock and a bow shock in front of a cylinder with a CO_2-dominated flow and observed the type VII interaction. A comparison with the same test-case but considering instead a N_2 mixture revealed that the post-shock temperatures were significantly lower for the gas model of the Martian atmosphere, resulting in a higher fluid density and a much smaller shock stand-off distance. Moreover, thermal non-equilibrium was nearly non-existent. Knisely has carried out extensive experimental work on shock interactions patterns over double-wedge and double-cone geometries for different gas mixtures: air, nitro-

gen and carbon dioxide [27]. The carbon dioxide mixture was used with the double-cone model exclusively and resulted in a type VI interaction. The surface heat flux experimental data was compared against theoretical and numerical predictions of a laminar flow. A good agreement was obtained up to the point of boundary layer separation, which was suggested to be due to a transitional flow. However, there was no systematic in-depth analysis of the shock interaction mechanisms for this specific gas mixture.

Chapter 3

Modelling of nonequilibrium hypersonic flows

3.1 Physical modelling

Detailed modelling of the physics involved in the nonequilibrium aerothermodynamic environment is necessary for the accurate prediction of hypersonic flows. In this flow regime, there are regions where the temperature is high and therefore molecular collisions are highly energetic, which results in finite-rate processes like chemical reactions and internal energy relaxation that affect the macroscopic properties of the fluid and may even dominate the flow characteristics. In this section, physical models that account for the coupling between fluid bulk motion, chemical kinetics, transport properties and thermodynamic nonequilibrium processes are introduced.

3.1.1 Kinetic theory of gases

The physical modelling of a nonequilibrium flow is based on a microscopic description of the gas by means of statistical thermodynamics. It is assumed that the gas consists of a large number of individual molecules/atoms with different modes of energy, corresponding to different degrees of freedom. The internal modes of energy of the CO_2 triatomic linear molecule are illustrated in Fig. 3.1

The translational energy mode of a molecule/atom, corresponding to the kinetic energy of its center of the mass, is associated to their translational motion. Atoms and molecules also possess

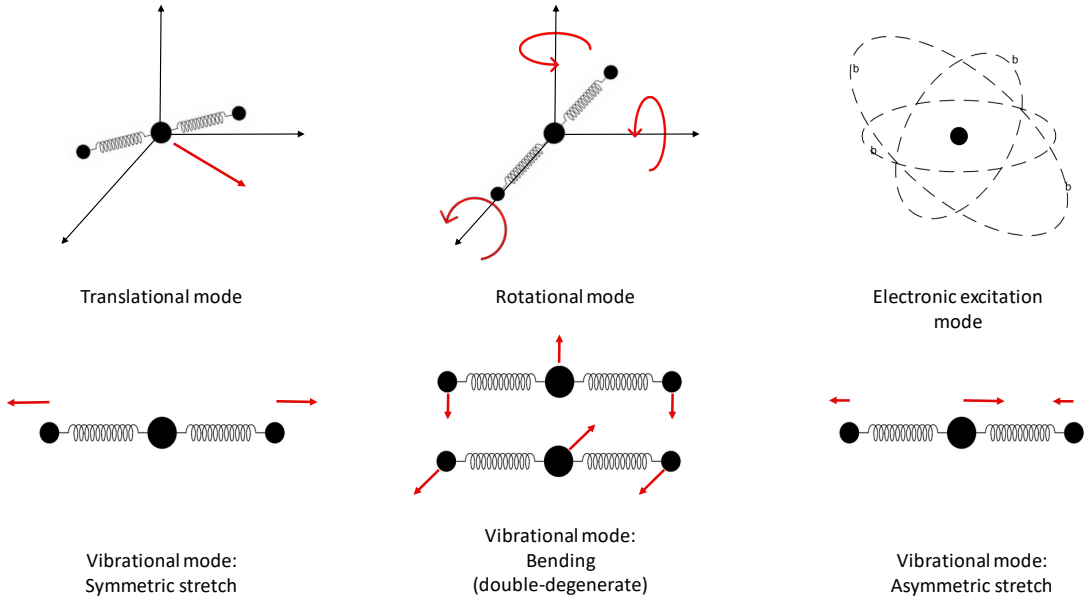

Figure 3.1: Internal energy modes of the CO_2 molecule.

a given amount of internal energy that is related to electronic excitation - the relative position of bound electrons with respect to the nucleus. Molecules exhibit two other degrees of freedom: rotation and vibration. The molecule's rotational kinetic energy, corresponding to its rotational energy mode, is associated to their rotational motion and moment of inertia. The vibrational energy of a molecule is a result of the vibrational motion of its atoms with respect to an equilibrium location. The CO_2 molecule exhibits three different vibrational modes: symmetric stretch, asymmetric stretch and bending - the latter one being double-degenerate. When the gas is in thermal nonequilibrium, the internal energy modes relax according to different time scales, and separation of the internal contributions to the global energy of the gas is required [74]. The total energy of a molecular chemical species ε_s is defined by the sum of these contributions:

$$\varepsilon_s = \varepsilon_{s,tra} + \varepsilon_{s,rot} + \varepsilon_{s,vib} + \varepsilon_{s,el} \tag{3.1}$$

For atoms, only translational and electronic energies are considered:

$$\varepsilon_s = \varepsilon_{s,tra} + \varepsilon_{s,el} \tag{3.2}$$

The study of quantum mechanics has shown that each of the previous energies is quantized,

which means that they can exist only at certain discrete values, as illustrated in the ladder-type diagram of Fig. 3.2. The vertical spacing between two energy levels is a measure of the energy interval between them. The vibrational column in the diagram is representative all of vibrational modes of CO_2.

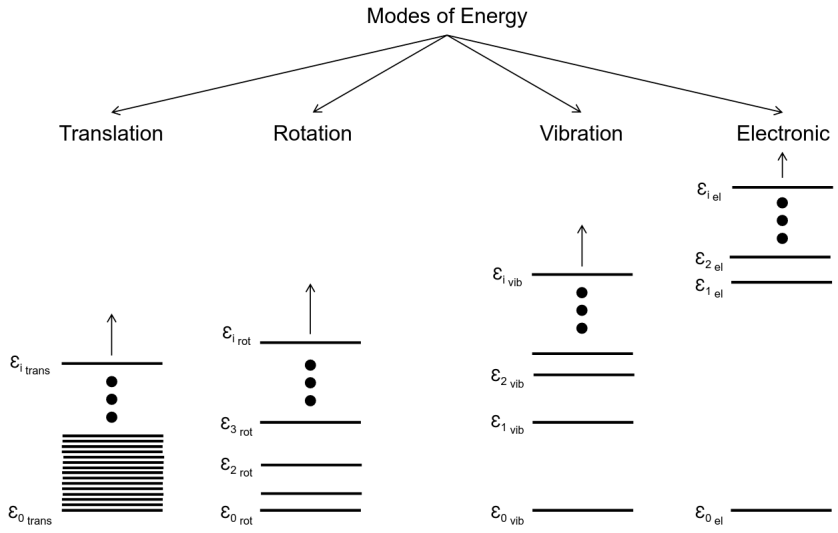

Figure 3.2: Diagram for the energy levels of the different thermal modes [74]. Index *i* refers to chemical species.

The lowest allowable energies for each level, denoted by ε_0, correspond to the energy that the particle would have at a temperature of absolute zero and are called the *ground-state* of each mode.

A single-species (denoted by s) system is therefore composed of a grand total of N_s molecules, which is the sum of the species fractions $N_{j,s}$ that occupy a given energy level $\varepsilon_{j,s}$:

$$N_s = \sum_j N_{j,s} \tag{3.3}$$

$N_{j,s}$ is defined as the population of the energy level $\varepsilon_{j,s}$ and the set of numbers formed by the several values of $N_{j,s}$ define the *population distribution*. As molecular collisions occur in a system and the molecules depart from one energy level to another, the population distribution can change. Additionally, for a given energy level $\varepsilon_{j,s}$, molecular orientation may vary, also in

a quantized manner (see Fig. 3.3). The number of different states that occur within the same energy level is called *degeneracy*, denoted by g_i.

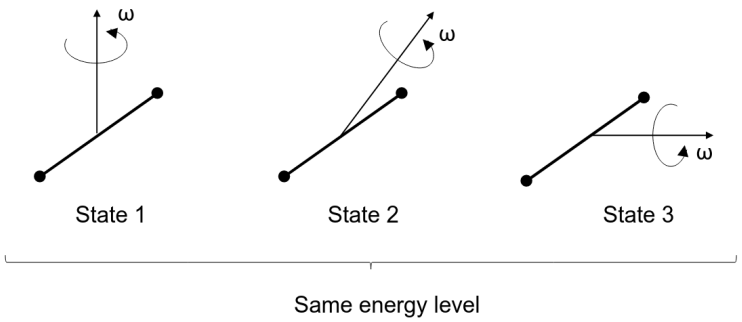

Figure 3.3: Different energy states according to molecular orientation [74].

Two-temperature approximation

In hypersonic flow, when the fluid is rapidly decelerated across a shock wave, a large amount of kinetic energy is transformed into translational energy of the gas. Through molecular collisions, this energy is exchanged between the different energy modes leading to a given population distribution. For weak deviations from equilibrium , one can assume partial thermal equilibrium. Under this assumption, the population of different energy modes follows a Boltzmann distribution at a specific temperature (T_{rot} for the rotational, T_{vib} for the vibrational, T_{el} for the electronic mode) - which is the base assumption of multi-temperature models. The Boltzman distribution for the population of internal energy levels is expressed according to the partition function Q_s:

$$\frac{N_{j,s}}{N_s} = \frac{g_{j,s} \exp\left(-\frac{\varepsilon_{j,s}}{k_B T}\right)}{Q_s} \tag{3.4}$$

The partition function Q_s is defined by a sum over the allowed energy states of the system, with each state weighted by a statistical factor:

$$Q_s = \sum_j g_{j,s} \exp\left(-\frac{\varepsilon_{j,s}}{k_B T}\right) \tag{3.5}$$

where k_B denotes the Boltzmann constant.

For weak deviations from equilibrium and for the specific approximation of a **two-temperature model** in a CO_2-based mixture, the following assumptions are considered:

1. the three vibrational modes relax at the same rate, thus can be described by a single vibrational temperature T_{vib} [75];

2. any other diatomic species in the mixture relax at the same rate as the vibrational modes of CO_2 and can be described by the same vibrational temperature T_{vib};

3. the motion of atoms due to molecular vibration has a negligible impact on the molecular moment of inertia, implying that there is no rotational-vibrational coupling and the molecule can be described as rigid rotor and harmonic oscillator;

4. as illustrated by the spacing between energy levels of different modes in Fig. 3.2, they are characterized by different time scales, satisfying the following condition:

$$\tau_{tra} < \tau_{rot} \ll \tau_{vib} < \tau_{react} \sim \theta \tag{3.6}$$

where τ_{tra}, τ_{rot}, τ_{vib}, τ_{react} are the characteristic times for translational, rotational, vibrational relaxation, chemical reactions and θ is the gas-dynamic time scale. The above condition 3.6 takes into account assumption 1. Empirical data shows that the translational and rotational relaxation proceed much faster compared to any vibrational energy transitions and chemical reactions, while the two latter processes have relaxation times of the same order as the mean time of the gas-dynamic parameters variation [76];

5. rotational and vibrational mode excitation is induced before excitation of the electronic modes and it is assumed that all particles are in the ground electronic state.

On the basis of the aforementioned assumptions, the gas of a hypersonic flow can be described to be in partial thermal equilibrium, where the translational and rotational modes are considered to be in equilibrium with each other (trans-rotational mode), and the vibrational and electronic

modes are considered to be in equilibrium with each other (vibro-electronic mode). In this approach, the gas is described by two temperatures, trans-rotational and vibro-electronic:

$$T_{tra} = T_{rot} = T_{tr} \neq T_{vib} = T_{elec} = T_{ve} \tag{3.7}$$

3.1.2 Governing equations

In this section, the physical model describing hypersonic flows accounting for high-temperature effects is presented. The system of governing equations follows the Navier–Stokes approach for a continuum, viscous laminar, thermal nonequilibrium flow with finite-rate chemistry [77]. The two-temperature model by Park is used to model thermal nonequilibrium. It has been developed initially for air [78] but later modified for CO_2 flows [59] and validated in [26,79] against experimental data and the more detailed state-to-state approach. The modified set of Navier-Stokes equations includes a continuity equation for each species included in the mixture, the momentum equation, the total energy conservation equation and a vibrational (vibro-electronic) energy conservation equation. The system of equations is not mathematically closed since it requires the modeling of the transport fluxes (shear viscosity, heat flux and diffusion fluxes), a proper definition of the internal energy source terms accounting for chemical reactions and energy relaxation in the fluid. Thus the physical description incorporates various physical and mathematical models, discussed in the next chapters: thermodynamics, internal energy exchange mechanisms, finite rate chemical kinetics and transport properties.

Species continuity equations

The set of Navier-Stokes equations considers a continuity equation per chemical species s in the mixture to describe the evolution of the gas composition:

$$\frac{\partial \rho_s}{\partial t} + \nabla \cdot \rho_s \vec{u} = \nabla \cdot \vec{J}_s + \dot{\omega}_s \tag{3.8}$$

where $\vec{u}$ is the flow velocity vector, ρ_s is the species mass density, $\dot{\omega}_s$ is the chemical source term to account for production/depletion of a given species as a result of chemical reactions, and $\vec{J}_s$ is the species mass diffusion flux. There is no net destruction or production of matter

inside the mixture and the total mass of the system does not diffuse, therefore:

$$\sum_s \dot{\omega}_s = 0 \tag{3.9}$$

$$\sum_s \vec{J}_s = 0 \tag{3.10}$$

Summing up all the species continuity equations, the global mass conservation equation is retrieved:

$$\frac{\partial \rho}{\partial t} + \nabla \cdot \rho \vec{u} = 0 \tag{3.11}$$

where ρ is the total mass density of the mixture.

Momentum equation

The momentum conservation equation is written as follows

$$\frac{\partial \rho \vec{u}}{\partial t} + \nabla \cdot (\rho \vec{u} \otimes \vec{u} + p\bar{I}) = \nabla \cdot \bar{\tau} \tag{3.12}$$

where p is the mixture pressure and $\bar{\tau}$ is the viscous stress tensor.

Total energy equation

The equation for conservation of total energy of the flow is given by:

$$\frac{\partial \rho e}{\partial t} + \nabla \cdot (\rho h \vec{u}) = \nabla \cdot \left(\bar{\tau} \cdot \vec{u} + \sum_s \vec{J}_s h_s + \vec{q}^{\text{ve}} + \vec{q}^{\text{tr}} \right) \tag{3.13}$$

where h is the total enthalpy per unit mass $h = e + \frac{p}{\rho}$, $\vec{q}^{\text{ve}}$ is the conduction heat flux associated to the vibro-electronic temperature, $\vec{q}^{\text{tr}}$ is the conduction heat flux associated to the trans-rotational temperature and e is the total energy of the flow per unit mass, accounting for the kinetic energy of the flow and the internal energy of the mixture:

$$e = \sum_{s=1}^{n_s} c_s e_s + \frac{1}{2}u^2 \tag{3.14}$$

where c_s is the mass fraction of the species, u is the magnitude of the flow velocity vector and e_s is the specific internal energy of the species.

Vibrational energy equation

The vibrational energy equation expresses the conservation of the sum of vibrational and electronic energy of the mixture, as follows:

$$\frac{\partial \rho e^{\mathrm{ve}}}{\partial t} + \nabla \cdot (\rho e^{\mathrm{ve}} \vec{u}) = \nabla \cdot \left(\sum_s \vec{J}_s h_s^{\mathrm{ve}} + \vec{q}^{\mathrm{ve}} \right) + \dot{\Omega} \tag{3.15}$$

where e^{ve} and h^{ve} are, respectively, the sum of specific vibrational and electronic energy and enthalpy per unit mass for the mixture, and $\dot{\Omega}$ is the vibro-electronic energy source term.

Thermodynamics

Calculating the nonequilibrium thermodynamic state and source terms is necessary to close the system of governing equations that describes hypersonic flows. This is achieved by means of coupling with appropriate multi-temperature thermochemistry models. The equations presented below describe the implementation of the two-temperature model for a mixture composed of neutral species. The gas is assumed to be a chemically reacting mixture of perfect gases, hence the total pressure of the mixture p is defined by Dalton's Law as the summation of the partial pressures associated with each species p_s and each component of the mixture is governed by the equation of state:

$$p = \sum_{s=1}^{n_s} p_s = \sum_{s=1}^{n_s} \rho_s \frac{R_{\mathrm{u}}}{M_s} T_{\mathrm{tr}}, \tag{3.16}$$

where R_{u} is the universal gas constant, M_s is the molar mass of species s and T_{tr} is the trans-rotational temperature. The specific internal energy of the species is given by the sum of the energy of formation and the contribution of each internal mode (translational, rotational, vibrational, electronic):

$$e_s = e_s^{\mathrm{tra}}(T_{\mathrm{tr}}) + e_s^{\mathrm{rot}}(T_{\mathrm{tr}}) + e_s^{\mathrm{vib}}(T_{\mathrm{ve}}) + e_s^{\mathrm{el}}(T_{\mathrm{ve}}) + e_s^0. \tag{3.17}$$

Using a combination of statistical thermodynamics and quantum mechanics, the internal mode energies are defined on the basis of the Rigid-Rotor Harmonic Oscillator model as:

$$e_s^{\mathrm{tra}}(T_{\mathrm{tr}}) = \frac{3}{2}\frac{R_{\mathrm{u}}}{M_s}T_{\mathrm{tr}}, \tag{3.18}$$

$$e_s^{\mathrm{rot}}(T_{\mathrm{tr}}) = \begin{cases} \frac{R_{\mathrm{u}}}{M_s}T_{\mathrm{tr}}, & \text{for linear molecules,} \\ 0, & \text{for atoms,} \end{cases} \tag{3.19}$$

$$e_s^{\mathrm{vib}}(T_{\mathrm{ve}}) = \begin{cases} \frac{R_{\mathrm{u}}}{M_s}\sum\limits_{\upsilon}\frac{\theta^{\mathrm{v}}_{\upsilon,s}}{\exp(\theta^{\mathrm{v}}_{\upsilon,s}/T_{\mathrm{ve}})-1}, & \text{for molecules,} \\ 0, & \text{for atoms,} \end{cases} \tag{3.20}$$

$$e_s^{\mathrm{el}}(T_{\mathrm{ve}}) = \frac{R_{\mathrm{u}}}{M_s}\frac{\sum\limits_i g_{i,s}\theta^{\mathrm{e}}_{i,s}\exp(-\theta^{\mathrm{e}}_{i,s}/T_{\mathrm{ve}})}{\sum\limits_i g_{i,s}\exp(-\theta^{\mathrm{e}}_{i,s}/T_{\mathrm{ve}})}, \tag{3.21}$$

where $\theta^{\mathrm{v}}_{\upsilon,s}$ is the characteristic vibrational temperature of species s and vibrational mode υ, $g_{i,s}$ and $\theta^{\mathrm{e}}_{i,s}$ are the degeneracy and characteristic electronic temperature, respectively, at energy level i for species s. The formation energy e_s^0 is referenced at the standard state conditions of 298.15 K and 1 atm.

Finite rate chemical kinetics

Thermo-chemistry provides the mass production terms according to the Law of mass action. Macroscopic rate coefficients are assumed to depend on an empirical temperature which is function of the different temperatures in the flow. The chemical source term $\dot{\omega}_s$ is given by:

$$\dot{\omega}_s = M_s \sum_{r=1}^{n_r} (\nu''_{s,r} - \nu'_{s,r}) \left[k_{\mathrm{f},r} \prod_{j=1}^{n_s} \hat{\rho}_j^{\nu'_{j,r}} - k_{\mathrm{b},r} \prod_{j=1}^{n_s} \hat{\rho}_j^{\nu''_{j,r}} \right], \tag{3.22}$$

where n_r and n_s are, respectively, the number of reactions and the number of species, ν'_s is the forward reaction stoichiometry coefficient, ν''_s is the backward reaction stoichiometry coefficient, $\hat{\rho}_j$ is the molar density, $k_{\mathrm{f},r}$ is the forward reaction rate and $k_{\mathrm{b},r}$ is the backward reaction rate. The forward reaction rate for each reaction r is defined according to the modified Arrhenius equation:

$$k_{\mathrm{f},r} = A_r T_{\mathrm{c}}^{N_r} \exp\left(-\frac{\theta_r}{T_{\mathrm{c}}}\right), \tag{3.23}$$

where the coefficients A_r, θ_r and N_r are obtained from experimental data and are, respectively, the reaction rate constant, the activation temperature and an exponent. The backward reaction rates $k_{\mathrm{b},r}$ are determined from the equilibrium reaction rates, $k_{\mathrm{b},r} = k_{\mathrm{f},r}/k_{\mathrm{eq},r}$ for every reaction r. The equilibrium reaction rates $k_{\mathrm{eq},r}$ are determined as a function of the Gibbs free energy. T_{c} is the controlling temperature determined by Park's two-temperature model [80]:

- Dissociation reactions AB + M $\Leftrightarrow$ A + B + M
  $T_{\mathrm{c}} = \sqrt{T_{\mathrm{tr}} T_{\mathrm{ve}}}$ for the forward rate; $T_{\mathrm{c}} = T_{\mathrm{tr}}$ for the backward rate;
- Exchange reactions AB + C $\Leftrightarrow$ A + BC
  $T_{\mathrm{c}} = T_{\mathrm{tr}}$.

Energy exchange mechanisms

In the two-temperature model, the energy transfer mechanisms that determine the change in vibrational energy of the mixture are accounted for in the source term vector. The source term $\dot{\Omega}$ is defined as the sum of the vibrational-to-translational energy transfer and energy exchanges due to chemical activity,

$$\dot{\Omega} = \sum_{s=1}^{n_s} \dot{\Omega}_s^{\mathrm{tr:ve}} + \dot{\Omega}_s^{\mathrm{c:v}} + \dot{\Omega}_s^{\mathrm{c:e}}. \tag{3.24}$$

The term $\dot{\Omega}^{\mathrm{tr:ve}}$ concerns the rate of energy exchange between the translational and vibrational energy modes, following the Landau-Teller model [81]

$$\dot{\Omega}_s^{\mathrm{tr:ve}} = \rho_s \frac{e_s^{\mathrm{v}}(T) - e_s^{\mathrm{v}}(T_{\mathrm{v}})}{\tau_s^{\mathrm{V\text{-}T}}}. \tag{3.25}$$

The vibrational relaxation time of each species, $\tau_s^{\mathrm{V\text{-}T}}$, is given by the Millikan and White empirical formula [82] and the Park correction [80],

$$\tau_s^{\mathrm{V\text{-}T}} = \tau_s^{\mathrm{MW}} + \tau_s^{\mathrm{P}}, \tag{3.26}$$

where the Millikan and White relaxation time of species s depends on the vibrational relaxation times of the interactions with collision partners r and the corresponding molar fractions X_r, as follows

$$\tau_s^{\mathrm{MW}} = \left(\sum_{r=1}^{n_s} \frac{X_r}{\tau_{s-r}^{\mathrm{MW}}} \right)^{-1}, \tag{3.27}$$

$$\tau_{s-r}^{\mathrm{MW}} = \exp\left(A_{s,r}\left(T^{-\frac{1}{3}} - B_{s,r} \right) - 18.42 \right)\left(\frac{p}{101325} \right)^{-1} [s]. \tag{3.28}$$

The Park correction is given by

$$\tau_s^{\mathrm{P}} = \left(N_s \sigma_s \sqrt{\frac{8 R_{\mathrm{u}} T_{\mathrm{tr}}}{\pi M_s}} \right)^{-1}, \tag{3.29}$$

where r denotes the r^{th} species, X_r is the molar fraction, N_s is the number density and σ_s is an effective cross-section for vibrational relaxation. The change in vibrational-electronic energy of the mixture due to the production/destruction of species is accounted for in the terms $\dot{\Omega}_s^{\mathrm{c:v}}$ and $\dot{\Omega}_s^{\mathrm{c:e}}$, given by

$$\dot{\Omega}_s^{\mathrm{c:v}} = c_1 \dot{\omega}_s e_s^{\mathrm{v}}, \quad \dot{\Omega}_s^{\mathrm{c:e}} = \dot{\omega}_s e_s^{\mathrm{e}}. \tag{3.30}$$

A non-preferential dissociation model is considered to account for the coupling between vibrational energy modes and finite-rate chemistry. The model assumes that molecules are destroyed

or created at the average vibrational energy of the cell, $c_1 = 1$.

Transport properties

With regard to dissipative fluxes, the mass diffusion flux of each species $\vec{J}_s$ is described by Fick's Law of diffusion:

$$\vec{J}_s = \rho_s \vec{V}_s \tag{3.31}$$

where $\vec{V}_s$ is the species diffusion velocity, obtained by solving the Stefan-Maxwell equations under the Ramshaw approximation [83]. The viscous stress tensor is written in vector notation as:

$$\bar{\tau} = \mu \left(\nabla \vec{u} + \nabla \vec{u}^{\mathsf{T}} - \frac{2}{3} \bar{I} (\nabla \cdot \vec{u}) \right) \tag{3.32}$$

where μ is the mixture viscosity coefficient. The conduction heat flux for each thermal energy mode $\vec{q}_k$ is assumed to be given by Fourier's Law of heat conduction:

$$\vec{q}_k = \lambda_k \cdot \nabla T_k \tag{3.33}$$

where T_k is the temperature and λ_k is the thermal conductivity coefficient of the kth energy mode. Viscosity μ and mode thermal conductivity λ_k are computed using Wilke's mixing rule [84]. The species thermal conductivity is calculated using Eucken's formula [85] that takes into account both translational and vibrational temperatures.

3.2 Numerical modelling

In order to simulate a hypersonic flow, a discrete formulation of the equation system given in Section 3.1.2 must be incorporated in a CFD code to be solved using numerical methods. When nonequilibrium effects are present, numerical models are required to effectively capture the coupling between fluid bulk motion, chemical kinetics and thermodynamic processes. This task is numerically challenging due to the various time scales associated to the different physical processes. To tackle the problem in a stable, reliable, and effective manner, appropriate numerical models must be used. This section introduces the numerical discretization models

that have been employed in the computational analysis, including both the discretization of the governing equations and time-integration approach.

In a compact form, the system of equations can be described as:

$$\frac{\mathrm{d}\mathbf{U}}{\mathrm{d}t} + \nabla \cdot \vec{\mathbf{F}}^{c}(\mathbf{U}) = \nabla \cdot \vec{\mathbf{F}}^{v}(\mathbf{U}) + \mathbf{Q}(\mathbf{U}) \tag{3.34}$$

The Finite Volume method is used to solve the discretized governing equations on an edge-based median dual-grid numerical mesh. The discretized conservation equations can be written for a control volume Ω_i as:

$$\int_{\Omega_i} \frac{\partial \mathbf{U}_i}{\partial t}\, d\Omega + \sum_{j \in N(i)} (\hat{\mathbf{F}}^{c}_{ij} + \hat{\mathbf{F}}^{v}_{ij}) \Delta S_{ij} - \mathbf{Q}|\Omega_i| = \int_{\Omega_i} \frac{\partial \mathbf{U}_i}{\partial t}\, d\Omega + \mathbf{R}(\mathbf{U}_i) = 0 \tag{3.35}$$

where $\mathbf{U}_i$ is the vector of conservative variables at cell i and $\mathbf{R}(\mathbf{U}_i)$ is residual representing the integration of all spatial terms at node i. $\hat{\mathbf{F}}^{c}_{ij}$ and $\hat{\mathbf{F}}^{v}_{ij}$ are the numerical approximations of the convective and viscous fluxes, and $\mathbf{Q}$ is a vector of source terms. ΔS_{ij} is the area of the face associated with the edge ij, Ω_i is the volume of the dual control volume, and $N(i)$ is the set of neighboring nodes to node i. The fluxes are computed at the midpoint of each edge, and added/subtracted to the residual for each of the two nodes making up a particular edge.

The system of governing equations is discretized on the basis of the upwind convective scheme AUSM (Advection Upstream Splitting Method), a flux-vector splitting method commonly used for high-speed flows due to its high accuracy and robustness [86]. AUSM is a low-dissipation, non-oscillatory scheme that enables superior shock capturing and avoids the presence of carbuncle effects typically observed in regions of strong shocks. The scheme separates the flux vector into convective terms propagated at the local flow velocity and pressure terms propagated at the local speed of sound, expressed as:

$$\hat{\mathbf{F}}_{ij} \cdot \mathbf{n} = \begin{bmatrix} \rho_s \\ \rho \mathbf{u} \\ \rho h \\ \rho e^{ve} \end{bmatrix} (\mathbf{u} \cdot \mathbf{n}) + \begin{bmatrix} 0 \\ p\mathcal{I} \cdot \mathbf{n} \\ 0 \\ 0 \end{bmatrix}, \tag{3.36}$$

where the interface Mach number M_{ij} can be split as:

$$M_{ij} = M_i^+ + M_j^-, \tag{3.37}$$

and $M^\pm$ are defined by using Van Leer splitting [87]:

$$M^\pm = \begin{cases} \pm\frac{1}{4}(M \pm 1)^2 & \text{if } |M| \leq 1 \\ \frac{1}{2}(M \pm |M|) & \text{otherwise} \end{cases} \tag{3.38}$$

Pressure is similarly discretized as:

$$p_{ij} = p_i^+ + p_j^-, \tag{3.39}$$

such that

$$p^\pm = \begin{cases} \frac{p}{4}(M \pm 1)^2(2 \mp M) \text{ for } |M| \leq 1. \\ \frac{p}{4}(M \pm |M|)/M \text{ otherwise.} \end{cases} \tag{3.40}$$

The flux approximation is given by

$$\hat{\mathbf{F}}_{ij} = \frac{(M_{ij} + |M_{ij}|)}{2} \begin{bmatrix} \rho_s c \\ \rho \mathbf{u} c \\ \rho h c \\ \rho e^{ve} c \end{bmatrix}_i + \frac{(M_{ij} - |M_{ij}|)}{2} \begin{bmatrix} \rho_s c \\ \rho \mathbf{u} c \\ \rho h c \\ \rho e^{ve} c \end{bmatrix}_j + P_{ij} \begin{bmatrix} 0 \\ \mathcal{I} \cdot \mathbf{n} \\ 0 \\ 0 \end{bmatrix}. \tag{3.41}$$

The convective scheme is used together with a MUSCL (Monotonic Upstream-centered Scheme for Conservation Laws) strategy and the Venkatakrishnan-Wang limiter to achieve a second order in space discretisation.

Viscous fluxes are computed at the median dual-grid interfaces and discretised by means of a second-order accurate central scheme, with gradient information evaluated using a Weighted Least-Squares approach and appropriate corrections in areas of high cell skewness. A dual time-stepping approach with a second-order backwards-difference discretization of the time

derivative terms is used to address time integration in cases where the flow is unsteady. Details on the code implementation carried out in this work, as well as a description of the numerical solver, are provided in Appendix A. Furthermore, accurately modelling shock interactions requires capturing different types of flow features and ensuring adequate grid spacing is crucial. The grid adaptation approach used in this work is described in Appendix B. Thorough validation of the numerical approach has been carried out for relevant test-cases and is detailed in Appendix C.

Chapter 4

Inviscid shock interactions

The present chapter serves as the starting point in the investigation of the physics governing shock interactions in CO_2 double-wedge hypersonic flows. Viscous effects are expected to play a significant role [47, 48], since the occurrence of shock/boundary-layer interaction can greatly influence the structure of the flow patterns. Nevertheless, the additional length scales introduced by a viscous model make the analysis of the shock interaction structure more challenging. In this chapter, an inviscid model is considered and focus is given to flow patterns resulting exclusively from shock-shock interactions.

The relaxation times that govern translational-to-vibrational energy transfer and the reaction rates that determine the chemical state of the flow are essentially function of the mixture temperature, therefore the freestream flow temperature is expected to influence nonequilibrium processes, which in turn may impact the resulting patterns of interaction. The objective of this chapter is to numerically study the gas dynamics involved in nonequilibrium inviscid shock interactions in CO_2-N_2 mixtures by varying the freestream temperature parameter. Considering the extensive research on shock interaction in air flows, this study conducts simulations on both air and CO_2-dominated mixtures to allow for a comparative analysis, taking into consideration the molecular structural differences between the two mixtures. Furthermore, to assess the effect of modelling nonequilibrium effects, the same simulations are additionally performed with a calorically perfect ideal gas model. Since for invisicd flow and ideal gas behaviour shock patterns are only function of the non-dimensional parameters γ, M_∞, $L_1/L_2 2$ and of θ_1 and θ_2, only one value of freestream temperature is considered.

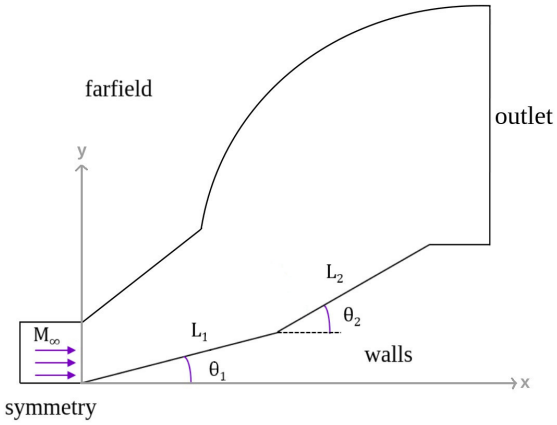

Figure 4.1: Double-wedge geometry, computational domain and boundary conditions.

The first section 4.1 presents the geometry and computational domain used in the computational analysis, together with boundary conditions. The test-case matrix providing simulation parameters is also presented. Choice of grid and grid independence studies are discussed in Section 4.2. In Sections 4.3 and 4.4, the impact of changing the freestream temperature on the patterns of shock interaction and the role of nonequilibrium effects is examined, respectively.

4.1 Domain, boundary conditions and simulation parameters

The geometry and computational domain used in the study are illustrated in Fig. 4.1. Both wedges have the same length, i.e. $L_1/L_2 = 1$. The first wedge has an angle of $\theta_1 = 15°$ and the second wedge has an angle of $\theta_2 = 45°$. The corner between the two wedges is located at $x = L_1 \cdot \cos\theta_1 = 0.193$ m. A symmetry boundary condition is considered for the symmetry segment, an inviscid wall boundary condition is imposed along the walls, supersonic outflow is used at the exit and a farfield boundary condition is imposed at the remaining boundary.

The freestream conditions are summarized in Table 4.1. For the flow of air, a mixture with five species (N_2, O_2, N, O, NO) is considered, and the reaction mechanism is taken from the widely-used references of Park [78, 88]. For the CO_2-N_2 flow, a mixture with 10 species (C, N, O, C_2, N_2, O_2, CN, CO, NO, CO_2) is used, and the reaction mechanism is taken from [59]. Following the approach of Candler [56], only CO_2 and N_2 are considered as initial species. For all simulations, the freestream Mach number and pressure are, respectively, $M_\infty = 9$ and $p_\infty =$

390 Pa. The initial mass fractions are $Y_{N_2} = 0.77$ and $Y_{O_2} = 0.23$ for air and $Y_{CO_2} = 0.95$ and Y_{N_2} = 0.05 for the CO_2-N_2 flow. It is assumed that the freestream flow is in thermal equilibrium, $T_{tr,\infty}$=$T_{ve,\infty}$=T_∞. Two different values of freestream temperature are simulated: $T_\infty = 300$ K and $T_\infty = 1000$ K. The first case aims at simulating the occurrence of shock wave interference in a situation typical of external aerodynamics, in the proximity of control surfaces and/or the fuselage-canopy area, where the flow has been previously heated up by the vehicle nose shock. The higher value of freestream temperature simulates the interference phenomena in the case of internal aerodynamics of a propulsive system, for which the flow undergoes a series of shock waves before entering the system. To better understand the impact of non-equilibrium effects in this study, these simulations were also run using a calorically perfect ideal gas model (PIG) - with $\gamma = 1.4$ for air and $\gamma = 1.29$ for the CO_2-N_2 mixture. Under the calorically perfect ideal gas assumption, the type of interaction that occurs depends only on the relevant non-dimensional parameters (which for inviscid flow are freestream Mach number M_∞, wedge length ratio L_1/L_2, specific heat ratio γ, wedge angles θ_1, and θ_2) [3], and therefore, only one value of freestream temperature was used, $T_\infty = 300$ K.

Table 4.1: Simulation parameters for inviscid shock interactions over the 15°-45° double-wedge.

T_∞ [K]	300/1000
p_∞ [Pa]	390
M_∞ []	9
$Y_{CO_2\text{-}N_2}[CO_2]$	0.981
$Y_{CO_2\text{-}N_2}[N_2]$	0.019
$Y_{air5}[N_2]$	0.77
$Y_{air5}[O_2]$	0.23

4.2 Grid independence studies

Shock interactions result in complex flow structures that can only be accurately captured using very fine grids. In order to avoid the consequent excessive computational times, adaptive mesh refinement is employed in this work, so that mesh resolution is increased only where it is needed, as per Appendix B. The grid adaptation approach allows the user to adjust the following

adaptation parameters:

- *sensor* - flow variable used to calculate the metric field driving the adaptation process;
- *hgrad* - maximum allowed ratio of element sizes between adjacent elements;
- *complex* - controls the complexity and density of the mesh in specific regions, particularly in areas with intricate geometries or detailed solution features that require higher resolution.

At every iteration of the grid adaptation process, the previous parameters can be tailored to each case and solution to ensure faster grid convergence and lower computational cost. The Mach number is chosen as the *sensor* for all cases since all the flow features translate to Mach number gradient and are therefore recognized by the adaptation process. The *complex* parameter is generally kept as low as possible to minimize node and element count while maintaining accuracy. However, cases with complex shock interactions require a higher *complex* value to capture additional flow features accurately, necessitating denser grids in key interaction regions for grid convergence. The *hgrad* parameter is progressively increased during the adaptation process to ensure a balanced approach, allowing steady convergence without overly slowing it down or necessitating excessive iterations.
The baseline two-dimensional grid is an unstructured mesh composed only of triangular elements. Since in hypersonic inviscid flow shock waves are characterized by very localized and sharp gradients/discontinuities of flow properties, the mesh adaptation process automatically clusters nodes over the shock waves and gradually captures the sharp shock interaction structure. Figure 4.2 illustrates and starting and ending point of the adaptation process for the air flow over the 15°-45° double-wedge with $T_\infty = 1000$ K.

Grid convergence is assessed qualitatively, on the basis of the observation of well-defined types of shock interaction following the classification paradigm originally introduced by Edney [6]. A quantitative assessment is performed by comparing the following quantities for different levels of adaptation: 1) normalized temperature profile as a function of the normal distance from the wall δ, at a position on the surface of the second wedge where the most complex flow features are observed (as illustrated by the blue line at the right of Fig. 4.2) and 2) the normalized wall surface pressure profile. The grid adaptation process is interrupted

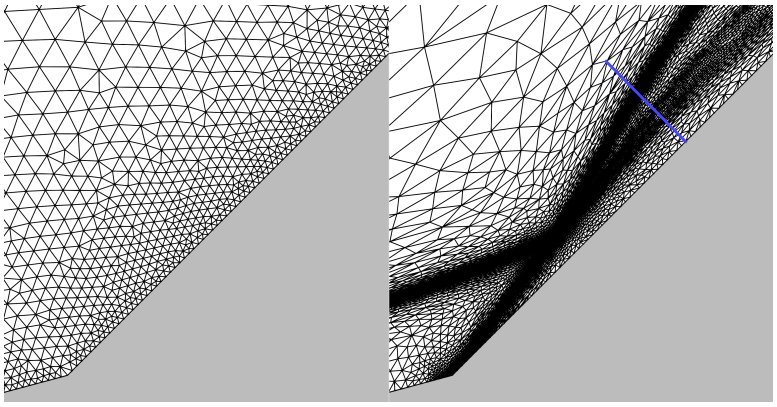

Figure 4.2: Original (left) and final adapted (right) mesh for the air-5 case with $T_\infty = 1000$ K.

when the established patterns of shock interaction do not change, which is supported by the quantitative convergence of extracted temperature and pressure profiles, normal and along the wall, respectively. Quantitative comparisons for the different iterations of adaptation, or levels of adaptation, are shown for all cases in Figs. 4.3 to 4.8. For each case, grid convergence is achieved, since results obtained for the final and second-last levels of adaptation are nearly identical for both quantities, and the very small differences that remain have no impact on the flow features associated with different shock patterns. Table 4.2 provides the number of nodes of the final grids used for each test-case. As it will be discussed in the following sections, the cases of air-5 with $T_\infty = 300$ K, and both air and CO_2-N_2 cases with a PIG model resulted in the most complex patterns of shock interaction, requiring the adaptation parameter *complex* to be increased. Accordingly, the grid adaptation process resulted in a significantly larger number of nodes for those cases.

Table 4.2: Number of grid nodes used in the final mesh of each test-case.

	$T_\infty = 300$ K	$T_\infty = 1000$ K	PIG
air	1,135,674	645,721	1,712,869
CO_2-N_2	385,273	480,241	1,919,397

4.3 Impact of the freestream temperature

In this section, shock interaction patterns in nonequilibrium flows over double-wedge geometries are discussed for different mixtures and values of the freestream temperature. In the first

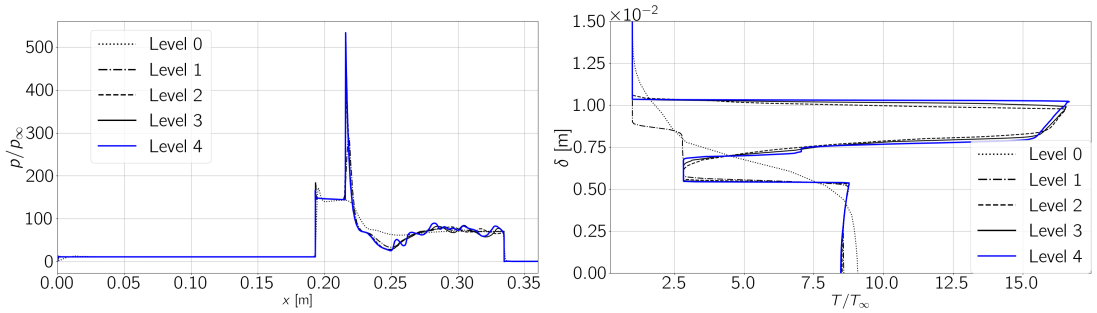

(a) Normalized surface pressure.

(b) Normalized translational temperature profile normal to the surface of the aft wedge.

Figure 4.3: Grid convergence plots for the nonequilibrium air-5 case with $T_\infty = 300$ K.

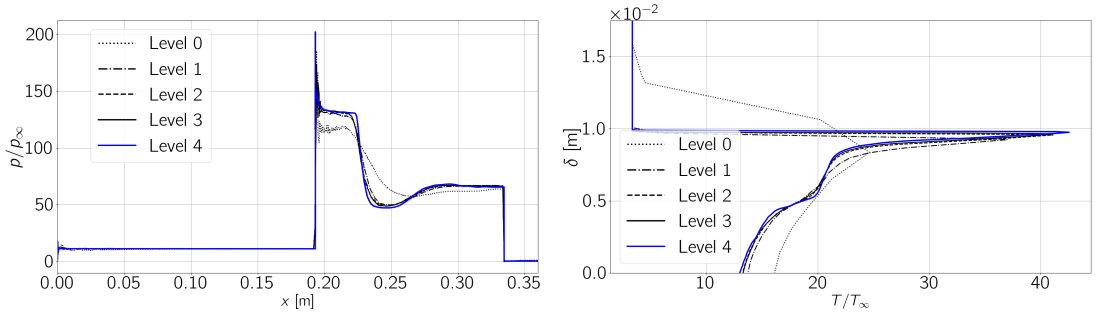

(a) Normalized surface pressure.

(b) Normalized translational temperature profile normal to the surface of the aft wedge.

Figure 4.4: Grid convergence plots for the nonequilibrium air-5 case with $T_\infty = 1000$ K.

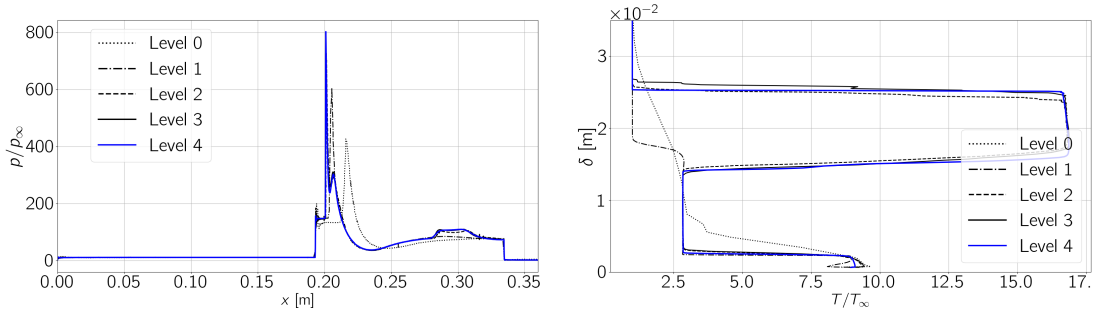

(a) Normalized surface pressure.

(b) Normalized temperature profile normal to the surface of the aft wedge.

Figure 4.5: Grid convergence plots for the air case with a PIG model.

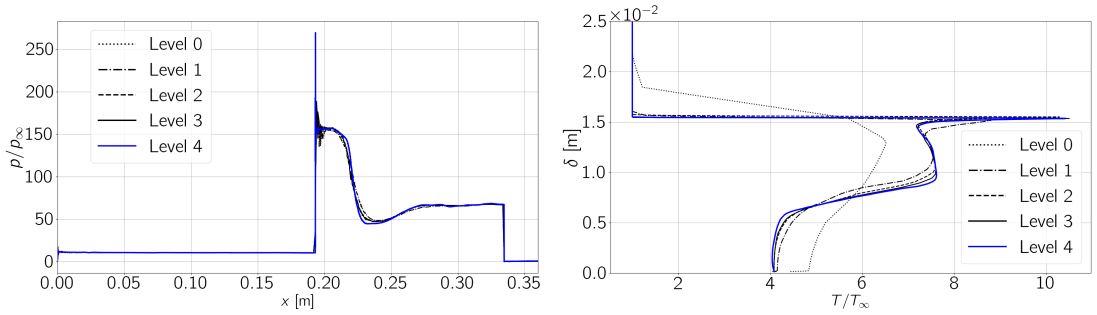

(a) Normalized surface pressure.

(b) Normalized translational temperature profile normal to the surface of the aft wedge.

Figure 4.6: Grid convergence plots for the nonequilibrium CO_2-N_2 case with $T_\infty = 300$ K.

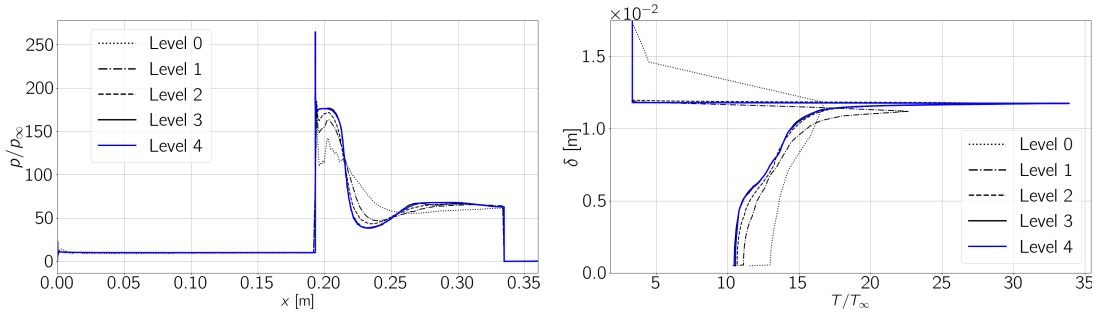

(a) Normalized surface pressure.

(b) Normalized translational temperature profile normal to the surface of the aft wedge.

Figure 4.7: Grid convergence plots for the nonequilibrium CO_2-N_2 case with $T_\infty = 1000$ K.

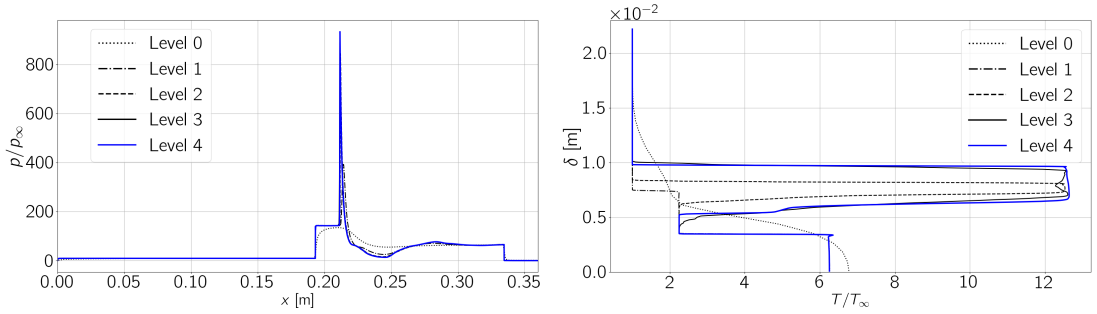

(a) Normalized surface pressure.

(b) Normalized temperature profile normal to the surface of the aft wedge.

Figure 4.8: Grid convergence plots for the CO_2-N_2 case with a PIG model.

set of test-cases, a mixture of air 5-species is considered. Figure 4.9 shows the normalized pressure and a numerical schlieren of the flowfield. For a freestream temperature of $T_\infty = 300$ K, a type V interaction with a six-shock configuration is obtained. Figure 4.10 shows a zoom of the shock interaction pattern, with normalized pressure contours and streamlines, to allow for a better understanding of the type V pattern and highlight the effect of the different flow features on the flow direction. This interaction is characterized by one triple-point P, as shown in the schematic illustrated in Fig. 4.11a. Point P is where the nose shock and the bow shock intersect, and from which a transmitted shock PT emerges in a Mach reflection structure. The latter shock interacts with the oblique shock generated by the corner between the two wedges (shock TB), causing shock PT to reflect as shock TU and shock TB to reflect as shock TR in a regular reflection structure. The reflection of these two shocks from opposite families is one of the key features in the type V six-shock interaction. Downstream of the corner between the two wedges, shock TR undergoes a regular reflection on the surface of the second wedge and gives rise to shock RQ. A contact discontinuity - only seen in numerical schlieren - emanates from the triple-point P. Shock TU reflects on the contact discontinuity as an expansion wave that, in turn, merges with the reflected shock RQ, which further downstream is reflected on the contact discontinuity as an expansion wave. The two expansion fans can be seen in both the normalised pressure contours (transition from red–yellow–green–light blue) and in the numerical schlieren. As the freestream temperature is raised to $T_\infty = 1000$ K, the shock interaction pattern completely changes and a type VI interaction is obtained, with a schematic shown in Fig. 4.11b. Results for normalized pressure contours and numerical schlieren are shown in the bottom images of Fig. 4.9 - note the different scale of the normalized pressure contours relative to the previous case. In this type of interaction, the flow is purely supersonic and oblique shock waves originating in the two corners directly intersect in point P, resulting in the appearance of a contact discontinuity that separates the flow that has passed through both shocks from the one that has passed through the second shock BP only. An expansion fan is emitted from the oblique shock intersection and reflected on the surface of the second wedge (transition of pressure contours from red to yellow). Some of the reflected expansion waves are deflected as they cross the contact discontinuity, and intersect with the oblique shock PS, weakening it. The remaining expansion waves are instead reflected on the contact discontinuity as compression waves, recompressing the fluid along the

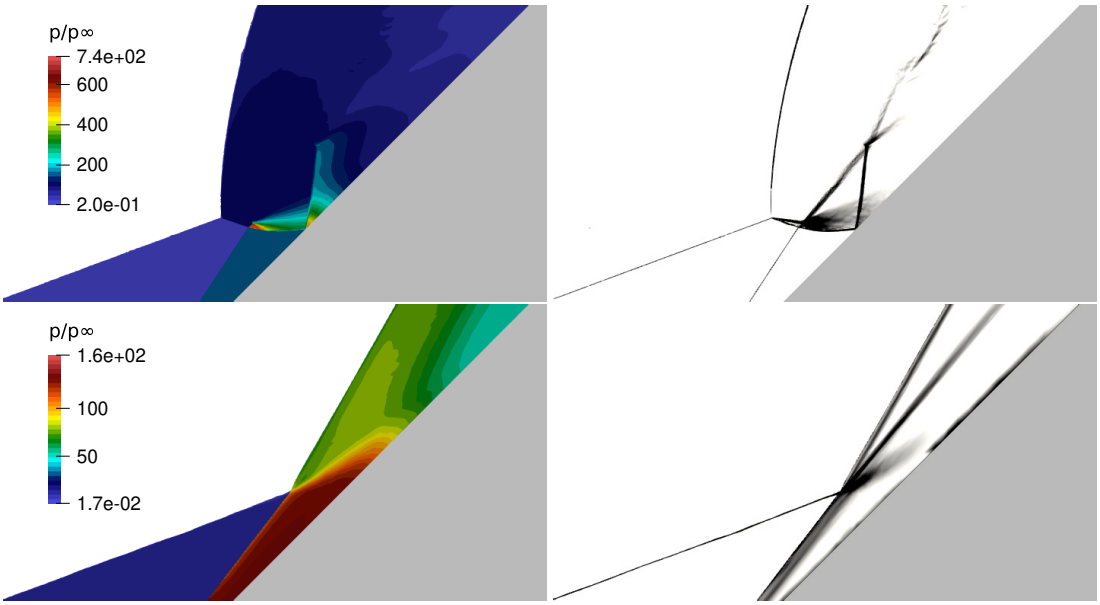

Figure 4.9: Nonequilibrium air-5 flow over the 15°-45° double-wedge. Normalized pressure p/p_∞ (left), numerical schlieren (right); From top to bottom: $T_\infty = 300$ K, $T_\infty = 1000$ K.

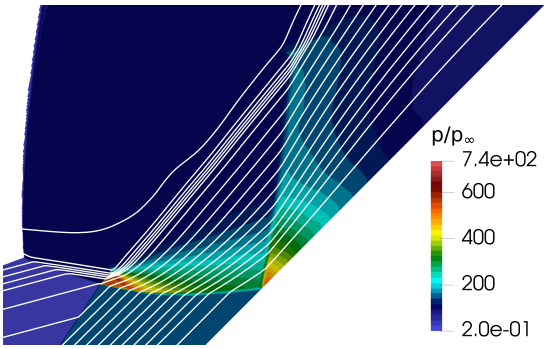

Figure 4.10: Nonequilibrium air-5 flow over the 15°-45° double-wedge. Normalized pressure p/p_∞ and streamlines for $T_\infty = 300$ K.

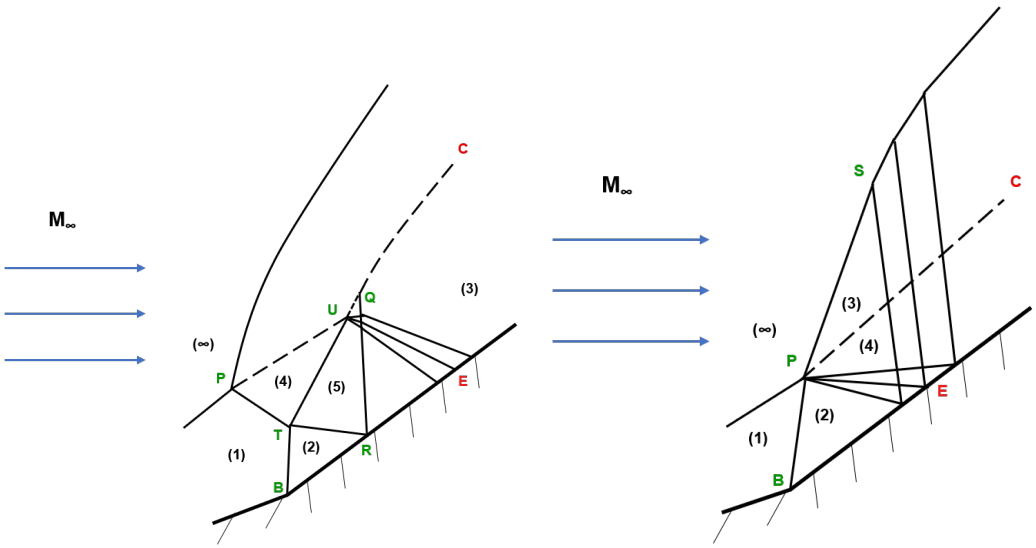

(a) Six-shock type V inviscid interaction [89].

(b) Type VI inviscid interaction [89].

Figure 4.11: Schematics of inviscid shock interaction patterns obtained for the nonequilibrium cases.

surface of the second wedge (green tp light blue pressure contours). The completely different shock interaction structures obtained for the nonequilibrium air-5 cases show that the freestream temperature parameter has a major influence on the patterns of interaction for this mixture. The larger freestream temperature of the latter case leads to a higher degree of dissociation and vibrational excitation of the molecules, resulting in a weaker shock interaction that is more attached to the wall. A more detailed discussion of the role of nonequilibrium effects follows in the next section.

In the second set of test-cases, the CO_2-N_2 mixture is considered. Figure 4.12 shows the shock interaction patterns obtained for this mixture. While a different pattern of interaction is obtained for $T_\infty = 300$ K relative to the air-5 case (six-shock type V for air-5 vs. type VI for CO_2-N_2), an identical pattern is seen for $T_\infty = 1000$ K (type VI). For the CO_2-N_2 mixture, both values of freestream temperature result in the supersonic type VI shock interaction, described in the previous paragraph. The differences in flow features observed between these two cases are relatively small. The shock angles differ slightly, and the interaction pattern is more attached to the wall as the freestream temperature is increased from 300 K to 1000 K in the case of CO_2. It is relevant to notice that, even though the corner shock angle is smaller for $T_\infty = 1000$ K, a

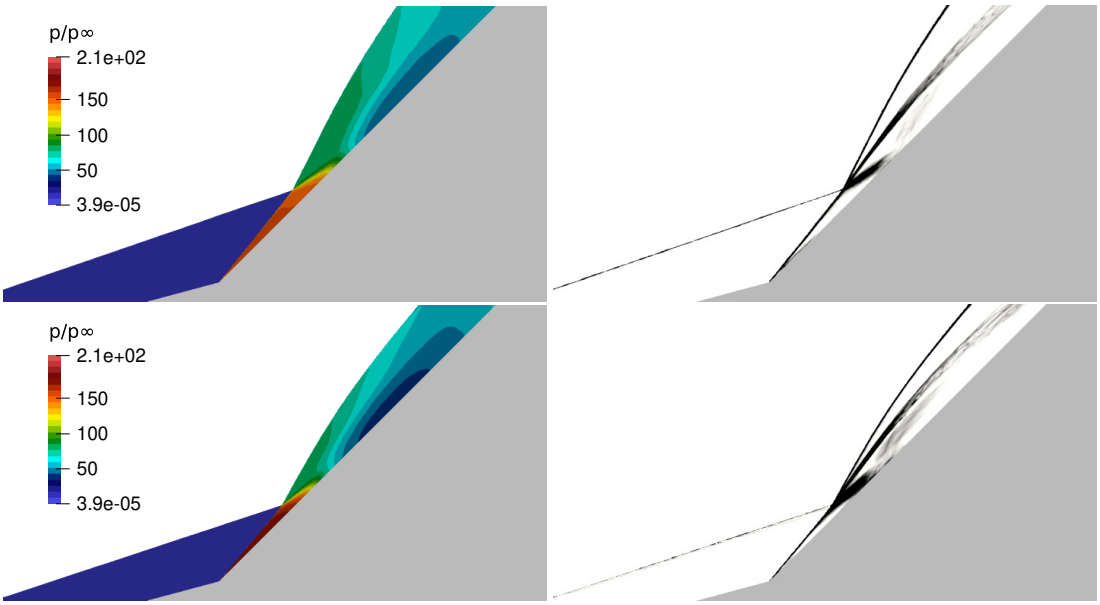

Figure 4.12: Nonequilibrium CO_2-N_2 flow over the 15°-45° double-wedge. Normalized pressure p/p_∞ (left), numerical schlieren (right); From top to bottom: $T_\infty = 300$ K, $T_\infty = 1000$ K.

higher post-shock pressure is obtained, contrary to what would be expected. As discussed in the next section, this is a result of nonequilibrium effects. The results shown in Figs. 4.9 and 4.12 reveal that the impact of the freestream temperature on the shock pattern is much smaller for this mixture than for air-5. The next section discussing the role of nonequilibrium effects in the two different mixtures will further explore these differences.

Figure 4.13 shows a comparison of the normalized surface pressure between the four cases. The stronger pressure peak associated to the stronger and more complex type V interaction pattern obtained for the air-5 case with $T_\infty = 300$ K is evident in the plot, at $x = 0.216$ m. For this interaction pattern, the higher pressure peak results from the regular reflection of shock TR on the surface of the aft wedge, whereas for the cases showing a type VI pattern, the pressure peak occurs at the corner between the two wedges at $x = 0.193$ m and is a consequence of the oblique shock generated at this location. The fluctuations observed in the air-5 case with $T_\infty = 300$ K downstream of $x = 0.25$ m suggest that the contact discontinuity might have some instability. To further investigate this, unsteady simulations would need to be performed. However, this occurs downstream of the steady pattern of shock interaction and therefore is out of the scope of this work. Some of the differences between the type VI cases are the location where the

expansion fan hits the wall, which occurs further upstream for CO_2-N_2 with $T_\infty = 300$ K, then for CO_2-N_2 $T_\infty = 1000$ K and further downstream for air-5 with $T_\infty = 1000$ K. The pressure plateau obtained downstream of the corner shock also differs slightly, with a stronger pressure load seen for CO_2-N_2 with $T_\infty = 1000$ K, which, as mentioned in the previous paragraph, is contrary to what would be expected.

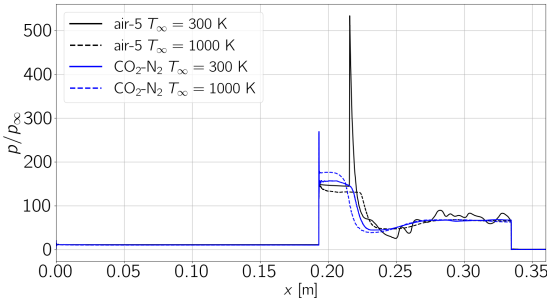

Figure 4.13: Comparison of normalized surface pressure profiles for inviscid shock interactions.

4.4 Nonequilibrium effects

To gain a thorough understanding of the role of nonequilibrium effects on the shock interaction flows investigated in this chapter, additional simulations were performed considering a calorically perfect ideal gas model (PIG). This model considers that the gas is in equilibrium, under the assumption that both chemistry and vibrational excitation are frozen (i.e., there is no translational-to-vibrational internal energy transfer). Using a PIG model, the freestream temperature has no influence on the pattern of shock interaction [3], therefore only the value of $T_\infty = 300$ K was simulated. Figure 4.14 shows contours of normalized temperature for the PIG cases and contours of normalized translational temperature for the nonequilibrium cases, both for air and CO_2-N_2 flows. For both mixtures, considering a PIG model drastically changes the pattern of interaction, exposing the influence that nonequilibrium physics has in the type of flows.

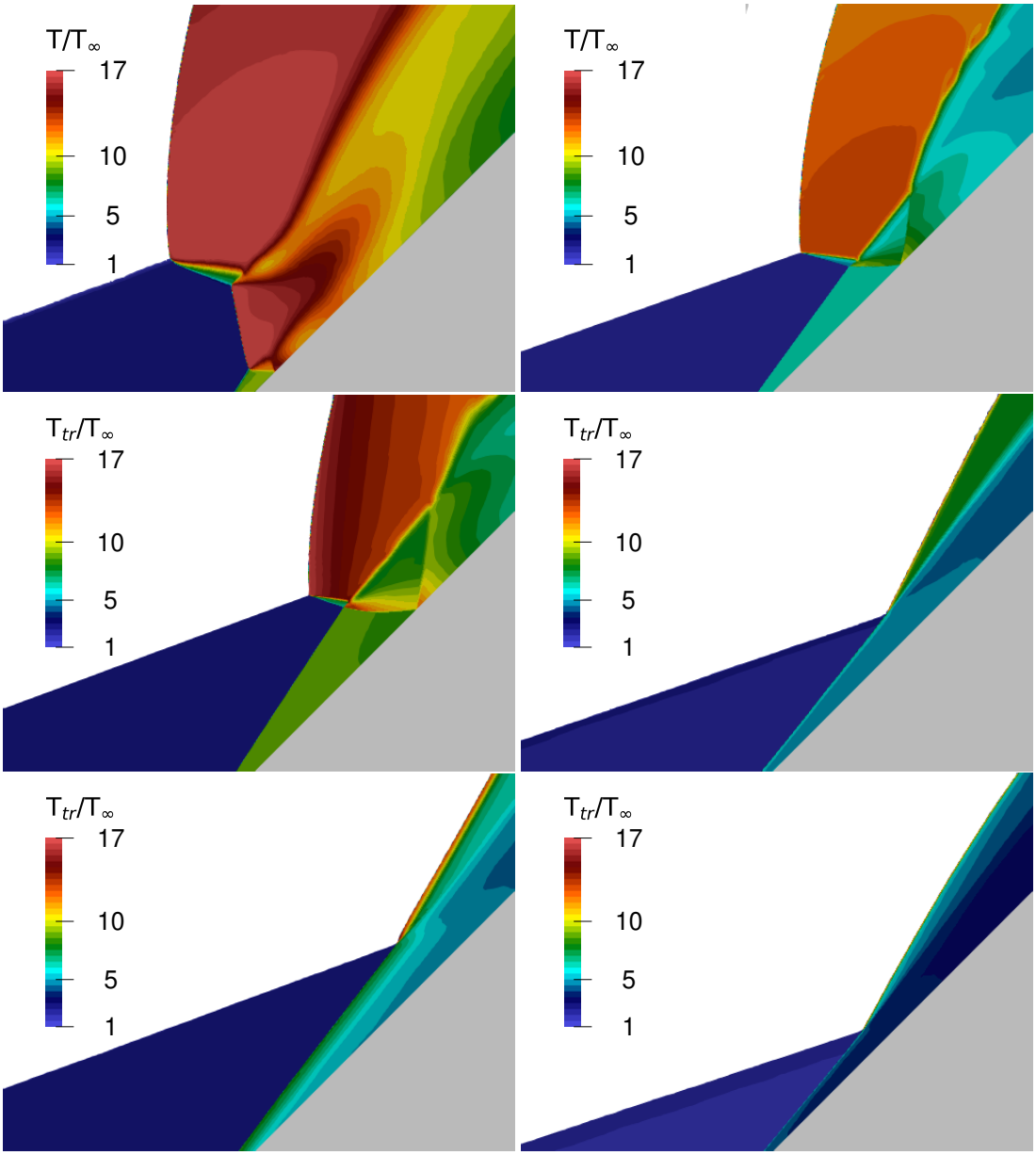

Figure 4.14: Air (left) and CO_2-N_2 (right) flows over the 15°-45° double-wedge: normalized temperature contours; From top to bottom: PIG, $T_\infty = 300$ K, $T_\infty = 1000$ K.

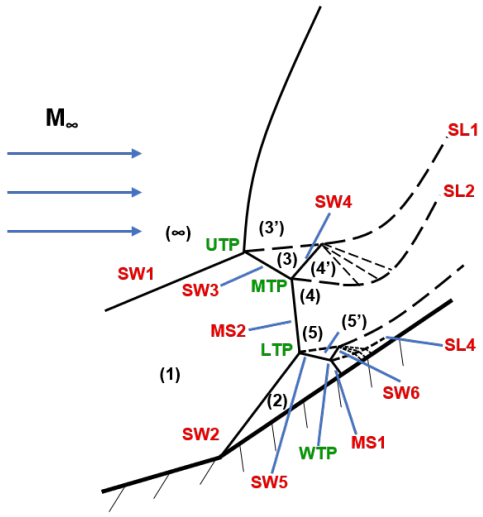

Figure 4.15: Schematic of the inviscid nine-shock type V interaction pattern.

For the air case, using a PIG model results in a nine-shock type V interaction. The schematic provided in Fig. 4.15 is used to analyse the pattern obtained numerically. This interaction is characterized by four triple-points. The upper triple-point UTP is the intersection between the first oblique shock, the bow shock and the transmitted shock SW3. The interaction of shock SW3 and the oblique shock generated in the corner between the two wedges - shock SW2 - results in a Mach reflection denoted by MS2, which gives rise to the mid triple-point MTP (connecting SW3, MS2 and SW4). The lower triple-point LTP concerns what is usually described as a lambda shock interaction, connecting MS2, the oblique shock from the corner between the two wedges SW2 and shock SW5. In this type of interaction, the flow is not able to meet both pressure equilibrium and flow tangency constraints with an incident and a reflected shock at the wall, which results in the reflection of shock SW5 on the surface of the second wedge as a normal shock in a second Mach reflection, giving rise to shock SW6 and the wall triple-point WTP. From the upper and mid triple-points, UTP and MTP respectively, two slip layers, SL1 and SL2 are emitted, bounding a thick contact surface. Furthermore, a third slip layer SL3 is emitted from the lower triple-point LTLP. Just behind the Mach reflection between the mid and lower triple-points, MTP and LTP respectively, slip layers SL2 and SL3 assemble a converging stream tube. Shock SW4 is reflected on the slip layer SL1 as an expansion wave, turning the slip layer SL1 upward. Further downstream, this expansion wave impinges on the slip layer SL2, which is turned upward and lets the stream tube bounded by SL2 and SL3 diverge. This

converging-diverging stream tube is a typical feature of the type V nine-shock configuration. The reflection of shock SW6 on the slip layer SL3 emits an expansion wave that makes SL3 turn upward. The flow between this contact discontinuity and the surface of the second wedge then undergoes a series of alternating isentropic compression and expansion waves, behaving as an underexpanded jet with regard to the adjacent flow region. As seen by the contours of normalized temperature in Fig. 4.14, the nine-shock type V shock interaction is characterized by the largest temperature jumps across the different shock waves (the largest temperature jump being between the freestream flow and the region behind the bow shock), strong shock waves forming Mach reflections and a bow shock with the largest standoff distance (with respect to the wall of the second wedge).

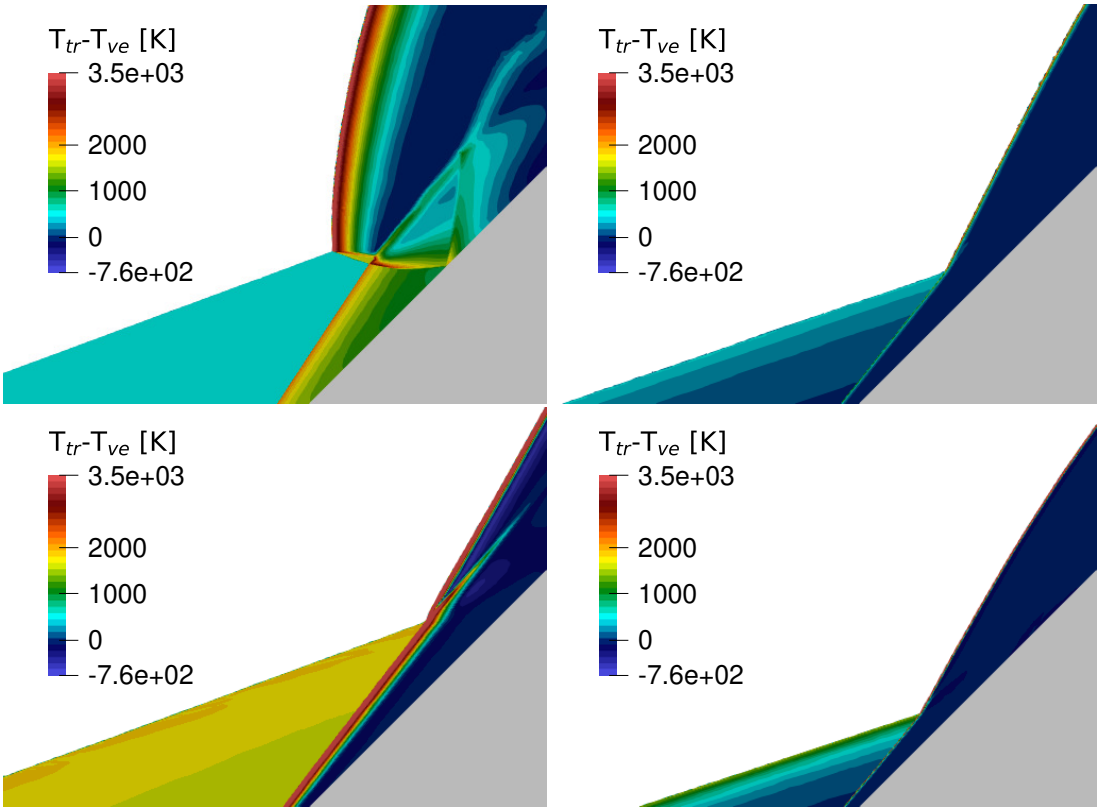

Figure 4.16: Air (left) and CO_2-N_2 (right) flows over the 15°-45° double-wedge: degree of thermal nonequilibrium; From top to bottom: $T_\infty = 300$ K, $T_\infty = 1000$ K.

For the CO_2-N_2 case, modelling nonequilibrium effects to accurately represent the physics in this type of flows is also key. Differently from both nonequilibrium cases that result in a type VI interaction, simulating this flow with a PIG model leads to a stronger interaction, the six-shock

type V described in the previous section (see Fig. 4.11a). As also mentioned in the previous section when discussing Fig. 4.12, the differences in flow features observed between the two nonequilibrium cases are relatively small. However, relative to the $T_\infty = 300$ K case, the effect of vibrational relaxation has a larger impact on the region of the contact discontinuity. Whereas the numerical schlieren clearly reveals a slip layer in both nonequilibrium cases, the contours of translational temperature do not show it for the $T_\infty = 1000$ K case (the slip layer is also quite faded in the air case with $T_\infty = 1000$ K). This a direct result of the more prominent vibrational-to-translational energy transfer that gradually occurs at the microscopic level as the gas relaxes towards thermal equilibrium.

From a global analysis of Fig. 4.14, it is possible to conclude that, as nonequilibrium effects become more relevant, the pattern of interaction tends to be weaker and less complex. This trend is seen when the freestream temperature is increased from 300 K to 1000 K (in the nonequilibrium cases), which is associated with a higher degree of thermal nonequilibrium and chemical activity behind the shocks, as well as when comparing a PIG model to the nonequilibrium one. When vibrational excitation and chemical dissociation are accounted for and occur in a more predominant way, a larger amount of the kinetic energy of the flow is converted into vibrational and chemical energy, respectively. As a result, the shocks are less strong, the internal translational energy behind the shocks is smaller and so is the temperature (translational).

Figure 4.16 shows contours of the difference between translational and vibrational temperatures, which is a measure of thermal nonequilibrium. It is evident that, for the CO_2-N_2 cases, the flow is mostly in thermal equilibrium downstream of the corner oblique shock. The lower characteristic vibrational temperature of the double degenerate mode of the triatomic molecule [56], compared to the vibrational modes of N_2 and O_2, results in a much faster vibrational relaxation. This difference in speed of vibrational relaxation between the two mixtures is seen more evidently just behind the first oblique shock. In this region, for both values of freestream temperature, the air contours change very little or do not change at all, like in the case of $T_\infty = 300$ K. This behaviour is opposed to what is seen for the CO_2-N_2 mixture, where a clear gradient is obtained behind this shock (sharper gradient for $T_\infty = 1000$ K) up to the point of reaching thermal equilibrium. Despite the fact that the CO_2-N_2 flow is mostly in thermal equilibrium downstream of the corner shock, there is a very thin region of strong thermal nonequilibrium

(not visible in the image) just behind the bow shock, where the difference between translational and vibrational temperature reaches 3,531 K for $T_\infty = 300$ K and 12,404 K for $T_\infty = 1000$ K. Larger freestream temperatures are associated with more drastic temperature jumps across the shocks, which in turn results in faster internal energy transfer. The slower relaxation for $T_\infty = 300$ K leads to a thin region of thermal nonequilibrium just behind the bow shock that is slightly visible, as opposed to the $T_\infty = 1000$ K case. This trend is more obvious in the contours for the air case where, for $T_\infty = 300$ K, a much larger region of the flow is found to be in thermal nonequilibrium, relative to the higher freestream temperature case. Even though thermal equilibrium tends to be reached faster in cases where the freestream temperature is larger, the degree of thermal nonequilbrium just behind the bow shock is stronger, with a maximum of $T_{tr} - T_{ve} = 4,434$ K for $T_\infty = 300$ K and $T_{tr} - T_{ve} = 13,377$ K for $T_\infty = 1000$ K.

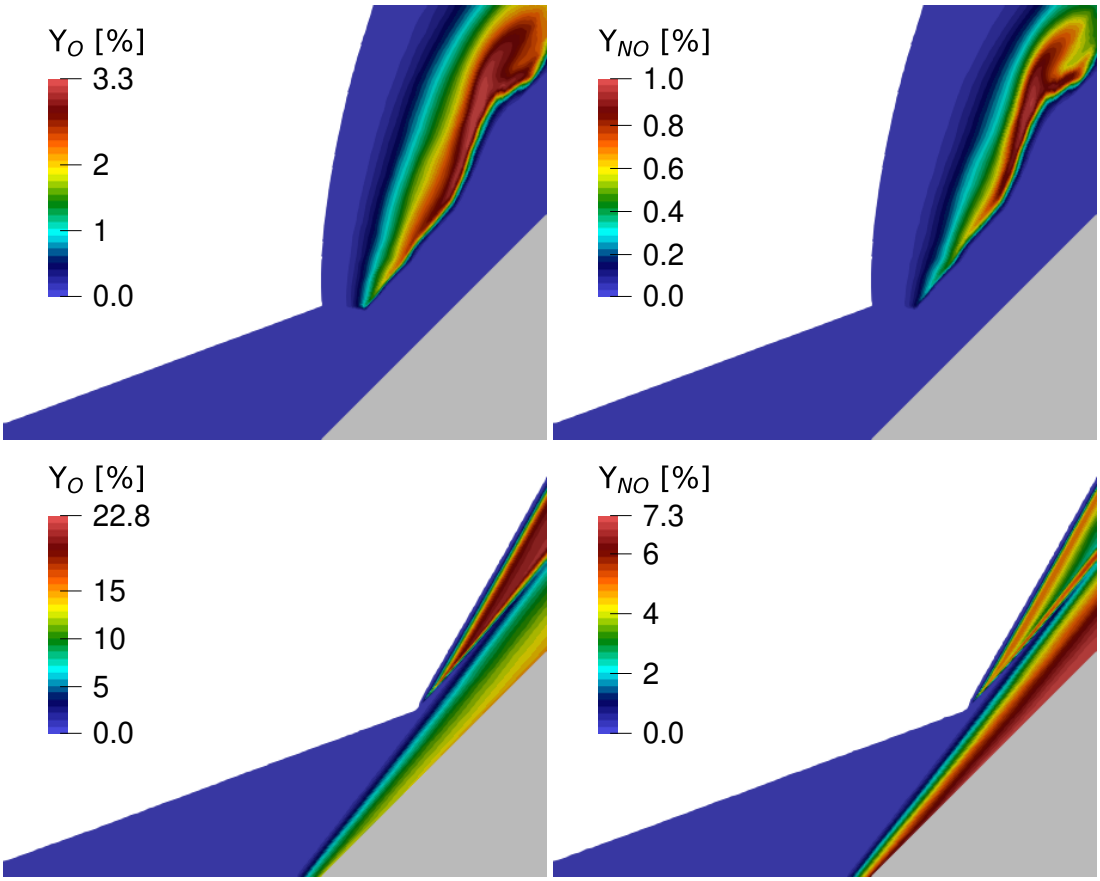

Figure 4.17: Air flow over the 15°-45° double-wedge: O (left) and NO (right) mass fraction contours; From top to bottom: $T_\infty = 300$ K, $T_\infty = 1000$ K.

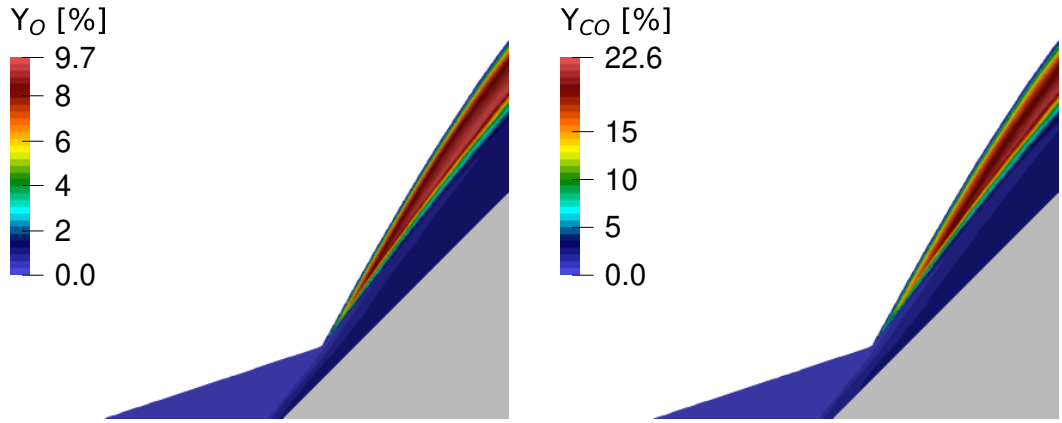

Figure 4.18: CO_2-N_2 flow over the 15°-45° double-wedge: O (left) and CO (right) mass fraction contours, with $T_\infty = 1000$ K.

Figure 4.17 shows the percentage mass fractions for O and NO species in the case of the air flow, for $T_\infty = 300$ K and $T_\infty = 1000$ K. Figure 4.18 shows the percentage mass fractions for CO and O species in the CO_2-N_2 flow, for $T_\infty = 1000$ K. For the remaining test-case, $T_\infty = 300$ K with the CO_2-N_2 mixture, no results are shown since the flow is chemically frozen. With $T_\infty = 300$ K, the flow is chemically frozen for the CO_2-N_2 mixture, whereas in the case of air O_2 and N_2 dissociation, as well as NO formation, take place. Just behind the bow shock there is a region of chemical incubation. Further downstream, the chemical species resulting from chemical reactions (N, O, NO) start to form, with most of the chemical activity occurring between slightly downstream of the bow shock and the contact discontinuity. As the freestream temperature is increased to $T_\infty = 1000$ K, the occurrence of chemical reactions increases substantially - with the maximum mass fraction of O changing from 3.3% to 22.8%, and the maximum mass fraction of NO changing from 1% to 7.3%. For $T_\infty = 1000$ K, the percentage of NO is small in regions where there is more atomic oxygen (between the bow shock and the contact discontinuity). The increasing percentage of atomic oxygen and nitrogen behind the bow shock results in the occurrence of NO formation, which then becomes more relevant in the near-wall region (where atomic oxygen is seen to be more scarce).

Figure 4.18 shows the percentage of mass fractions for CO and O species in the case of the CO_2-N_2 flow, for $T_\infty = 1000$ K. At this value of freestream temperature, as opposed to $T_\infty = 300$ K, there is enough energy to break the bonds of CO_2 molecules, resulting in a maximum mass

fraction of 22.6% of CO and 9.7% of atomic oxygen. Even though contours are only shown for CO and O mass fractions, other reactions occur: oxygen recombination with a maximum O_2 percentage of 4.6%, N_2 dissociation with a maximum N_2 percentage of 0.17% and NO formation with a maximum NO percentage of 0.19%. The amount of energy in the flow is not sufficient to trigger CO dissociation, as there are no atoms of carbon. For this mixture, the occurrence of dissociative chemical reactions appears to have a non-negligible influence on the post-shock pressures. Even though, for the higher freestream temperature, the shock waves for this mixture display slightly smaller shock angles, the maximum pressure behind the oblique shock generated in the corner between the two wedges increases (see Fig. 4.13). As dissociation starts to occur and more particles are present in the flow, the density jump across the oblique shock increases, and consequently the pressure jump increases as well.

As explained in 3.1.2, a simple non-preferential dissociation model is employed to address the chemical-vibrational coupling. The latter model assumes that molecules can be dissociated from all vibrational states, which may be valid for situations where the free-stream kinetic energy per unit mass is much larger than the dissociation energies of the molecules [77]. In preferential dissociation, on the other hand, it is considered that molecules dissociate more easily when they are vibrationally more excited. Molecules must "ladder climb" from lower to higher vibrational states to be dissociated. As a result, dissociation reactions are delayed, and vibrational temperature tends to be lower during the relaxation process, when compared to non-preferential dissociation [33]. It is possible that using a preferential dissociation model in this study would have had an impact on the results. Given the different assumptions of the preferential and non-preferential model, less dissociation would occur, with lower vibrational temperatures, stronger thermal non-equilibrium would be obtained for each case. According to what is observed in this chapter, that would mean delaying the trend that has been shown as temperature rises. Further studies employing this model would be required to understand if this would have a significant impact on the shape of the interactions patterns or even change them.

Table 4.3 shows the summary of shock interactions patterns obtained in the previous analysis:

Table 4.3: Inviscid shock interactions: summary of shock interaction patterns.

Mixture	PIG model	Nonequilibrium model $T_\infty = 300$ K	Nonequilibrium model $T_\infty = 1000$ K
air-5 species	type V 9-shock	type V 7-shock	type VI
CO_2-N_2	type V 7-shock	type VI	type VI

Chapter 5

Viscous laminar shock interactions

In this chapter, the study of shock interactions resulting from CO_2-N_2 flows over double-wedges is extended to include the modelling of transport phenomena (mass diffusion, viscosity and thermal conductivity). Although the interaction of strong shock waves dominates the hypersonic flow over a double-wedge, the near-wall region is heavily affected by viscous effects, which in turn may change the mechanism of shock interaction further from the wall. As detailed in Section 1.1, a viscous double-wedge flow gives rise to flow features such as boundary layer, flow separation, recirculation, viscous slip layers, etc. The main focus of this chapter is to investigate the interaction between the viscous flow features and the shock wave system, as well as their role in the overall mechanism of shock interaction and surface aerothermal loads.

The first and second sections of this chapter present the CFD set-up and grid independence approach employed for the simulation of viscous flow, respectively. The remaining of the chapter is divided in two parts, study I and study II. In study I, Section 5.3, viscous laminar shock interactions are simulated with the nonequilibrium two-temperature model over four different double-wedge geometries. In the previous chapter, it was concluded that, despite the small degree of thermal nonequilibrium encountered in the case of CO_2-N_2 for most part of the flow, it still has a significant impact on the inviscid pattern of interaction. With the aim to further investigate the role of vibrational relaxation in these flows, the viscous laminar numerical results obtained with the two-temperature model are compared to results obtained using different assumptions to model the behaviour of internal energy transfer (the calorically perfect ideal gas model and the thermally perfect ideal gas model)

In study II, reported in the fourth part of this chapter, Section 5.4, the response of hypersonic viscous shock interactions to changes in the freestream flow is analysed. The freestream Mach number is known to strongly influence the shape and angles of shock waves, as well as flow regions where viscous effects play a significant role. A parametric study is conducted to characterize the viscous nonequilibrium shock interaction in CO_2-N_2 flows over double-wedges with respect to Mach number and the same four different geometries.

5.1 Domain, boundary conditions and simulation parameters

The numerical studies in this chapter are performed for hypersonic laminar viscous CO_2-N_2 flow over the double-wedge geometry illustrated in Fig. 4.1. Four different configurations are simulated by increasing the aft wedge angle θ_2 from 40° to 55° in increments of 5° , with $\theta_1 = 15°$. The wedge length ratio remains the same $L_1/L_2 = 1$, with $L_1 = L_2 = 0.2$ m. The two wedge surfaces and the expansion surface downstream of the expansion corner are assumed to be isothermal walls. For the leftmost horizontal segment, a symmetry boundary condition is applied. An outlet boundary condition is chosen for the exit and farfield is considered for the remaining boundaries. Numerical simulations are performed for a flow of CO_2:97%, N_2:3% (mole fractions) referring to the atmosphere of Mars.

The simulation parameters for the study I are presented in Table 5.1. Freestream conditions are chosen so that the flow is in the laminar continuum regime, chemistry is frozen and for values of pressure and temperature that can be found in the Martian atmosphere. The freestream flow is assumed to be in thermal equilibrium. The same freestream conditions are simulated with a nonequilibrium two-temperature model (NEQ), a thermally perfect gas model (TPG) and a perfect ideal gas model (PIG).

Table 5.1: Simulation parameters for study I.

T_∞ [K]	160
p_∞ [Pa]	10
M_∞ []	9
Re_∞ [-]	55105
$Y[CO_2]$	0.98
$Y[N_2]$	0.02
T_{wall} [K]	300

For study II, additional freestream conditions are simulated by decreasing and increasing the Mach number, as per the table below:

Table 5.2: Simulation parameters for study II.

T_∞ [K]	160
p_∞ [Pa]	10
M_∞ [-]	7, 9, 11
$Y[CO_2]$	0.98
$Y[N_2]$	0.02
T_{wall} [K]	300

5.2 Grid independence studies

For the numerical studies carried out in this chapter, the mesh adaptation approach reported in Section 4.2 is adjusted to account for the flow features resulting from viscous effects, particularly the presence of a boundary layer in the near-wall region. For the viscous simulations, the baseline grid is a hybrid mesh, with an structured region along the geometry surface and an isotropic unstructured region for the rest of the computational domain, as illustrated in Fig. 5.1, at the left.

The unstructured mesh adaptation process used for the inviscid simulations is combined with a boundary layer generation tool. The tool adapts the tangential size of elements at the wall and allows to, at every iteration of the adaptation process, modify the number of structured mesh layers, height of the first layer and exponential growth factor for the element heights. The height of the first layer of elements providing convergence of the surface quantities for the final adapted grid is 1×10^{-6} m. The final adapted grid for the case of the 15°-50°double-wedge with the thermally perfect gas model is shown in Fig. 5.1 at the right. For cases where the flow turns out to be unsteady, adaptation is done isotropically and uniformly in the unsteady flow region to capture the moving shock interaction structure accurately.

Grid convergence in the viscous simulations is assessed qualitatively, on the basis of the establishment of a given shock interaction pattern, and quantitatively, by comparing normalized wall surface pressure, wall surface heat flux and the normalized temperature profile normal to the wall at two given locations where relevant flow features are present. These two locations

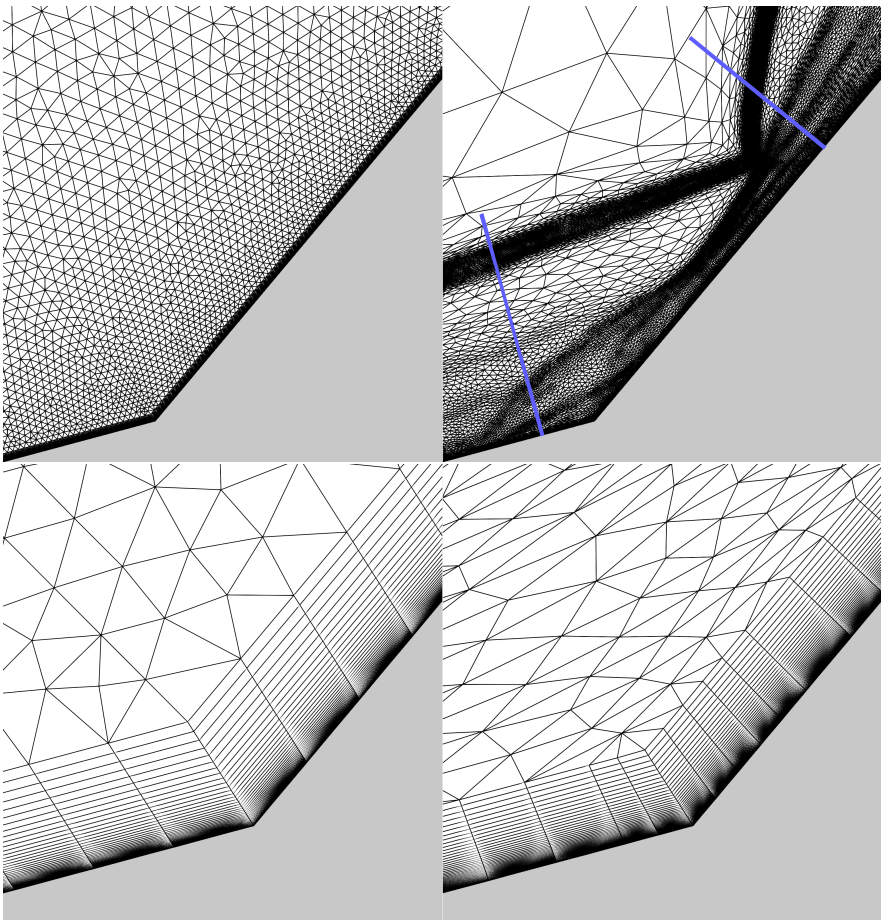

Figure 5.1: Zoomed views, in the corner between the two wedges, of the original (left) and final adapted (right) hybrid grids for the 15°-50°case simulated with a thermally perfect gas model.

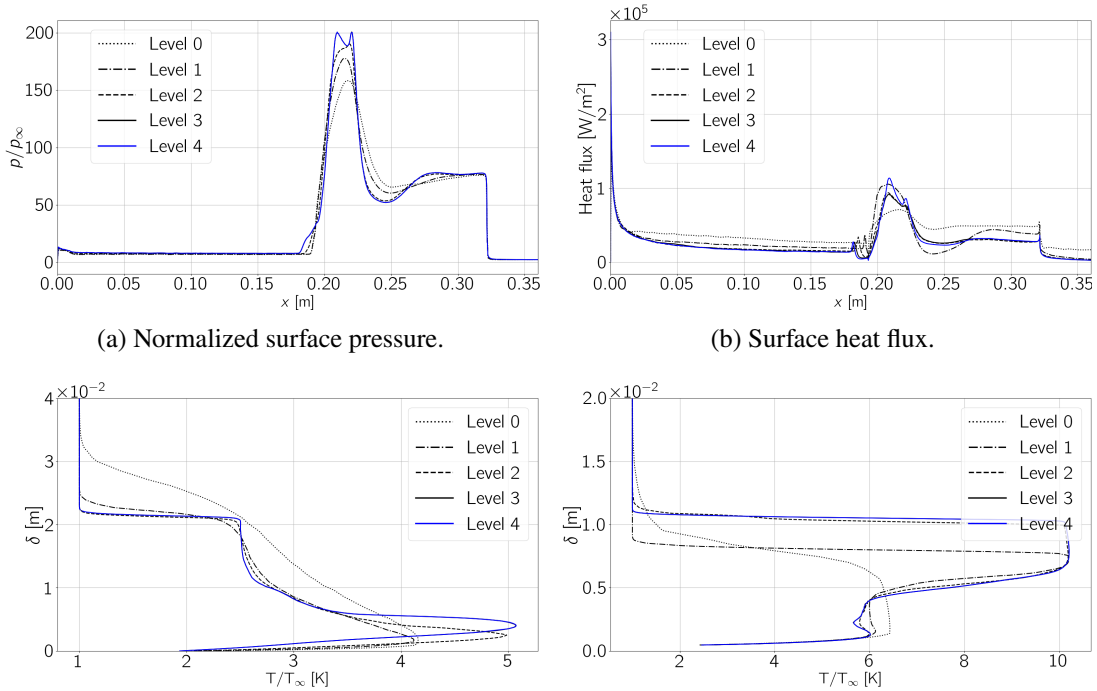

(a) Normalized surface pressure.

(b) Surface heat flux.

(c) Normalized translational temperature profile normal to the surface of the aft wedge at location 1.

(d) Normalized translational temperature profile normal to the surface of the aft wedge at location 2.

Figure 5.2: Grid convergence plots for the 15°-50°case with the thermally perfect gas model.

are indicated by the blue lines in Fig. 5.1. The first line, in location 1, captures a region where viscous effects are dominant and crosses the boundary layer along the surface of the first wedge and the separated flow region in the vicinity of the corner between the wedges. Following the approach used for inviscid flow, the second line, in location 2, is chosen to be in the region where the main shock interaction occurs. A grid convergence study was performed for all test-cases, but for simplicity, only the case of the 15°-50°double-wedge with the thermally perfect gas model is showcased here. Quantitative comparisons for the different levels of adaptation are displayed in Fig. 5.2, showing grid convergence.

Table 5.3 provides the number of nodes of the final grids used for the different test-cases of study I, in terms of geometry and gas model. Table 5.4 provides the number of nodes of the final grids used for the different test-cases of study II, in terms of geometry and Mach number. The cases for which the final grids have a significantly larger number of nodes correspond to those for which the most complex patterns of shock interaction, including unsteady flow dynamics, were

obtained.

Table 5.3: Number of grid nodes used in the final mesh of each test-case for study 1.

	NEQ	TPG	PIG
15°-40°	488,355	544,868	463,667
15°-45°	530,124	542,206	442,588
15°-50°	422,547	448,061	2,634,430
15°-55°	2,691,616	2,500,575	2,462,622

Table 5.4: Number of grid nodes used in the final mesh of each test-case for study II.

	$M_\infty = 7$	$M_\infty = 9$	$M_\infty = 11$
15°-40°	138,066	488,355	526,679
15°-45°	478,233	530,124	374,324
15°-50°	489,396	422,547	498,411
15°-55°	1,090,778	2,691,616	651,005

5.3 Role of vibrational relaxation

This section investigates the influence of vibrational relaxation on the patterns of shock interaction and surface loads occurring in carbon-dioxide flows over double-wedge configurations. In order to isolate the effect of vibrational relaxation and ensure that nonequilibrium processes happening in the flow are exclusively due to internal energy exchanges between different degrees of freedom of particles in the gas, flow conditions are adjusted to produce a flow in thermal nonequilibrium where chemical reactions are not activated.

A computational analysis is performed to simulate a viscous hypersonic CO_2-N_2 flow over four different double-wedge configurations. A detailed discussion on the nonequilibrium mechanisms of shock interaction is presented in Section 5.3.2, with computational results obtained using the two-temperature model described in Chapter 3.

The impact of vibrational relaxation on shock interaction patterns is investigated through a comparative analysis. Results obtained from nonequilibrium simulations are compared with those using different models, with different assumptions pertaining to the behavior of internal energy exchange. The aforementioned set of four simulations is performed using two other physical models that assume thermal equilibrium and can be described with one temperature

only, the thermally perfect gas model (TPG) and the calorically perfect ideal gas (PIG) model. A brief description of the mathematical formulation and underlying assumptions is given below.

5.3.1 Thermal equilibrium models

The system of equations implemented for the calorically perfect ideal gas and for the thermally perfect gas models follows the widely known classical Navier-Stokes approach for a continuum, viscous laminar, chemically frozen flow in thermal equilibrium, with a single equation for the energy (total energy of the mixture) and assuming a single temperature T. In both models, the specific heats are defined as:

$$C_p = \frac{\gamma R}{\gamma - 1}, \qquad C_v = C_p - R \tag{5.1}$$

where C_p is the specific heat of the mixture at constant pressure, C_v is the specific heat of the mixture at constant volume, $\gamma = \frac{C_p}{C_v}$ is the ratio of specific heats and R is the gas constant of the mixture. In the calorically perfect ideal gas model, there is no physical modelling of the internal structure of molecules in the gas. It is considered that rotational/vibrational/electronic degrees of freedom are not excited and therefore rotational/vibrational/electronic energy is not accounted for. Internal energy is only described in terms of translational degrees of freedom. The specific heats, and therefore the ratio of specific heats, remain constant with temperature. The thermally perfect gas model considers the impact of vibrational excitation assuming thermal equilibrium. As the internal energy of the gas increases, a portion of it is instantaneously transferred from the translational to the vibrational mode, instead of raising the temperature of the gas. This results in a decrease of the specific heat ratio with temperature $C_p = f(T)$ and $C_v = f(T)$ that depends on the mixture in question. The temperature at which this process becomes significant depends on the characteristic vibrational temperature of the molecules. As shown in Fig. 5.3, for the mixture studied in this work, this model predicts a significant decrease of the specific heat ratio up to 2000 K, above which this change becomes more gradual. The graph shows that the low characteristic vibrational temperature of CO_2 molecules has a large impact on the thermodynamic properties of the mixture even if thermal nonequilibrium is not considered, and therefore is it expected that this will influence the shock interaction structures of the flows studied in this thesis.

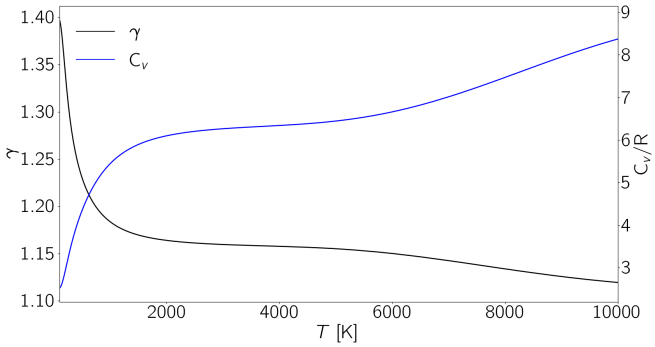

Figure 5.3: Variation of specific heat at constant volume C_v and specific heat ratio γ of a CO_2:0.97, N_2:0.03 mixture with temperature for a thermally perfect gas model.

5.3.2 Nonequilibrium shock interaction patterns

This section presents the study of nonequilibrium shock interaction structures with respect to the angle of the aft wedge. Numerical results are obtained on the basis of the two-temperature model introduced in Chapter 3. Figure 5.4 shows the numerical schlieren for the four different geometries at the left, as well as pattern schematics that identify the flow features observed and help better understand the interaction mechanisms, at the right. Figure 5.5 shows a comparison of the respective surface pressure (left) and heat flux (right) distributions. For the first aft wedge angle of 40°, a type VI Edney pattern occurs at point P, where the interaction of oblique shocks generates another oblique shock CS, a contact discontinuity CD and an expansion wave EW, that reflects on the surface on the aft wedge, refracting on CD and causing CS to turn downwards and becoming a curved shock. Upstream of point P, the system of waves depicted in Fig. 1.3a originates in the compression corner. Shocks DS and ReS intersect each other before interacting with the leading shock LS. However, this intersection occurs so close to the triple-point P that no other features are generated and the resulting pattern is basically equivalent to having all the three shocks interacting at point P, as illustrated in the schematic. The different flow features of this interaction pattern are also seen in the distribution of surface loads shown by the black curve in Fig. 5.5. An initial increase/decrease in pressure/heat flux occurs as consequence of flow separation on the surface of the first wedge. Downstream of this region, both distributions are qualitatively similar, exhibiting a relatively wide peak that corresponds to the region of flow compression and reattachment to the wall on the surface of the second wedge. This is followed by a gradual decrease of pressure and surface heating resulting from the reflection of

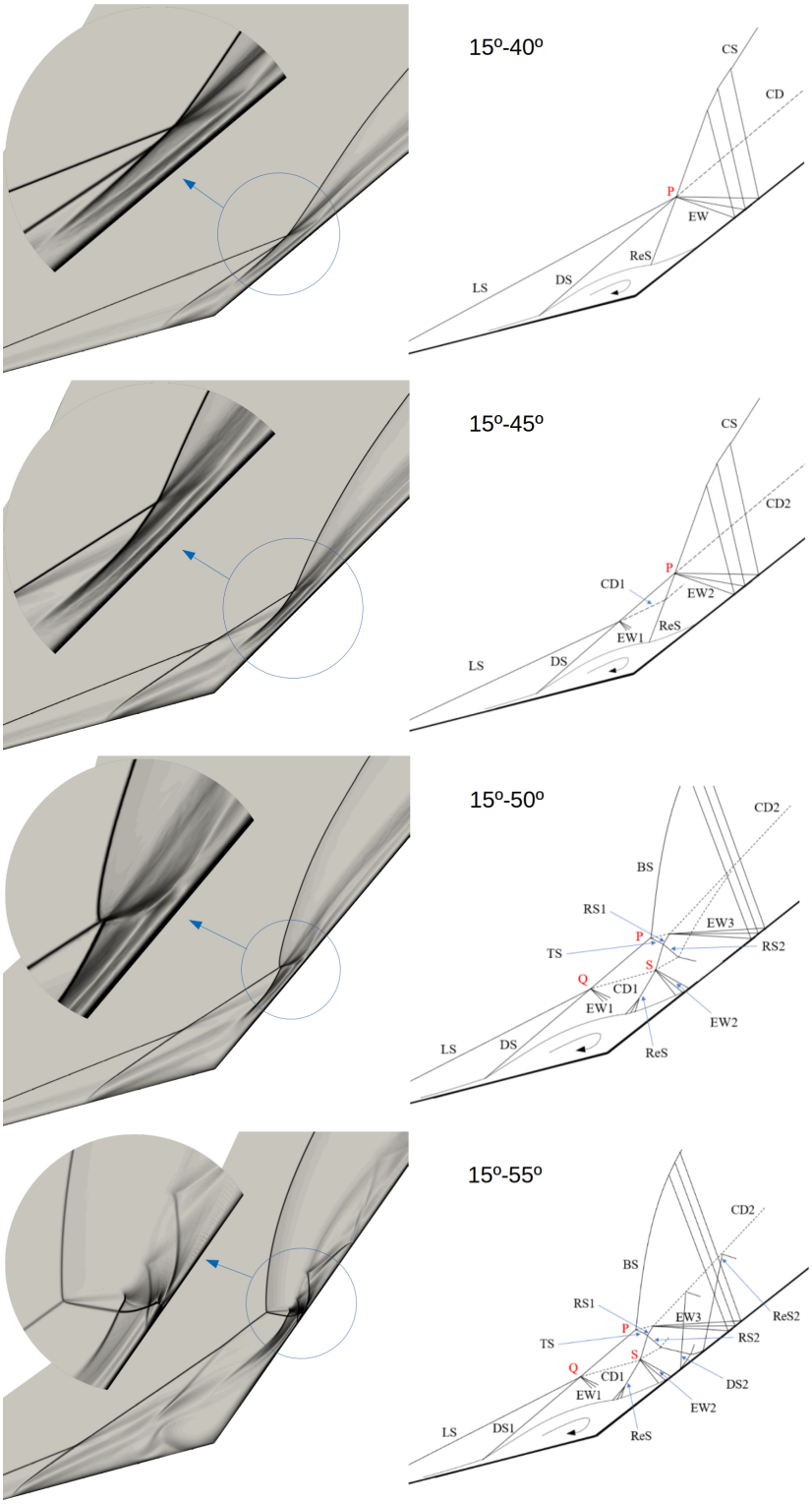

Figure 5.4: Numerical schlieren (left) and schematics (right) for shock interaction patterns obtained with a two-temperature model.

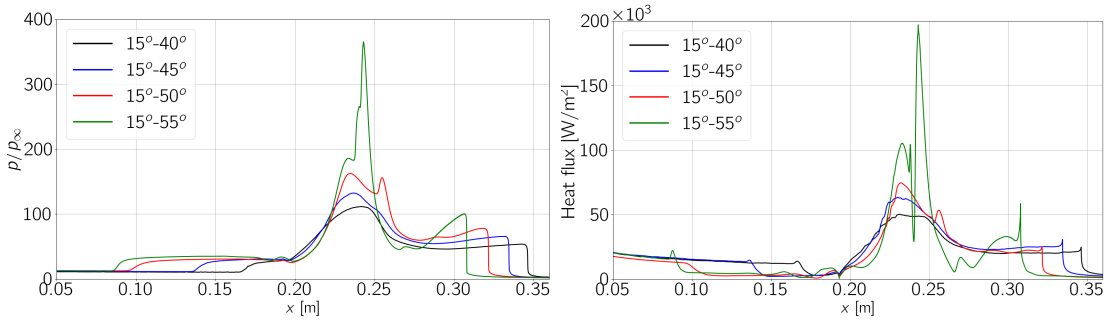

(a) (b)

Figure 5.5: Comparison of surface aerothermal loads obtained with a two-temperature model for the different double-wedge geometries: (a) normalized pressure distribution, (b) heat flux distribution.

the expansion wave EW on the wall.

Increasing the aft wedge angle to 45° leads to a few changes in the shock interaction pattern over the double-wedge. The system of waves in the compression remains the same, but a significantly larger recirculation region is obtained. In this case, the stronger detachment shock DS, characterized by a larger shock angle, intersects the leading shock LS much before reaching point P. This intersection locally generates a secondary type VI interaction pattern, exhibiting the typical expansion wave EW1 and contact discontinuity CD1 emanating from the intersection point. Downstream of this point, CD1 turns upward upon crossing the reattachment shock ReS. Furthermore, the combined shock resulting from the secondary type VI interaction intersects the reattachment shock ReS at the triple-point P, which generates the additional features CS, CD2 and EW2 that characterize the primary type VI interaction pattern. Since all the differences in the interaction pattern occur away from the wall, the distributions of surface quantities is qualitatively very similar to the previous geometry, as expected. A quantitative comparison confirms the observation already made for the size of the separated region. Indeed, we can see in Fig. 5.5 that for this geometry the flow separates at $x = 0.135$ m, whereas for the 40° aft angle the separation point is located at $x = 0.165$ m. The higher aft wedge angle leads to an overall stronger shock interaction structure, with a peak of pressure and heat flux resulting from the reattachment of the boundary layer that is, respectively, 16% and 21% larger for this case.

For the 15°-50° geometry, the boundary layer separates closer to the leading edge and the size of the recirculation bubble further enlarges. In the vicinity of the compression corner, a system

of waves equivalent to the one found for the previous test-case is obtained, with a local type VI interaction originating at point Q as a result of the intersection between the leading shock LS and the detachment shock DS. Further downstream, the boundary layer gradually reattaches accompanied by a series of compression waves that merge, forming the reattachment shock ReS. The flow pattern generated in the vicinity of the second wedge corresponds to a type V with a regular reflection configuration, which significantly differs from the ones observed up to this point. Shock QP resulting from the type VI interaction and the bow shock BS interact at the triple-point P, from which a transmitted shock TS emanates. The latter intersects with shock ReS in a regular refection that gives rise to the reflected shocks RS1 and RS2. Shock RS1 reflects on the contact discontinuity CD2 - arising from the shock interaction at point P - and an expansion fan EW3 forms, accelerating the flow. Upon this reflection, CD2 changes its direction because of the increased pressure behind the shock wave, and a convex corner forms. Further downstream, EW3 reflects on the surface of the second wedge and crosses CD2. The contact discontinuity CD1 generated in the type VI interaction plays an active role in the mechanism of the type V interaction. After crossing the reattachment shock ReS, turning it upward and generating another expansion wave EW2, it intersects shock RS2. From this latter interaction, CD1 changes its direction and ends up merging with CD2. The relatively weak shock RS2 further loses its strength when crossed by CD1 and the SWBLI of shock RS2 on the surface of the second wedge is weak, never causing the boundary layer to separate. The increased complexity of the flow pattern obtained for this geometry is also reflected on a qualitatively different behaviour of the surface pressure and heat flux distribution. For this case, after the first peak caused by reattachment of the boundary layer, both pressure and heat flux drop as a consequence of the expansion wave EW2 that reaches the surface of the second wedge. A second peak, 12% and 23% lower in pressure and heat flux respectively, is observed just after, resulting from the weak impingement of shock RS2 on the surface.

As the aft wedge angle is further increased to 55°, the trend previously observed for the location of the separation point and size of the corresponding recirculation bubble holds. This trend can be easily seen in Fig. 5.5a, shown by the location of first increase in pressure, corresponding to the detachment shock. Overall, the shock interaction mechanism obtained for this test-case is similar to the one obtained for 50°. The increased angle of the detachment shock DS and

standoff distance of the bow shock BS leads to a stronger shock TS emanating from the triple-point P. The main differences in the flow pattern arise from the higher angle of shock RS2. The impingement of the latter shock on the surface of the second wedge leads to a stronger SWBLI, that in this case results in localized boundary layer separation. Similarly to what occurs in the compression corner, this separation is accompanied by an additional detachment shock DS2 and reattachment shock ReS2 that increase the complexity of the wave system. Both of these shocks end up reflecting on the contact discontinuity CD2 in a regular manner. In Fig. 5.5a, the several stages of flow compression are shown, corresponding to detachment and reattachment of the boundary layer in the compression corner, followed by detachment and reattachment of the boundary layer in the region of shock impingement. These four successive shocks cause the surface pressure to rise much above the previous cases, with a peak that is 54% larger than the one for the 15°-50° geometry. The larger separation region in the compression corner contains some vortex dynamics that can be seen in the heat flux surface distribution. This dynamics is seen in Fig. 5.5b between $x = 0.15$ m and the compression corner at $x = 0.193$ m, where some fluctuations of the surface heating occur. Downstream of the compression corner, the heat flux gradually rises as a consequence of the reattaching boundary layer, generating a relatively wide peak at $x = 0.233$ m. The following narrow peak occurs as a result of the detachment shock DS2, followed by a drastic drop corresponding to the boundary layer separation induced by impingement of shock RS2. Upon reattachment, accompanied by shock ReS2, the boundary layer becomes extremely thin and the pressure is high, leading to very localized strong surface heating of about 197,000 W/m^2, 61% higher than the maximum obtained for the 50° aft wedge angle.

5.3.3 Thermal nonequilibrium effects

The presence of nonequilibrium phenomena is explicitly discussed in this section. The maximum flow temperature of 2621 K was observed for the highest aft angle of 55° as expected, just behind the strongest portion of the bow shock. No changes of mass fraction were seen for any of the cases, indicating that there was no dissociation being activated. Since for the geometries and conditions studied the flow is chemically frozen, the focus is exclusively on the effects of vibrational excitation. Figure 5.6 shows a measure of the degree of thermal nonequilibrium

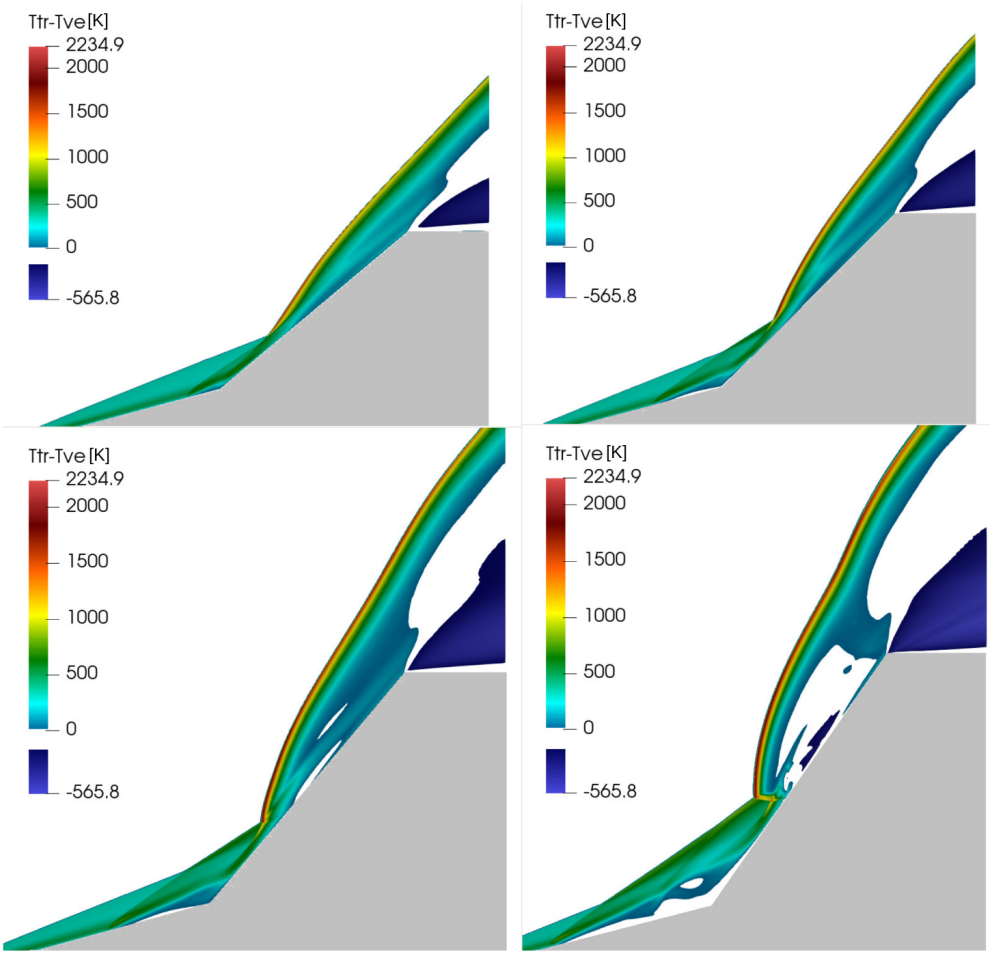

Figure 5.6: Degree of thermal nonequilibrium obtained for all geometries: 15°-40°, 15°-45°, 15°-50° and 15°-55° double-wedge.

in the flow (difference between trans-rotational and vibro-electronic temperatures) obtained for all geometries. It is evident that for all different aft angles, the state of thermal equilibrium of the freestream is not preserved after the shocks. Right behind the leading shock LS, the vibrational temperature starts to rise, but remains below the translational temperature due to the vibrational relaxation time that it takes to equilibrate the two internal modes of energy. Regions of stronger nonequilibrium take place behind the strongest portion of the bow shock, since these are the regions where a larger amount of kinetic energy is transformed into internal energy. As the aft angle increases, the bow shock is stronger and so is the thermal nonequilibrium in this region. However, larger regions of thermal equilibrium are seen also as the angle increases. This is because post-shock velocities are lower for stronger shocks, therefore the flow residence time increases and becomes much larger than vibrational relaxation time. This same reasoning would explain why the conclusions of this thesis differ from the one drawn by Candler [56], who observed a very small region with thermal nonequilibrium in their results. The degree of nonequilibrium established in supersonic/hypersonic flows may vary substantially from case to case, depending on the different parameters. The different geometrical shape used by Candler (cylinder) and larger freestream Mach number studied in his work result in a much stronger bow shock, associated to much larger post-shock translational temperatures (in the order of 10^4). Following the reasoning above, it is expected that, in that case, equilibration of internal energies is achieved much faster and therefore a smaller region of the flowfield is thermal nonequilibrium.

Furthermore, thermal equilibrium tends to be reached in other regions of low velocity such as separated regions, either in the recirculation bubble in the vicinity of the compression corner - except for the lowest angle where this bubble is too small - or regions of separation due to shock impingement on the surface of the second wedge. On the other hand, downstream of the expansion corner, the vibrational temperature becomes higher than the translational one. This is a state of population inversion in the vibrational levels, where the upper states are more populated than the lower ones. The rapid expansion causes the translational energy to suddenly decrease below the vibrational one, which is a state of thermal nonequilibrium that is opposite of what occurs behind a shock wave. It is evident for all test cases that vibrational degrees of freedom are excited for the given flow conditions, and that are not in equilibrium with the

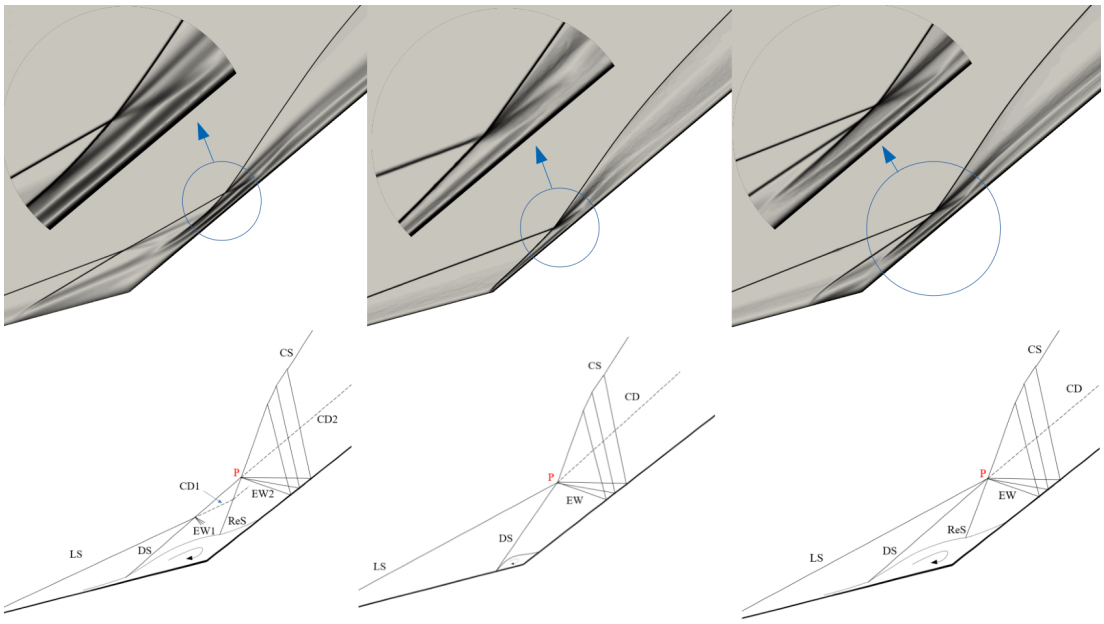

Figure 5.7: Comparison of density gradients and shock interaction schematics obtained for a CO_2-N_2 flow over the 15°-40° double-wedge: perfect ideal gas (left), thermally perfect gas (middle) and nonequilibrium gas (right).

translational energy.

5.3.4 Thermal equilibrium shock interaction patterns

In order to assess the role of thermal nonequilibrium on the physics of shock interactions obtained with the two-temperature model, the same test-cases have been simulated with the simplified models previosuly introduced . The aim is to assess the differences of shock interaction structures numerically obtained with the equilibrium models in relation to the more detailed two-temperature model. Both qualitative and quantitative comparisons are reported to understand the impact of different simplifying assumptions on the characteristics of the flow in terms of interaction patterns as well as surface pressure and wall heat flux distribution, respectively.

15°-40° double-wedge

Figure 5.7 shows the numerical results obtained for density gradient in the case of the 15°-40° geometry, as well as corresponding auxiliary schematics of the shock interaction pattern. A type VI Edney pattern occurs at point P for all three models. However, upstream of point P, all

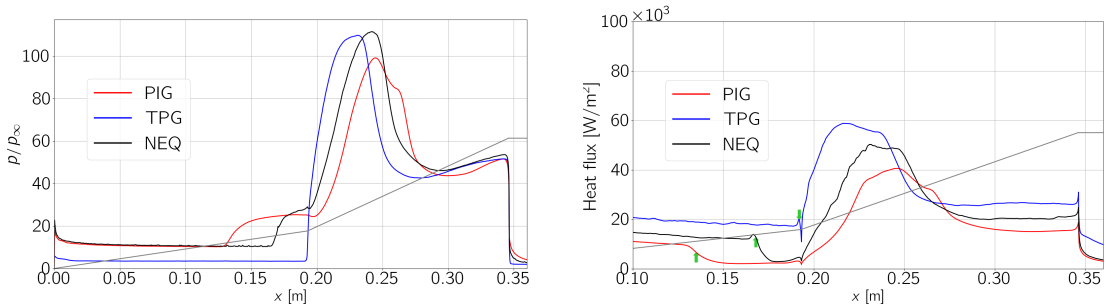

(a) (b)

Figure 5.8: Comparison of surface aerothermal loads of (a) normalized pressure and (b) heat flux, for the 15°-40° double-wedge: perfect ideal gas, thermally perfect gas and nonequilibrium gas model. Green arrows indicate separation points.

models result in different shocks structures originating at the compression corner. Both the PIG and NEQ models exhibit the system of waves depicted in Fig. 1.3a, where the major difference arises from the different locations of the detachment shock DS. In the case of the PIG model, a larger separation region leads to a shock DS that crosses the leading shock LS before reaching point P, leading to a secondary type VI pattern associated to the contact discontinuity CD1 and expansion wave EW1. EW1 impinges on the slip layer surrounding the separation bubble and CD1 refracts on the shock wave arising from the reattachment of the boundary layer, RS. For the PIG model, the primary type VI pattern is a result of interference between ReS and the curved shock generated in the secondary type VI interaction. On the other hand, for the NEQ model, the earlier separation point keeps the detachment shock DS under the leading shock. In this case, the type VI interaction is a consequence of interference between the leading shock LS and the shock resulting from coalescence of the detachment and reattachment shocks, DS an ReS respectively. The simplest shock interaction structure is observed when a TPG model is used. In this case, the boundary layer separates very slightly (the separation is too small to be visualized in the density gradient plots) and no reattachment shock is generated. The interaction pattern observed in this case is purely due to the interaction between shocks LS and DS. It is fair to conclude that the differences between the obtained shock interaction patterns originate from the different sizes of the recirculation bubble in the compression corner. For the PIG model, the internal energy of the gas - that is increased through a shock wave, as a result of the conversion of kinetic energy in the form of flow velocity to internal energy in the form of temperature and

pressure - is stored only in the translational degrees of freedom, causing a stronger disturbance of the flow associated to a larger separation, than for a case where vibration excitation is accounted for. The TPG and the NEQ model, on the contrary, account for the partition of internal energy between different internal energy modes, therefore resulting in lower post-shock temperatures and increased densities associated to a smaller recirculation bubble. The detailed NEQ model explicitly models this relaxation process by accounting for the time that it takes for the energy transfer to reach a state of equilibrium. Right behind the shock wave, vibrational levels are not populated instantaneously, which means that the portion of kinetic energy of the flow that is transformed into internal energy across the shock is stored only in the trans-rotational degrees of freedom at first, and then gradually transferred to the vibro-electronic modes. In the TPG model, the influence of vibration is modelled in a simplistic way, where the same portion of energy is redistributed instantaneously amongst the trans-rotational and vibro-electronic modes. As a consequence, the effect of energy absoption by vibrational excitation is further enhanced and almost no separation occurs. For the flow to deflect in the same direction, weaker disturbances are obtained when more energy is absorbed by the vibrational modes.

Figure 5.8 shows the normalized pressure and wall heat flux for the surface of the 15°-40° double-wedge. Despite the different interaction pattern obtained for the three models, the profile of both surface quantities is qualitatively similar. The LS post-shock pressure is almost identical for the PIG and NEQ model, higher than for the case of the TPG model, that exhibits a more attached shock in the nose. The first increase in pressure corresponds to the separation of the boundary layer, that occurs earlier for the PIG model at $x = 0.135$ m, then for the NEQ model at $x = 0.168$ m and nearly at the compression corner at $x = 0.192$ m for the TPG model. The precise locations of the separation point for each model are depicted in Fig. 5.8, indicated by the green arrows. The larger values of pressure, corresponding to the peaks, occur in the reattachment region for all models. It is interesting to notice that, despite the overall tendency for a more complex interaction in the case of the PIG model, the more gradual reattachment of the recirculation bubble leads to a wider and 12% lower pressure peak for this model, whereas for the NEQ and TPG they are almost identical in the maximum value, with a delayed location for the NEQ model, as expected from the larger size of the separated region. The different sizes of the recirculation bubble can also be clearly seen in Fig. 5.8, in the regions where the wall

heat flux is the lowest for each case. From the blue line, it is now evident that an extremely small separation exists in the compression corner of the TPG model, shown by the spike of minimum heat flux at about $x = 0.19$ m. The smoother separation obtained in the PIG solution is accompanied by a separation shock of a smaller angle than for the TPG and NEQ models, for which separation of the boundary layer is more abrupt. As such, the stronger separation shocks of the latter models locally compress the flow against the wall, leading to small spikes of the heat flux in these regions. As the boundary layer reattaches, a region of high local aerodynamic heating occurs. In the case of the TPG model, the separation region is quite small and reattachment occurs abruptly. This results in a larger heat flux peak, of about 17% higher than for the NEQ model and 44% higher than for the PIG model, where reattachment takes place gradually. The monotonic behaviour observed for the peaks of heat flux, in terms of having a larger peak for the TPG model, then the NEQ model and the PIG model, follows the thickness of the thermal boundary layer obtained in each solution. When vibrational excitation is not accounted for (PIG model), a thicker boundary layer is obtained due to the larger shock angles and lower post-shock velocities, compared to the vibrational nonequilibrium solution (NEQ model). In turn, the NEQ post-shock velocity is lower than the one obtained for the equilibrium solution (TPG model), for which the partition of internal energy between the two degrees of freedom is modelled to occur instantaneously. Apart from the higher heat flux peak obtained for the TPG model relative to the NEQ model, the locations and values of the heat flux peaks in the reattachment region follow the tendency observed in the pressure plots. For all three solutions, the expansion fan that forms at the ending point of the second wedge causes a sudden drop in surface pressure and heat flux.

15°-45° double-wedge

Figure 5.9 shows density gradient contours for the 15°-45° geometry and the schematics corresponding to the obtained shock patterns. As opposed to the NEQ model, for the PIG and TPG models the increment of 5° in the aft wedge angle is not sufficient to change the interaction pattern that was observed in the case of the 15°-40° double-wedge. The system of waves remains identical, with the differences lying in the size of the recirculation region, the shock angles and the curvature of the bow shock CS. For the PIG case, the separation point occurs closer to the

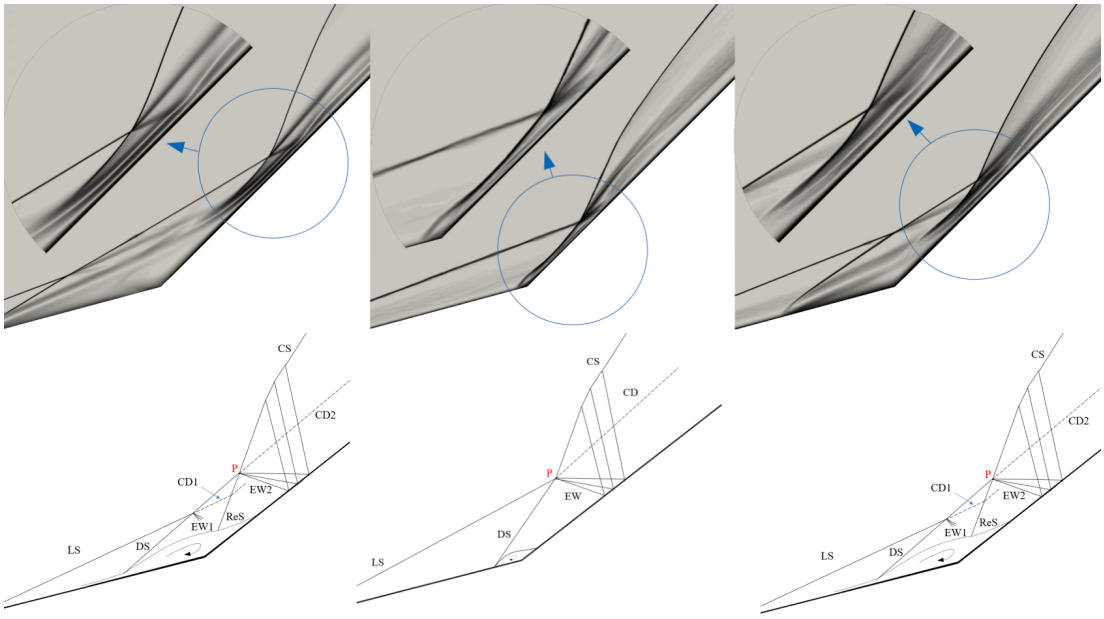

Figure 5.9: Comparison of density gradients and shock interaction schematics obtained for a CO_2-N_2 flow over the 15°-45° double-wedge: perfect ideal gas (left), thermally perfect gas (middle) and nonequilibrium gas (right).

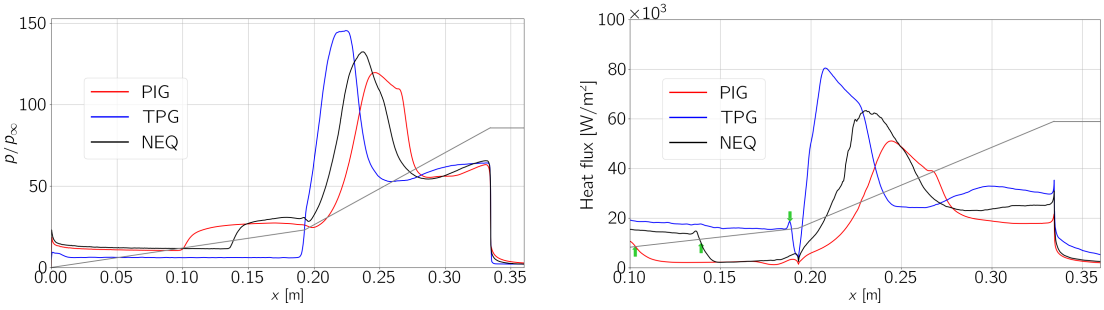

(a) (b)

Figure 5.10: Comparison of surface aerothermal loads of (a) normalized pressure and (b) heat flux, for the 15°-45° double-wedge: perfect ideal gas, thermally perfect gas and nonequilibrium gas model. Green arrows indicate separation points.

leading edge for the 15-°-45° than for the 15°-40° geometry, at $x = 0.10$ m vs. $x = 0.13$ m respectively, which results in a significantly larger separated region and larger angle for the detachment shock DS. Additionally, the 45° aft wedge angle leads to a reattachment shock RS and an interaction region that is further from the wall and in a more downstream location. The bow shock CS follows this tendency as well, being slightly more curved and significantly more detached from the surface of the second wedge. When it comes to the TPG model, the increment in the wedge angle also influences the separation region in the compression corner. For this geometry, a small detachment of the boundary layer can already be visualized. Even though a reattachment shock does not form, a small compression wave occurs in this location and turns the detachment shock DS downward, making it more attached to the wall. Contrary to what is observed for the PIG model, this causes the interaction region to shift upstream, even though the CS shock layer is slightly larger. It is relevant to note that, for the PIG model, the angle of the aft wedge is the only parameter that changes from test-case to test-case, which means that all the differences in the flowfield are solely attributed to this factor. For the TPG and NEQ solutions, the thermodynamic properties of the mixture also play a role. The fact that vibrational excitation absorbs the translational energy of the flow, reducing the post-shock temperatures and increasing density, leads to smaller shock standoff distances and overall weaker shock interactions. Accordingly, in the TPG solution, where the impact of energy absorption by vibration is expected to be more significant, the shock interaction pattern changes the least. In the case of the NEQ model, where the influence of vibrational excitation is expected to be smaller than for the equilibrium solution due to the associated time of relaxation towards equilibrium, the shock interaction pattern actually changes when the angle is increased, suggesting that the change in geometry has a larger impact on the flow physics than the real gas effects. This is also seen in Fig. 5.6, which shows that the degree of thermal nonequilibrium does not seem to be very different between the first two angles. The significantly larger separation length and the stronger detachment shock associated to a larger angle result in the local secondary type VI interaction found in PIG solution for both 15°-40° and 15°-45° double-wedges.

Figure 5.10 shows the surface quantities obtained for the 15°-45° double-wedge. The surface pressure profiles are qualitatively similar to the ones obtained for the 15°-40° double-wedge, except for the fact that, in this case, the TPG model results in a 12% larger maximum value

than the one of the NEQ model. Additionally, the separated region is now evident for the TPG model, shown by the first spike resulting from the detachment shock DS and followed by a sudden drop due to the small separated region. As expected from the increase in angle of the aft wedge and its effects on the strength of the shocks, the separation lengths as well as pressure peaks are larger for all models. The same observations hold for the heat flux plots. The monotonic tendency observed in the peaks of both pressure and heat flux (TPG →NEQ →PIG models) follows the behaviour of the reattachment of the boundary layer. When more internal energy is stored in the translational energy mode of the molecules in the gas, larger recirculation regions are obtained. Larger recirculation regions are followed by a more gradual compression that reattaches the flow to the wall, therefore resulting in lower and wider peaks for the surface quantities. The impact of a slightly larger separated region for the TPG model in relation to the previous geometry is noticeable from the overshoot occurring around $x = 0.19$ m, which corresponds to the detachment shock DS. The very short separated region in the compression corner results in undershoot right downstream.

15°-50° double-wedge

Figure 5.11 shows the same set of numerical results for the 15°-50° geometry. It is evident that for all the three models, completely different shock interactions patterns are obtained by incrementing 5° in the aft wedge angle. All the three shock interaction mechanisms exhibit instead a type V pattern with a regular reflection configuration. The trend observed for previous aft angles when it comes to the different ways of modelling the behaviour of vibrational relaxation is maintained: when more internal energy is absorbed in the excitation of vibrational modes, the sizes of the recirculation bubble and separation length are smaller and the overall interaction pattern is less complex (PIG →NEQ →TPG). Comparing to the previous geometries, stronger SWBLI occurs, as there is shock impingement on the wall of the second wedge. As opposed to the NEQ solution, the boundary layer obtained with the PIG model separates very close to the leading edge (see separation point in Fig. 5.12b), creating a very large separation bubble inside which vortex dynamics occurs. The type VI interaction resulting from the intersection between shocks LS and DS is also seen in the PIG solution but for this case it occurs in the vicinity of the leading edge. The contact discontinuity CD1 ends up being dissipated in the

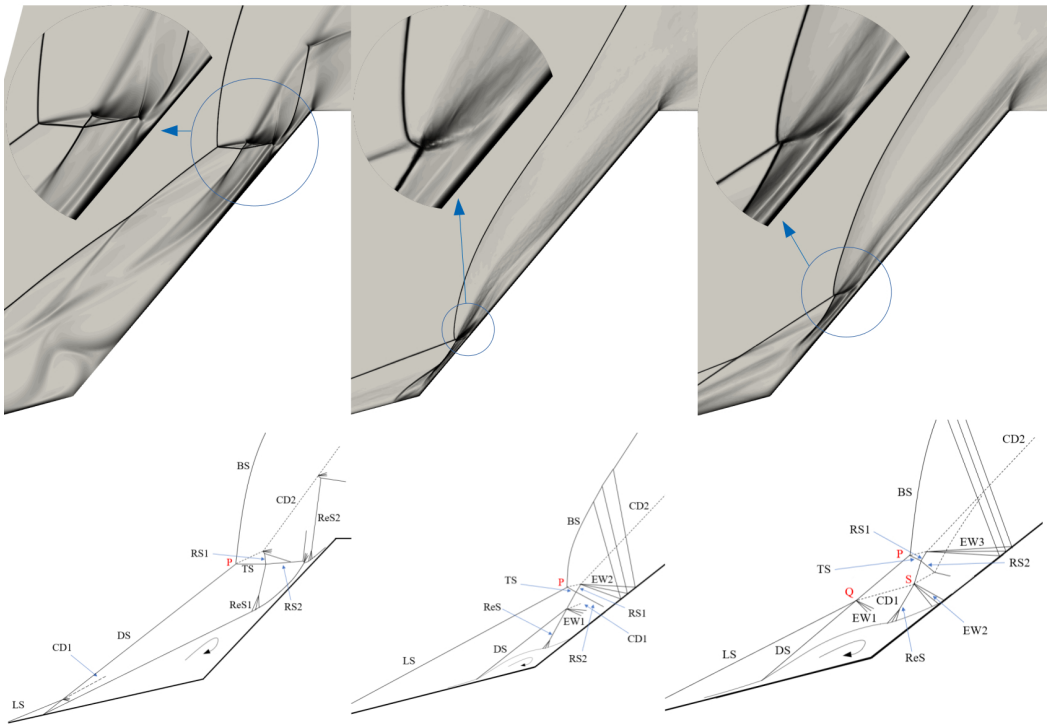

Figure 5.11: Comparison of density gradients and shock interaction schematics obtained for a CO_2-N_2 flow over the 15°-50° double-wedge: perfect ideal gas (left), thermally perfect gas (middle) and nonequilibrium gas (right).

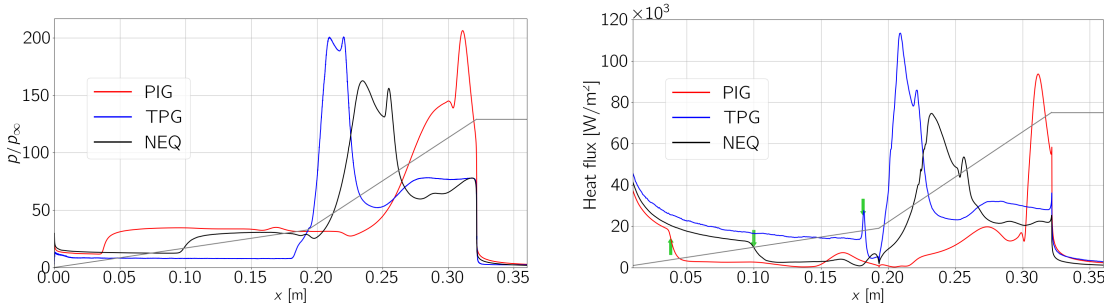

(a) (b)

Figure 5.12: Comparison of surface aerothermal loads of (a) normalized pressure and (b) heat flux, for the 15°-50° double-wedge: perfect ideal gas, thermally perfect gas and nonequilibrium gas model. Green arrows indicate separation points.

interaction with the separated viscous layer and the vortexes generated inside the recirculation bubble, never reaching the region where the main interaction takes place. Shocks TS and ReS1 interact in a regular reflection that gives rise to a system waves similar to the one seen in the NEQ solution. However, for the PIG model RS1 impinges on the contact discontinuity CD2 in a lambda-shaped stem reflection, resulting in a small expansion and an additional shock that impinges on RS2. Whereas for the NEQ case shock RS2 impinged on the surface of the second wedge in a relatively weak manner, here the adverse pressure gradient leads to a clear SWBLI. Shock RS2 causes the boundary layer to locally separate and reflects in a Mach stem inverted lambda-shaped pattern. Downstream of the normal shock impinging on the wall, the reattachment of the boundary layer is accompanied by a series of compression waves that merge into the reattachment shock ReS2, which in turn reflects on the contact discontinuity CD2 in another Mach reflection structure. Compared to the NEQ results, the TPG solution is characterized by a much smaller separated region, as well as a significantly weaker detachment shock DS that never crosses the leading shock LS. Accordingly, a local type VI interaction occurs between DS and ReS and point P marks, instead, the interaction between the leading shock LS, the transmitted shock TS and the bow shock BS. The resulting contact discontinuity CD1 refracts on shock RS2, that impinges on the wall of the aft wedge without separating the boundary layer.

Figure 5.12 shows the surface aerothermal loads for the 15°-50° double-wedge. As expected from interaction patterns discussed above, the PIG solution results in a wall normalized pressure and heat flux distribution that are qualitatively very different from the ones obtained for the models that account for vibrational excitation. After the plateau region of pressure in the separated region, a gradual increase translates the smooth reattachment of the boundary layer. Once the boundary layer is reattached, a strong peak of pressure emerges due to the impingement of shock RS2 on the surface of the aft wedge. It is noticeable that, for this case, the main shock interaction mechanism occurs very close to the expansion corner. On the other hand, the TPG and NEQ models results in surface distributions that are qualitatively very similar. Downstream of the separated region, that is much smaller for the TPG solution, both curves display two peaks of pressure, respectively due to the reattachment of the boundary layer and impingement of shock RS2. In the NEQ solution, the flow expands downstream of boundary layer reattachment, resulting in a impingement peak of pressure that is about 12% lower than

the one caused by reattachment. For the TPG model, reattachment and shock impingement occur close together, therefore the flow does not expand significantly before compressing again and the two peaks have a very similar intensity of about 200. For both models, after the strong expansion downstream of the second peak, the movement of the contact discontinuity towards the wall slightly recompresses the fluid before reaching the convex expansion corner. As observed for the previous geometry, the smaller recirculation bubble of the TPG solution leads to a higher and thinner peak of pressure, revealing a stronger recompression in the reattachment region, as opposed to the NEQ solution, for which a gradual reattachment results in a lower and wider peak. The heat flux distribution of the TPG and NEQ models fairly follow what is seen in the pressure plot, except for the second heat flux peak of the TPG model that is 25% lower than the first one. This is due to the fact that shock RS2 crosses the thermal boundary layer and further weakens, which would affect the heat flux but not pressure. When it comes to the PIG model, downstream of the separation point and up to about $x = 0.26$ m, the region of separation exhibits fluctuations of heat flux that take place as a consequence of the vortexes that result from flow recirculation. Occurrence of vorticity beneath the separation line due to increasing aft angle has been reported before [2, 90]. Between $x = 0.25$ m and $x = 0.29$ m, a wide and low local peak occurs as a result of the smooth reattachment of the boundary layer. At $x = 0.29$ m the heat flux slightly decreases again due to shock induced separation. The boundary layer reattachment following the impingement of shock RS2 then leads to a very localized peak of heat flux at about $x = 0.31$ m, before the strong expansion occurring due to the convex corner.

15°-55° double-wedge

As opposed to the NEQ model, the flow over the 15°-55° geometry using a PIG model did not reach steady state, therefore the solution obtained with the steady state solver was provided as first guess to resolve the unsteady shock interaction process with time-accurate simulations. Figure 5.13 shows density gradient contours and shock pattern schematics for the different shock interaction structures that were obtained. The complexity of this test-case deserves a thorough description of the unsteady dynamics driving the mechanism of interaction. The flow physics became periodic after 0.015 s, therefore the first and last snapshots show the same flowfield. The periodicity of the flow physics becomes evident in Fig. 5.14, that shows instant normalized

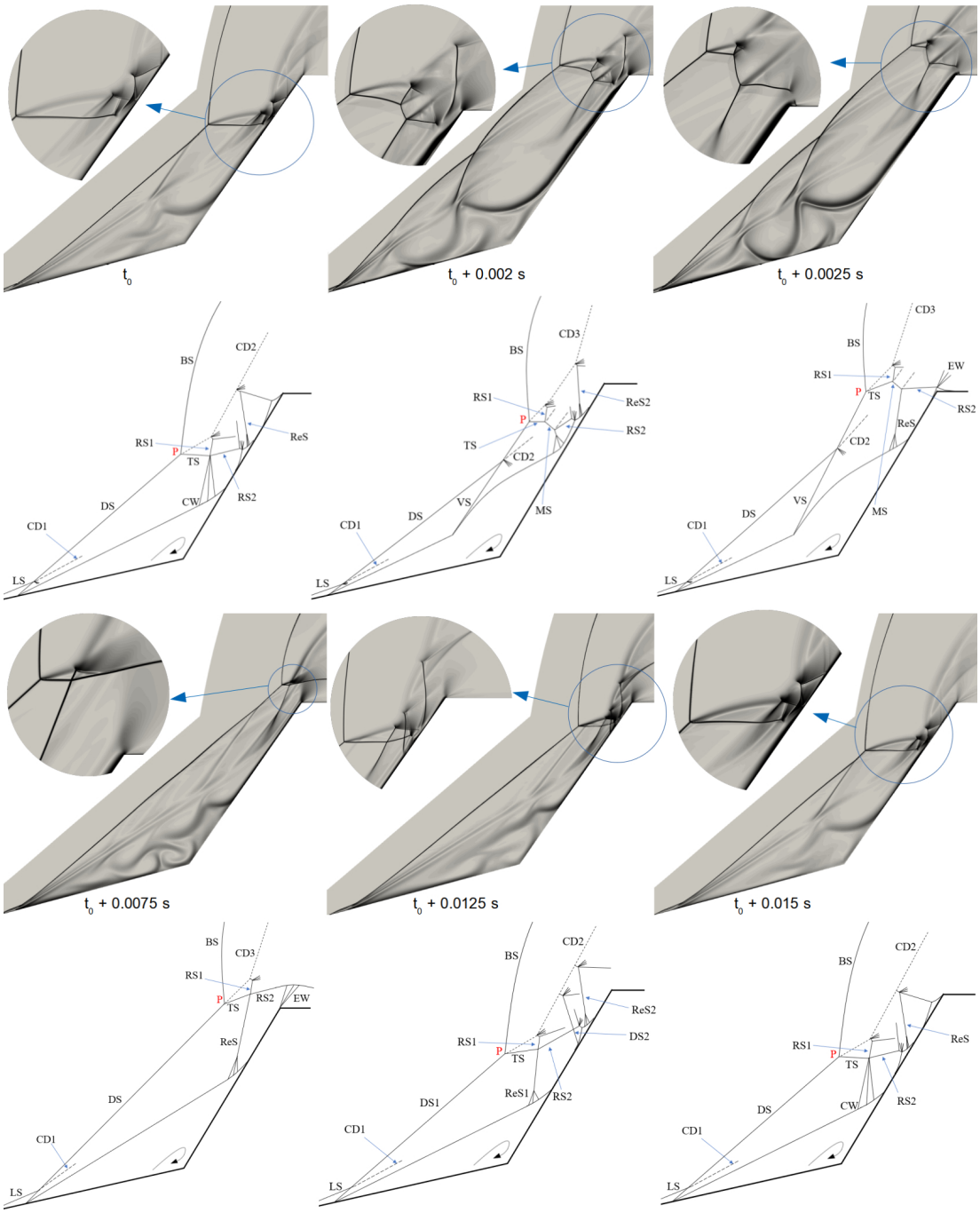

Figure 5.13: Unsteady density gradients and shock interaction schematics obtained for a CO_2-N_2 flow over the 15°-55° double-wedge with a perfect ideal gas model.

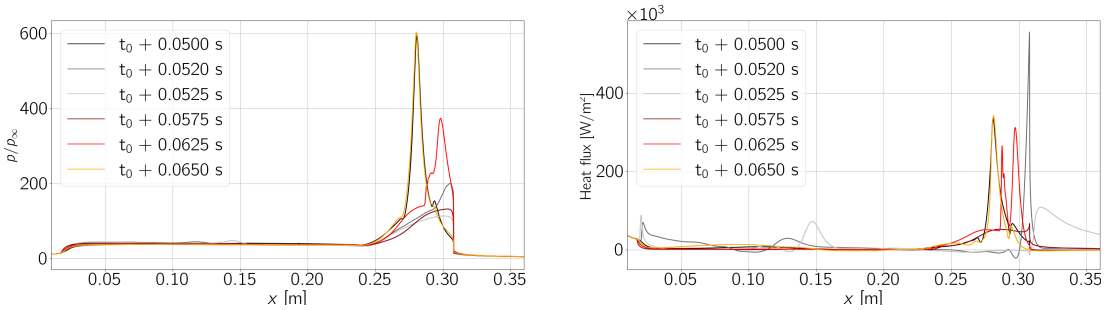

(a) (b)

Figure 5.14: Instant surface aerothermal loads for the 15°-55° double-wedge with a perfect ideal gas model: (a) normalized pressure distribution, (b) heat flux distribution.

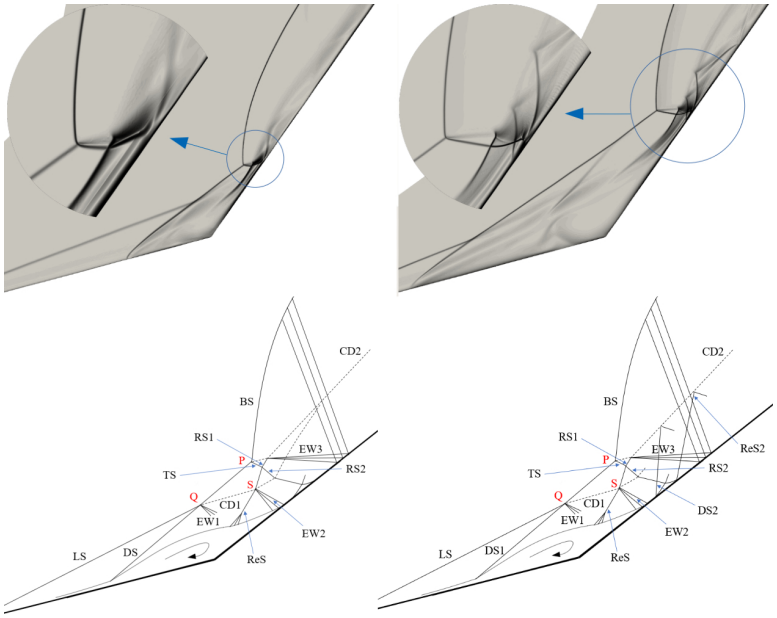

Figure 5.15: Comparison of density gradients and shock interaction schematics obtained for a CO_2-N_2 flow over the 15°-55° double-wedge: thermally perfect gas (left) and nonequilibrium gas (right).

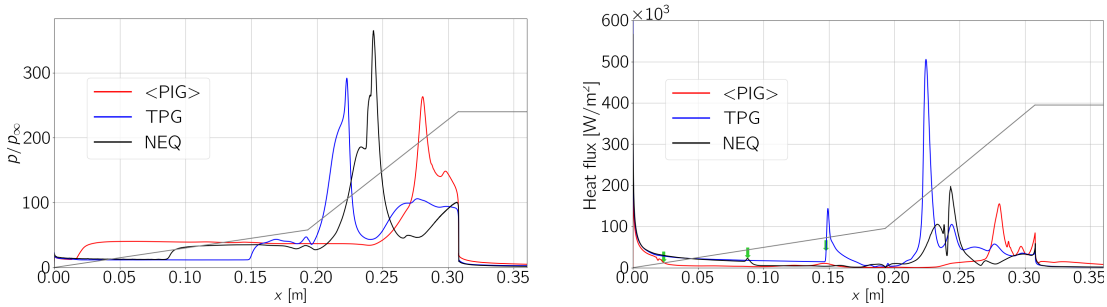

(a) (b)

Figure 5.16: Comparison of surface aerothermal loads of (a) normalized pressure and (b) heat flux, for the 15°-55° double-wedge: perfect ideal gas (time averaged), thermally perfect gas and nonequilibrium gas model. Green arrows indicate separation points.

pressure and heat flux distributions for this test-case. The initial and final curves, respectively at t_0 and $t_0 + 0.015$ s, are almost identical. Even though the heat flux profiles at these instants of time do not match with a perfect superimposition, the shock interference pattern does not change and the exact same type of interaction is obtained.

At the initial instant of time t_0, the detachment shock DS interacts with the bow shock BS generated by the second wedge, forming a triple point P with a transmitted shock TS directed towards the aft wedge. A second triple-point is formed as the reattachment compression wave CW interacts with the transmitted shock TS. The shock interaction mechanism is quite similar to the one obtained for the 15°-50° with a PIG model. The first difference lies in the fact that the compression wave CW generated in the reattachment of the boundary layer downstream of the compression corner does not form a shock wave before interacting with the transmitted shock TS, but this does not seem to affect the overall type V interaction. Furthermore, when shock ReS reflects on the contact discontinuity CD2, in this case it impinges on the surface of the aft wedge, resulting in a third region of boundary layer separation and a spike in surface pressure and heating, at $x = 0.275$ m. The impingement of shock RS2 on the wall plays a major role on the unsteady mechanism of interaction. The shock-induced adverse pressure gradient is transmitted upstream through the subsonic portion of the boundary layer, affecting the overall shock system that becomes more complex at $t_0 + 0.002$ s. The propagation deforms the shear layer and significantly increases the size of the separation bubble in the compression corner, shifting the interaction region downstream. As seen in Fig. 5.14, the surface pressure peak has con-

siderably decreased and is now located just upstream the expansion corner. On the other hand, the shock-induced separation leads to a minimum value of surface heating, just before a large spike due to reattachment of the boundary layer in this region. As the disturbances resulting from shock impingement travel upstream, vortex dynamics is generated/energized inside the large-scale flow separation. At this point, the largely separated recirculating flow in the compression corner causes the detachment shock DS to become curved and an additional curved shock wave VS to appear. Both shocks interact in a local type VI interaction. The vorticity-related fluctuations of surface pressure and heat flux seen in Fig. 5.14 are an indicator of the upstream disturbances created by shock impingement. Even though the separation point on the fore wedge is never altered throughout the unsteady process, and the upstream conditions of the detachment shock DS do not change during the time-periodic flow, the strength of the detachment shock DS changes due to the variation of the separation angle. Reattachment of the large separation region is accompanied by a series of compression waves CW that, at this instant of time, merge to form a shock wave before interacting with shock TS. In an interaction that is considerably stronger than for the previous instant of time, the reattachment shock and transmitted shock TS interact in a Mach reflection structure through the Mach stem MS. From the extreme points of this Mach stem, two additional contact discontinuities emanate. Similarly to what is observed in the previous snapshot, shock impingement of RS2 occurs further downstream on the surface of the second wedge. After impingement, RS2 is reflected on the surface on the aft wedge and then on CD2, at which point it becomes quite weak and ends up fading in the strong expansion of the convex corner.

At $t_0 + 0.0025$ s, the shock interaction mechanism has further shifted towards the expansion corner and maintains its structure. The flow inside the recirculation region becomes increasingly chaotic, and additional shocks VS are seen at the top of the recirculation flow region, each associated with a local type VI interaction. No shock impingement occurs at the wall of the second wedge, since RS2 only reaches the surface of the geometry downstream of the convex corner, where the strong expansion takes over. The disturbances generated by previous shock impingement start damping out and, as seen in the transition from $t_0 + 0.0025$ s to $t_0 + 0.0075$ s, decaying vortex activity causes shocks VS to vanish and the angle and standoff distance of shock DS to decrease. At $t_0 + 0.0075$ s, the detachment shock DS has returned to its initial

linear shape. As it strongly interacts with the bow shock BS, the latter also gets closer to the wall. The interaction weakens, the two triple-points connecting the Mach stem collide and a type V pattern with regular shock reflection is formed. At this instant of time, the reattachment shock ReS and the transmitted shock TS reflect on each other in a regular manner, giving rise to shocks RS1 and RS2. The latter becomes curved when it interacts with the corner expansion fan, never reaching the wall. Accordingly, for these two instants of time, both surface pressure and heat flux do not exhibit any peaks upstream of the expansion corner.

At t_0+0.0125 s, the motion of the interaction mechanism has changed its direction and is moving upstream, as it becomes again more complex. A type V regular reflection still dominates the flowfield, but additional shock waves are formed. As the shock interaction structure approaches its initial shape, some features are still different from the state of the flow at the start of the period. The reattachment region still exhibits a clear merging of the compression waves into a single shock ReS1, seen in Fig. 5.14a as the increase in pressure after the separation plateau. The following increase in surface pressure corresponds to the strong SWBLI that results in a large shock-induced boundary layer separation. The size of the shock-induced separation is dictated by the impingement angle and strength of the transmitted shock. The thickening of the boundary layer at this location further displaces the bow shock BS upstream along with the triple-point P. As a consequence of the larger separation, a detachment shock DS2, that is not seen at the first instant of time, appears upstream of the impingement location. In Fig. 5.14b, this separation corresponds to the sudden drop in surface heating, located in between the two spikes generated at reattachment locations, ReS1 and ReS2. The reattachment shock ReS2 is also seen in the pressure plot as the peak of the red curve. The multiple shocks reflect on the contact discontinuity and the wedge surface, intersecting each other regularly. Finally at $t_0 + 0.015$ s, the shock interaction structure has further moved upstream and its shape, as well as distribution of surface quantities, correspond to the ones obtained for the initial instant of time. The flow physics of this shock interaction mechanism can be summarized as a strong coupling between the separation angle, vortex dynamics in the separated region, the impingement of shock RS2 and overall shock interaction structures.

Figure 5.15 shows the numerical results obtained for the 15°-55° double-wedge with a TPG and NEQ model. Accounting for molecular vibrational motion seems to stabilize the entire

flow, since both of these solutions achieved steady state. Durna et al. [9] showed that, below a certain threshold value for the angle of the aft wedge, the flow reaches steady state after shock establishment time. Our results obtained for this geometry show that accounting for vibrational excitation delays this threshold. Given the trend observed in the parametric study, it is fair to assume that the equilibrium solution would lead to a later transition between a steady and an unsteady mechanism of interaction. In both cases, the increase in aft wedge angle in relation to the previous geometry leads to further displacement of the separation point towards the leading edge and a larger separation region (however still smaller than for the PIG solution). In the TPG solution, the pattern of interaction slightly changes in relation to the previous aft wedge angle. Shock DS has an angle that is large enough to cross the leading shock LS. The shock wave system is equivalent to the one observed for the 15°-50° with a NEQ model. However, now shock RS2 is strong enough to reflect on the surface of the second wedge, causing a small region of boundary layer separation. The interaction is overall stronger for the NEQ solution than for the TPG one. The increased angle of the detachment shock DS and standoff distance of the bow shock BS leads to a stronger shock TS emanating from the triple-point P, located further downstream than for the TPG model. This discrepancy also affects the intensities of the remaining shocks resulting from this interaction. The stronger reflection of RS2 on the surface of the second wedge leads to a stronger SWBLI with a larger region of boundary layer separation that is accompanied by a detachment shock DS2 and a reattachment shock ReS2, that are not seen in the TPG solution.

Figure 5.16 shows a comparison of the surface quantities between the three models, where for the unsteady case a time-averaged distribution over the periodic cycle is plotted. The TPG and NEQ models result in a qualitatively similar normalized pressure distribution. The first increase in pressure corresponding to the detachment of the boundary layer takes place in different locations for the three models, occurring at $x = 0.021$ m when vibrational excitation is not accounted for, at $x = 0.088$ m when the nonequilibrium relaxation time is accounted for and more downstream, at $x = 0.148$ m when equilibrium is enforced. The pressure plateau downstream of the separation point is similar for all three models, which shows that the effects of vibrational excitation in surface pressure are minimal in this region. For the models that account for molecular vibration, the second increase in pressure results from reattachment of the boundary layer,

which occurs more gradually for the NEQ model. The more abrupt reattachment in the TPG solution leads to a larger pressure gradient in this region, and just downstream to a 9% larger spike resulting from shock impingement. The time-averaged surface pressure obtained with the PIG model results in a pressure peak resulting from shock impingement that is of similar intensity as the one obtained with a NEQ model. As for the surface heating distributions, all three models result in qualitatively different curves. Whereas for the TPG model, a heat flux spike is generated in the region of boundary layer detachment on the surface of the fore wedge, this transition is smooth in the NEQ solution. In contrast, the transition between boundary layer reattachment and shock impingement is smoother for the TPG model, which results in a single large peak of heat flux of about 500,000 W/m^2 in this region. The NEQ solution, on the other hand, exhibits two smaller heat flux peaks that are separated by a sudden drop of this quantity, which is a consequence of the SWBLI separated region between reattachment and shock impingement. The PIG model results in a long region of low heat flux corresponding to the very large separation bubble. Several spikes are obtained in the surface time-averaged heat flux near the expansion corner, where most of the interaction features take place. It is worth noticing that, even though the averaged heat flux is overall much lower for this model than for the other two, from a design perspective it is essential to consider the instantaneous spike at $t_0 + 0.002$ s that results in the highest value of heat flux observed in the numerical results.

Table 5.5 summarises the shock interactions patterns obtained in study I of this chapter:

5.4 Effect of Mach number

As discussed in the literature review presented in Chapter 2, it is known that freestream conditions have a significant influence of patterns of shock interaction in the case of air mixtures. The numerical study performed in Chapter 4 revealed that, for the case of carbon-dioxide flows, the specific parameter of freestream temperature explicitly determines the nonequilibrium characteristics of the flow, which in turn play a major role in the pattern of shock interaction, as concluded in the previous section. The results presented in the previous section have also exposed that viscous effects and the resulting flow features govern shock interactions, especially in cases when the aft wedge angle is larger. As the freestream Mach number is known to have

Table 5.5: Viscous shock interactions, study I: summary of shock interaction patterns.

Geometry	PIG model	TPG model	NEQ model
15°-40°	type VI + type VI	type VI	type VI
15°-45°	type VI + type VI	type VI	type VI + type VI
15°-50°	type VI + type V with RR reflection + shock impingement pattern, Fig. 1.3b	type VI + type VI–type V transition with RR reflection	type VI + type VI–type V transition with RR reflection
15°-55°	type VI + Unsteady oscillating type V between MR reflection and RR reflection + shock impingement pattern, Fig. 1.3b	type VI + type VI + type V with RR reflection + shock impingement pattern, Fig. 1.3b	type VI + type VI + type V with RR reflection + shock impingement pattern, Fig. 1.3b

a primary role in determining shock interaction structures as well as boundary layer shapes and associated point of separation, this section dives into a parametric study with respect to this parameter. A numerical parametric study on nonequilibrium viscous shock interactions is performed with respect to the freestream Mach number over the same double-wedge configurations previously simulated.

5.4.1 Shock pattern characterization for varying freestream Mach number

15°-40° double-wedge

Figure 5.17 shows contours of Mach number and difference between translational and vibrational temperatures (which measures thermal nonequilibrium) for the flow over the 15°-40°double-

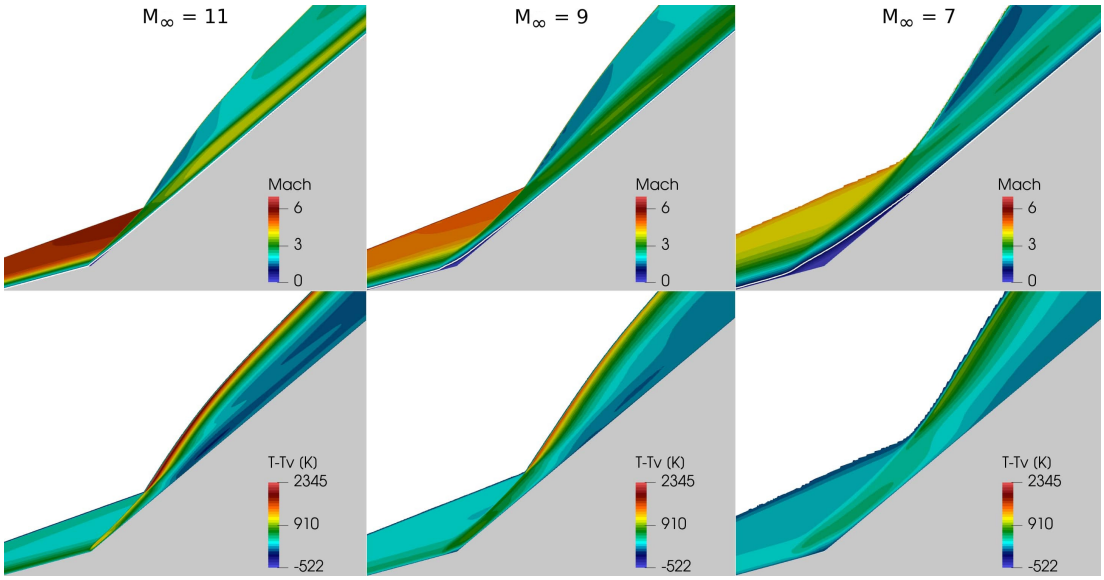

Figure 5.17: Contours of Mach number (top) and difference between translational and vibrational temperatures (bottom) for a CO_2-N_2 flow over the 15°-40°double-wedge with $M_\infty = 11$, $M_\infty = 9$ and $M_\infty = 7$.

wedge for decreasing freestream Mach number: 11, 9, 7. The white line in the top row refers to the sonic line. All three cases display a type VI interaction, characterized by the direct interaction of two oblique shocks that results in a combined shock BS, an EW and a CD or slip layer when viscous effects are present (inviscid schematic provided in Fig. 4.11b).

It is well known from inviscid gas dynamics that, in a flow over a wedge, increasing the freestream Mach number causes the oblique attached shock wave, or the detached bow shock, to move closer to the body. For the case of an attached shock, a shock that is closer to the body is as-

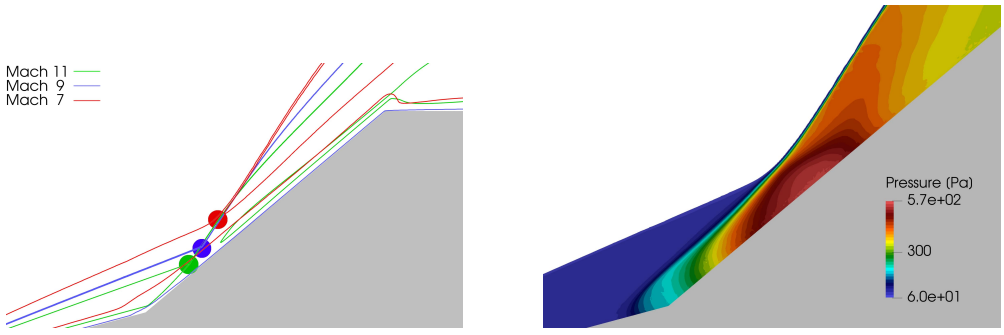

Figure 5.18: Comparison of Mach number contour lines for different values of freestream Mach (7, 9, 11) for the 15°-40°geometry (left). Contours of pressure for a CO_2-N_2 flow over the 15°-40°double-wedge with $M_\infty = 7$ (right).

sociated to a lower shock angle. In Fig. 5.18 (left), Mach contour lines for the three cases are plotted. It is clearly seen that for shock LS, which occurs only due to the presence of the first wedge, the shock angle continuously increases with decreasing Mach number, following the expected trend. The boundary layer along the surface of the first wedge is increasingly thicker for lower freestream Mach, as a result of the lower post-leading-shock flow velocity in this region. As the freestream Mach number is decreased from 11 to 7, shock CS has a larger shock angle, which in turn gives rise to a larger pressure gradient interacting with the boundary layer. Looking at Fig. 5.17, the main difference in the flow occurs in the compression corner, in the region of boundary layer detachment. The larger adverse pressure gradient travelling upstream through the thicker boundary layer causes the detachment point to occur further upstream for decreasing values of freestream Mach. Larger separation, as well as subsonic regions (indicated by the white line in the top row of Fig. 5.17), result from the lower freestream Mach. For all three cases, the size of the separated flow region is small enough that no reattachment shock occurs. Instead, the gradual reattachment of the boundary layer results in a series of compression waves that coalesce into the detachment shock, which can be visualized clearly at the right hand side of Fig. 5.18, showing pressure contours for a zoomed view of the compression corner for the case of $M_\infty = 7$. The detachment shock interacts directly with shock LS at the triple-point P, generating features BS, EW and a viscous slip layer. The contour lines displayed at the left side of Fig. 5.18 for all three cases show that the triple-point P tends to travel downstream and further away from the wall as the Mach number decreases. Following the trend observed for the leading shock, the bow shock standoff distance also increases with lower freestream Mach number.

Figure 5.19 shows the distribution of surface quantities, normalized pressure and Stanton number. As expected, lower values of freestream Mach number result in lower distributions of pressure and Stanton number along the whole surface of the geometry. From the surface pressure distribution, the single stage of flow compression at the wall seen for $M_\infty = 9$ and $M_\infty = 11$ is an indication of the coalescence of the boundary layer detachment and reattachment into one single shock. For the case of $M_\infty = 7$, two stages of compression, resulting from detachment and subsequent reattachment of the boundary layer, can been seen. The two stages of gradual compression somewhat merge into each other and still result in a single shock. The increasing

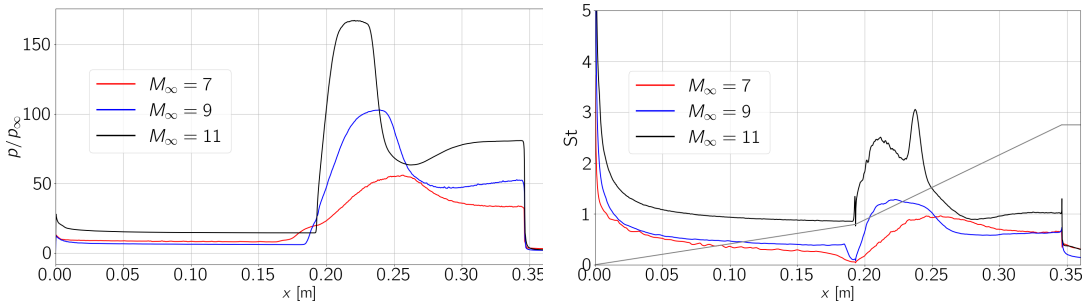

Figure 5.19: Comparison of surface quantities distribution for different freestream Mach numbers for the 15°-40°geometry. Normalised pressure (left), Stanton number (right).

size of the separated flow region with decreasing Mach number is shown by two elements for the case of $M_\infty = 7$: 1) the first increase in pressure resulting from flow separation occurs earlier and 2) the maximum value of pressure, corresponding to the point of reattachment, occurs further downstream, compared to the other two cases.

The increasing size of the separated flow region with decreasing Mach number is more evident in the wall Stanton number distribution, shown by the sudden drop of this coefficient after the initial gradual decrease along the surface of the first wedge. For the case of $M_\infty = 11$, the size of the separated region is extremely small and the sudden Stanton number drop is shown by an inverted spike at $x = 0.193$ m. Whereas the cases for $M_\infty = 9$ and $M_\infty = 7$ exhibit a qualitatively similar distribution that reflects the flow separation in the compression corner followed by gradual flow reattachment and subsequent expansion, the case for $M_\infty = 11$ is slightly more complex. There is a first spike occurring at the point of boundary layer separation. Even though the separated boundary layer is usually associated with decreasing heat flux, by visualizing contours of translational temperature and the sonic line with a close-up near the compression corner, show in Fig. 5.20, it can be seen that the detachment shock first compresses the flow against the wall just upstream the compression corner at the point of separation, $x = 0.1927$ m – which causes the wall Stanton number to spike up at this location. Immediately downstream, where the boundary layer is already detached from the wall, the Stanton number decreases suddenly due to presence of the compression corner, leading to the subsequent inverted spike seen at $x = 0.193$ m. The Stanton number then starts gradually increasing until reaching the wide peak of approximately 2.5 at $x = 0.212$ m, resulting from the gradual reattachment of the bound-

ary layer. The reattachment is indicated by the sonic line that gradually gets closer to the wall, as shown in Fig. 5.20: at the compression corner, the distance d normal to the wall between the wall and the sonic line is $d = 0.972$ mm and gradually decreases to $d = 0.639$ further downstream.

From the contours of Mach number, the Stanton number would be expected to gradually decrease up to the expansion corner, due the expansion wave. However, the maximum peak of Stanton number of around 3 is actually seen for $x = 0.2375$ m. To determine the cause of this maximum value in surface heating, Fig. 5.21 shows the distribution along the wall of the second wedge of each one of the contributions to the total heat flux, vibrational and translational, at the left. A peak of heat flux is seen for both contributions at $x = 0.2375$ m. To better understand what gives rise to these peaks, profiles of both temperatures have been extracted parallel to the surface of the second wedge, at different normal distances from the wall 0.001 m, 0.0005 m, 0.00025 m, and 0.0001 m. The temperature profiles are plotted at the right of Fig. 5.21. For h = 0.001 m, a single peak of translational temperature is seen at $x = 0.2$ m, corresponding to the temperature rise occurring in the reattachment region due to flow compression in the vicinity of the compression corner. After the rise in temperature due to the corner shock, a vibrational-to-translaional energy exchange process initiates and the translational temperature gradually decreases, while the vibrational temperature increases, reaching a peak at $x = 0.234$ m. At this location, the translational temperature starts decreasing more drastically, due to the presence of the expansion wave. As the normal distance to the wall decreases, both temperatures tend to approach 300 K, given the isothermal boundary condition enforcing thermal equilibrium at the wall, with $T_{tr} = T_{ve} = 300$ K. In the direction normal to the surface of the second wedge, towards the wall, for the same x location, internal energy exchange between the translational and vibrational mode occurs to satisfy the condition of thermal equilibrium at the wall. The more detailed analysis leads to the conclusion that the peak of heat flux seen at $x = 0.2375$ m is a combined effect of the expansion wave resulting from the shock interaction and the process of vibrational relaxation.

15°-45° double-wedge

Figure 5.22 shows contours of Mach number and difference between translational and vibra-

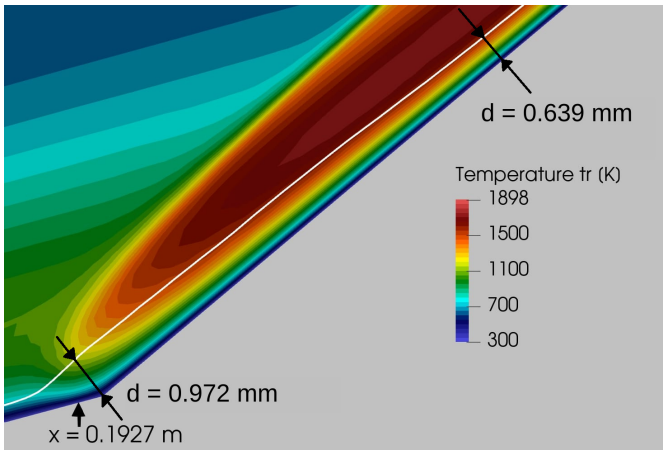

Figure 5.20: Compression corner detailed view of the 15°-40°double-wegde with $M_\infty = 11$: translational temperature with sonic line.

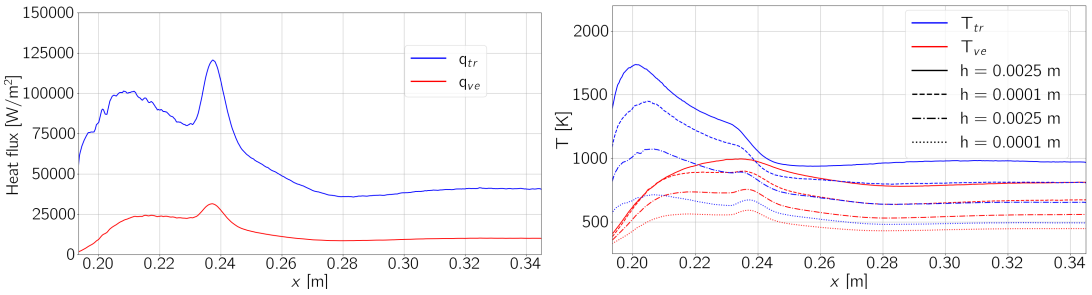

Figure 5.21: Detailed analysis of translational and vibrational heat flux contributions (left) and temperatures (right) along the surface of the second wedge, for the 15°-40°double-wedge with $M_\infty = 11$.

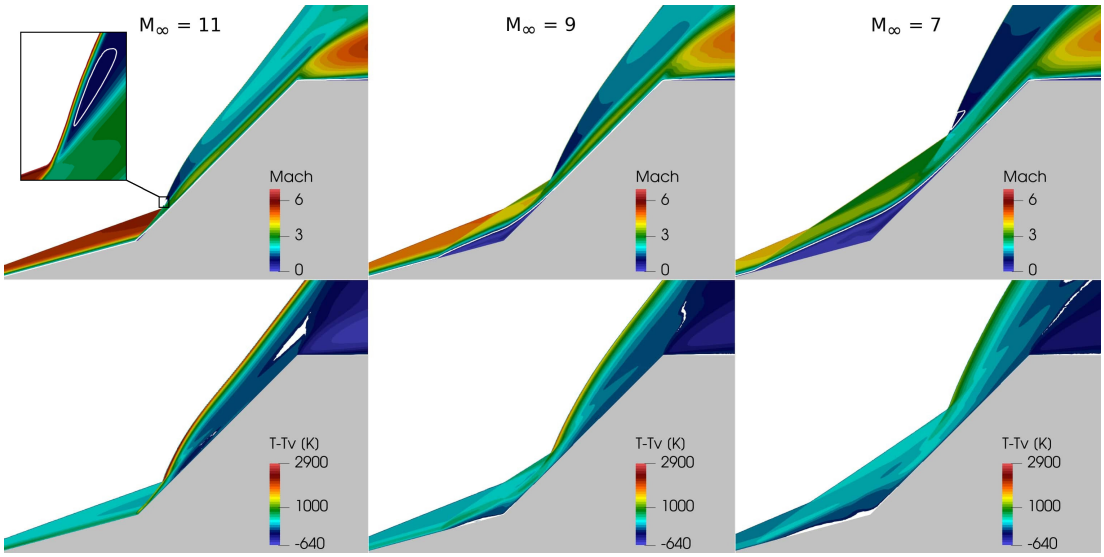

Figure 5.22: Contours of Mach number (top) and difference between translational and vibrational temperatures (bottom) for a CO_2-N_2 flow over the 15°-45°double-wedge with $M_\infty = 11$, $M_\infty = 9$ and $M_\infty = 7$. White regions in the bottom row represent thermal equilibrium. Reproduced with permission from AIAA AVIATION Forum (2022). Copyright 2022 by the American Institute of Aeronautics and Astronautics [7].

tional temperatures for the flow over the 15°-45°double-wedge for decreasing freestream Mach number: 11, 9, 7. All three cases show the type VI pattern of interaction (Fig. 4.11b). Whereas the Mach 11 flow results in the same mechanism of shock interaction as for the case of the 40°aft wedge angle (a single type VI interaction), the Mach 9 and 7 flows exhibit two instances of a type VI interaction. The more complex pattern of interaction for the two latter cases is due to the boundary layer separation occurring further upstream along the surface of the first wedge for lower Mach numbers. As per the discussion for the 15°-40°case, lower freestream Mach number results in a thicker boundary layer along the surface of the first wedge, which leads to earlier flow separation. The separation bubble is larger and so is the angle of the detachment shock, as well as the distance between the points of flow detachment and reattachment. As the detachment shock interacts with the leading shock, the first type VI pattern of interaction is formed. Further downstream, the combined shock resultant from the latter interaction, in turn, interacts with the shock generated at the flow reattachment point on the surface of the second wedge, leading to another type VI mechanism of interaction.

In Fig. 5.23, Mach contour lines for the three cases are plotted. Similarly to the 15°-40°geometry,

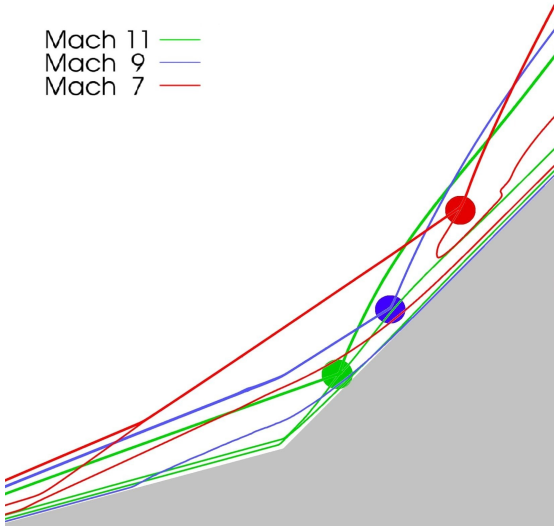

Figure 5.23: Comparison of Mach number contour lines for different values of freestream Mach (7, 9, 11) for the 15°-45°geometry.Reproduced with permission from AIAA AVIATION Forum (2022). Copyright 2022 by the American Institute of Aeronautics and Astronautics [7].

it is seen that, for shock LS, the shock angle continuously increases with decreasing Mach number, following the expected trend. Due to the different patterns of interaction resulting from different values of freestream Mach, for shock BS this trend is only verified further downstream, where there is less influence of the mechanism of shock interaction. As for the 15°-40°double-wedge, the triple-point P travels downstream and further away from the wall as Mach number decreases. The sonic line in Fig. 5.22 indicates that, besides the boundary layer, subsonic flow regions are found behind the bow shock for $M_\infty = 11$ and $M_\infty = 7$. A type VI interaction that results in subsonic pockets behind the bow shock has been named as supercritical type VI by Olejniczak et al. [3].. A very small subsonic pocket is seen just downstream the triple-point P for $M_\infty = 11$, whereas no subsonic flow exists behind the BS for $M_\infty = 9$. Even though it is expected that a lower freestream Mach number $M_\infty = 9$ would lead to lower post-shock velocities, and eventually a larger subsonic region than for $M_\infty = 11$, this is not the case. As mentioned before, the very small region of flow separation in the case of $M_\infty = 11$ generates one single shock resulting from detachment and subsequent reattachment of the boundary layer. Because these two stages of flow compression are combined into one shock, the associated shock strength and angle are larger than for the detachment shock in the case of $M_\infty = 9$, that is generated only due to boundary layer detachment. As a consequence, there is a larger

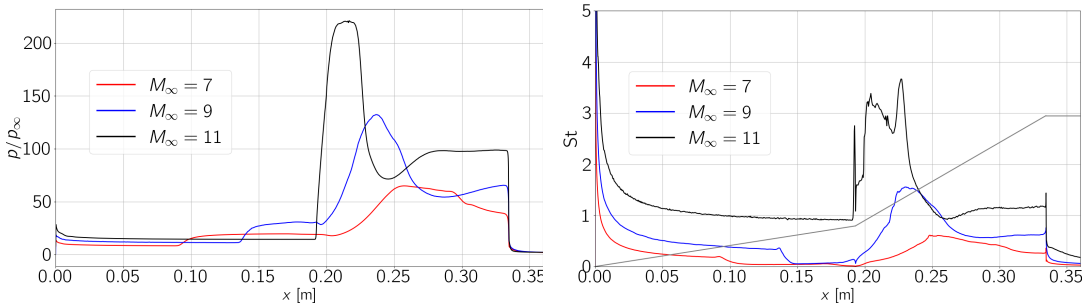

Figure 5.24: Comparison of surface quantities distribution for different freestream Mach numbers for the 15°-45°geometry. Normalised pressure (left), Stanton number (right). Reproduced with permission from AIAA AVIATION Forum (2022). Copyright 2022 by the American Institute of Aeronautics and Astronautics [7].

curvature of BS near the triple-point P for $M_\infty = 11$, leading to the lower and subsonic velocities. From $M_\infty = 9$ to $M_\infty = 7$, which result in the same interaction pattern, the expected trend of lower post-shock velocities obtained for lower freestream Mach number is obtained, with a subsonic pocket being generated for the lower freestream Mach $M_\infty = 7$.

Figure 5.24 shows the distribution of surface quantities, normalized pressure and Stanton number. For the case of $M_\infty = 11$, both distributions qualitatively follow what was obtained for the 15°-40°geometry and same value of freestream Mach. The cases of $M_\infty = 9$ and $M_\infty = 7$ present a different qualitative distribution, but both showcase the pressure variations associated to the same flow features characterising the type VI interaction: two stages of flow compression due to boundary layer detachment and reattachment followed by an expansion region. An initial increase/decrease in pressure/Stanton number is seen at approximately $x = 0.09$ m and $x = 0.135$ m, for $M_\infty = 7$ and $M_\infty = 9$ respectively, corresponding to the point of boundary layer separation. Further downstream, the peaks of pressure and Stanton number seen at $x = 0.23$ m and $x = 0.255$ m, respectively, are associated with the reattachment of the boundary layer. The parametric study shows that, for lower freestream Mach numbers, the larger separated regions reattach more gradually, which is indicated by the significantly wider peaks of pressure and Stanton number.

15°-50° double-wedge

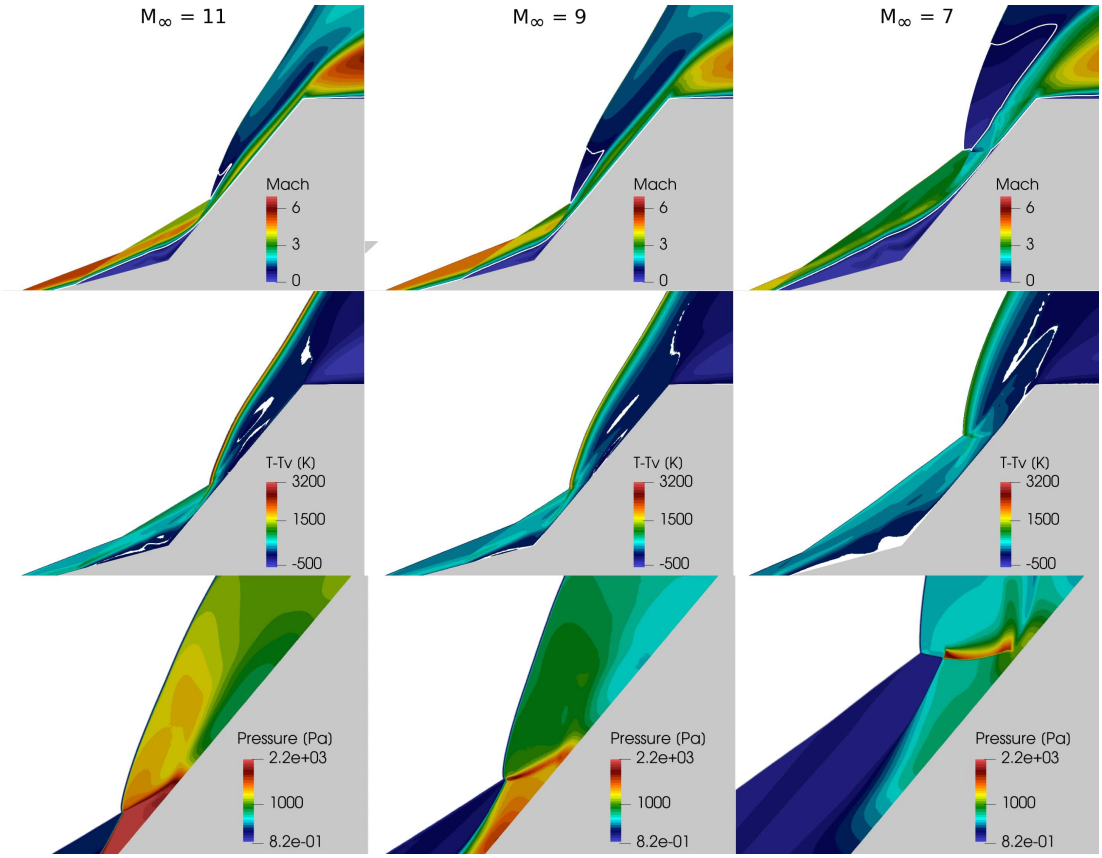

Figure 5.25: Contours of Mach number (top), difference between translational and vibrational temperatures (bottom) and pressure (bottom) for a CO_2-N_2 flow over the 15°-50°double-wedge with $M_\infty = 11$, $M_\infty = 9$ and $M_\infty = 7$. White regions in the bottom row represent thermal equilibrium.

Figure 5.25 shows contours of Mach number (top row), difference between translational and vibrational temperatures (middle row) and pressure in a zoomed view on the region of interaction (bottom row) for the flow over the 15°-50°double-wedge for decreasing freestream Mach number: 11, 9, 7. As the aft wedge angle increases from 45°to 50°, for each value of freestream Mach number, the separated flow region in the compression corner continuously thickens, resulting a reattachment shock characterized by a larger shock angle. The bow shock becomes stronger and has a wider standoff distance. From the previous geometry, the way the shock interaction mechanism develops reflects the latter changes, leading to a transition between type VI and type V for the cases of $M_\infty = 11$ and $M_\infty = 9$ and to a fully established type V (Fig. 4.11a) for $M_\infty = 7$.

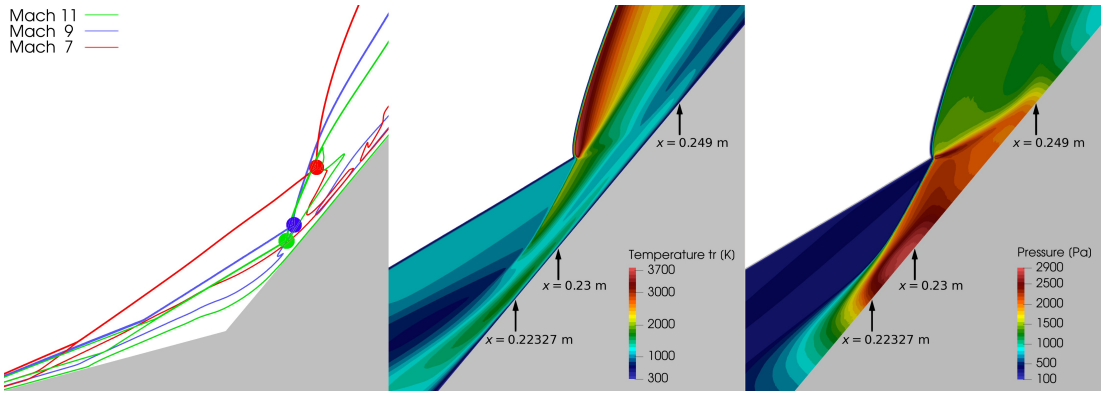

Figure 5.26: Comparison of Mach number contour lines for different values of freestream Mach (7, 9, 11) for the 15°-50°geometry (left). Detailed view of the shock interaction region for the 15°-50°double-wegde with $M_\infty = 11$ (middle – translational temperature, right – pressure).

Compared to $M_\infty = 9$, the pattern of interaction obtained for $M_\infty = 11$ is closer to the supercritical type VI. Looking at the pressure contours in Fig. 5.25, the case of $M_\infty = 11$ appears to generate a pattern of interaction corresponding to the system of two shock waves interacting, leading to a combined shock BS, an EW and a slip layer – which would correspond to the type VI interaction. However, the accentuated curvature of the bow shock near the triple-point and the subsonic pocket behind it (white line in the Mach contours) suggests a transition to the type V pattern [89]. For $M_\infty = 9$, the mechanism of interaction displays additional flow features and shocks that are difficult to visualize in the Mach contours but become evident in the zoomed view of the pressure contours. Specifically, the reattachment shock is reflected as shock RS2 (with pressure contours changing from orange to dark red), which in turn impinges on the surface of the second wedge.

When the freestream Mach number is further decreased to 7, a more complex interaction system is obtained due to the larger number of shock waves. From Fig. 5.26 (left), it is seen that the significantly larger separated flow region, as well as significantly larger angle of the detachment shock, cause the triple-point to travel further downstream. The stronger shocks in the main region of interaction, characterized by larger shock angles, push the triple-point further away from the wall. From the triple-point, a transmitted shock is generated and reflected on the reattachment shock, in a regular reflection shock system corresponding to the type V interaction (pressure contours). Another key feature of this pattern of interaction is the impingement of shock RS2 on the surface of the aft wedge (check schematic Fig. 1.3b). This flow feature

results in a SWBLI that is strong enough to cause boundary layer separation (indicated by the sonic line in the Mach contours) and therefore generate additional separation and detachment shocks. The detachment shock is seen in the pressure contours in the transition from sage green to dark green, and the reattachment shock is indicated by the transition from dark green to lime green – both near the surface of the aft wedge, in the region of shock impingement.

Figure 5.27 shows a comparison of surface properties for all 15°-50°cases: Mach 11, 9 and 7. For $M_\infty = 11$, up until the pressure peak, the surface pressure distribution follows what is expected from a standard type VI interaction: the first increase in pressure corresponding to the separation of the boundary layer and the peak reflecting the subsequent reattachment. Before the flow fully expands along the surface of the aft wedge, another very small local pressure peak is seen at $x = 0.248$ m. This is an indicator that the flow pattern is not a standard type VI, but instead is transiting to a type V. This small pressure peak is indicative of the flow compression associated to a very weak shock impinging on the surface – weak enough that can not be visualized in the flow contours, but still affects the surface distributions. When it comes to surface heating, the initial drop of Stanton number at $x = 0.11$ m reflects the point of boundary layer separation. Further downstream, the Stanton number distribution exhibits a few fluctuations, reflecting the recirculating flow inside the separation region. The reattachment of the boundary layer then causes the Stanton number to spike up to approximately 4 at $x = 0.22327$ m. At this location, a maximum of translational temperature is also visualized in the contours shown at the middle image of Fig. 5.26. The contours of pressure shown at the left of the same figure confirm that this the region of compressing flow due to reattachment of the boundary layer. The Stanton number stays approximately constant up to $x = 0.23$ m, and then starts decreasing due flow expansion downstream the point of reattachment (pressure contours from red to orange along the wall). Another spike is seen further downstream at $x = 0.249$ m, this latter spike being due to the weak shock impinging on the surface of the aft wedge. The Stanton number then gradually decreases along the wall up to the expansion corner.

The surface distribution for the case of $M_\infty = 9$ is quite similar to the one for $M_\infty = 11$, confirming that both cases result in a similar mechanism of shock interaction. The fact that $M_\infty = 9$ results in a transition type VI–type V that is closer to the fully established type V interaction is shown by the second spike of pressure. Whereas for $M_\infty = 11$, the weak impinging

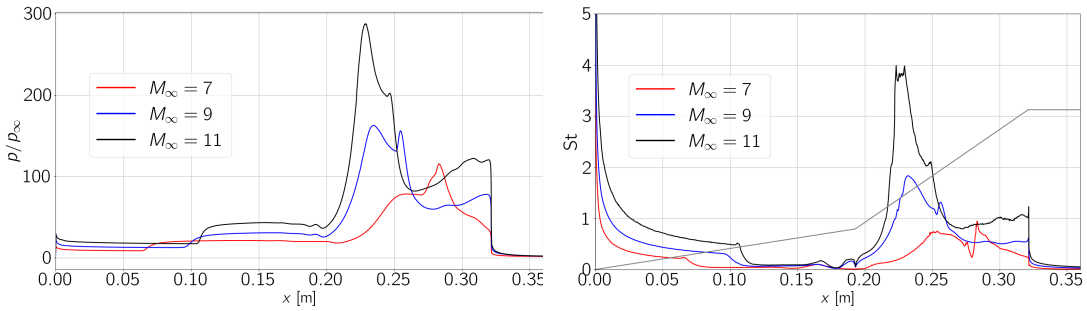

Figure 5.27: Comparison of surface quantities distribution for different freestream Mach numbers for the 15°-50°geometry. Normalised pressure (left), Stanton number (right).

shock leads to a surface pressure spike that is 0.7 times smaller than reattachment peak, for $M_\infty = 9$, the compression associated to the impinging shock is comparable to the one caused by boundary layer reattachment. The Stanton number distribution for the $M_\infty = 9$ case reflects the aforementioned behaviour, where instead this quantity drops in the region of flow separation. For $M_\infty = 7$, the significantly longer separated flow region and gradual reattachment is evident in both surface pressure and Stanton number distributions. Compared to the two previous cases, $M_\infty = 7$ results in qualitatively different distributions that reflects, instead, the fully established type V interaction pattern. Specifically, after the boundary layer reattachment downstream of the compression corner (that occurs approximately between $x = 0.21$ m and $x = 0.26$ m), the surface pressure distributions shows two stages of compression, that would correspond to the detachment and reattachment shocks caused by the SWBLI on the aft wedge's surface (the reattachment shock corresponding to the peak of pressure distribution). The two stages of compression are not easily distinguished in the pressure distribution. However, they become evident in the Stanton number plot, where the separation is shown by the sudden drop at $x = 0.279$ m and the following spike at $x = 0.283$ m reflects flow reattachment downstream of the shock impingement and its interaction with the boundary layer.

15°-55° double-wedge

For the 15°-55°double-wedge, all three values of freestream Mach number result in a type V interaction pattern (Fig. 4.11a). The $M_\infty = 7$ did not reach a steady state, therefore the solu-

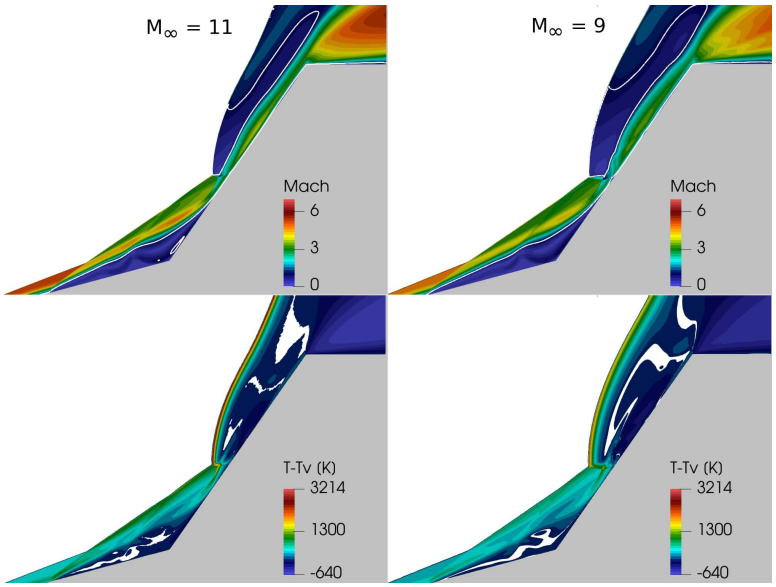

Figure 5.28: Contours of Mach number (top) and difference between translational and vibrational temperatures (bottom) for a CO_2-N_2 flow over the 15°-55°double-wedge with $M_\infty = 11$ and $M_\infty = 9$. White regions in the bottom row represent thermal equilibrium. Reproduced with permission from AIAA AVIATION Forum (2022). Copyright 2022 by the American Institute of Aeronautics and Astronautics [7].

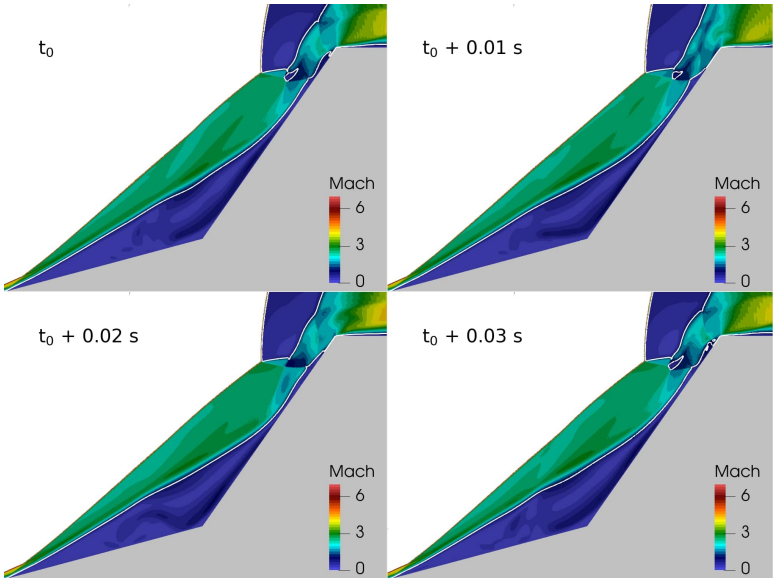

Figure 5.29: Contours of Mach number for a CO_2-N_2 with $M_\infty = 7$ flow over the 15°-55°double-wedge. Reproduced with permission from AIAA AVIATION Forum (2022). Copyright 2022 by the American Institute of Aeronautics and Astronautics [7].

tion obtained with the steady state solver was provided as a first guess to resolve the unsteady shock interaction process with time-accurate simulations. Figure 5.28 shows contours of Mach number and difference between translational and vibrational temperatures for the flow over the 15°-55°double-wedge for freestream Mach numbers 11 and 9. Figure 5.29 shows the Mach number contours for the $M_\infty = 7$ case. In this figure, contours are shown for four different instants of time, where the first and fourth instant of time depict essentially the same shock interaction pattern, showing that the flow is periodic in time.

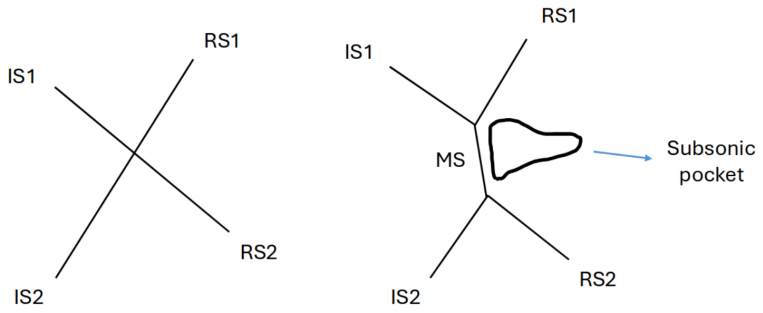

Figure 5.30: Types of shock reflection found in the type V interaction pattern: RR at the left and MR at the right.

The type V interaction pattern is characterized by the reflection of two shocks from opposite families. For the solutions presented in this section, this reflection occurs between the reattachment shock ReS and the transmitted shock TS generated at the triple-point - a schematic showing the reflection between shocks ReS and TS is shown in Fig. 5.3.2, at the two bottom rows. In the latter schematic, a regular reflection is shown. However, when two shocks from opposite families interact, the resulting reflection can be a regular reflection RR or a Mach reflection MR, where an additional normal shock, or Mach Stem MS, connects the points of reflection. The two types of shock reflection are depicted in Fig. 5.30, where IS1 and IS2 are the incident shocks 1 and 2, respectively, and RS1 and RS2 are the reflected shocks 1 and 2, respectively. In presented results, the reattachment shock ReS corresponds to IS2 and the transmitted shock TS corresponds to IS1.

For $M_\infty = 11$ and $M_\infty = 9$, a type V interaction with RR reflection is obtained. The pattern of interaction, including the flow features resulting from the presence of viscous effects, is similar. The differences between $M_\infty = 11$ and $M_\infty = 9$ follow the trends observed for the

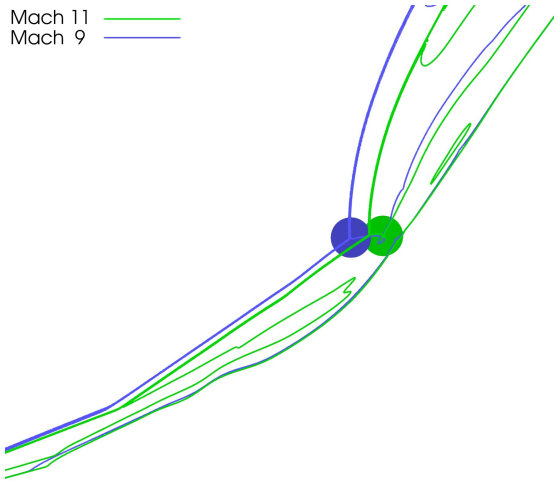

Figure 5.31: Comparison of Mach number contour lines for different values of freestream Mach (9, 11) for the 15°-45°geometry. Reproduced with permission from AIAA AVIATION Forum (2022). Copyright 2022 by the American Institute of Aeronautics and Astronautics [7].

previous geometries. A larger recirculation bubble in the compression corner is obtained for the lower Mach number, which in turn results in a leading shock and detachment shock characterized by larger angles – see Fig. 5.31. A larger subsonic region is seen behind the bow shock (see Fig. 5.32), that is also characterized by a larger standoff distance for the lower Mach number. The most significant differences in the mechanism of interaction are in the main region of shock interference, that is zoomed in in Fig. 5.32. In this region, for both cases there is shock impingement (explained in Fig. 1.3b) on the wall of the aft wedge. For the $M_\infty = 9$ case, the impinging shock is stronger and characterized by a larger shock angle, which results in a stronger SWBLI. For the $M_\infty = 11$ case, the shock induced boundary layer separation is quite small and does not generate any additional shocks. For $M_\infty = 9$, the separation resulting from shock impingement is larger enough to generate additional detachment and reattachment shocks occurring upstream and downstream of the separation point, respectively. The two shocks can be clearly visualized in the pressure contours of the bottom row in Fig. 5.32, from the transition of light blue to green contours (detachment shock) and green to yellow contours (reattachment shock). It is concluded that a more complex shock interaction pattern, with a larger number of interacting shock waves, is obtained for the $M_\infty = 9$ case. By looking at Fig. 5.31, from the locations of both triple-points, it can be extrapolated that when separation from shock impingement occurs, the main region of interaction is pushed upstream. Since a larger separation due to

shock impingement is obtained for $M_\infty = 9$, the triple-point is therefore located more upstream than for $M_\infty = 11$. It is relevant to notice that this trend is opposite of what was seen for the previous geometries.

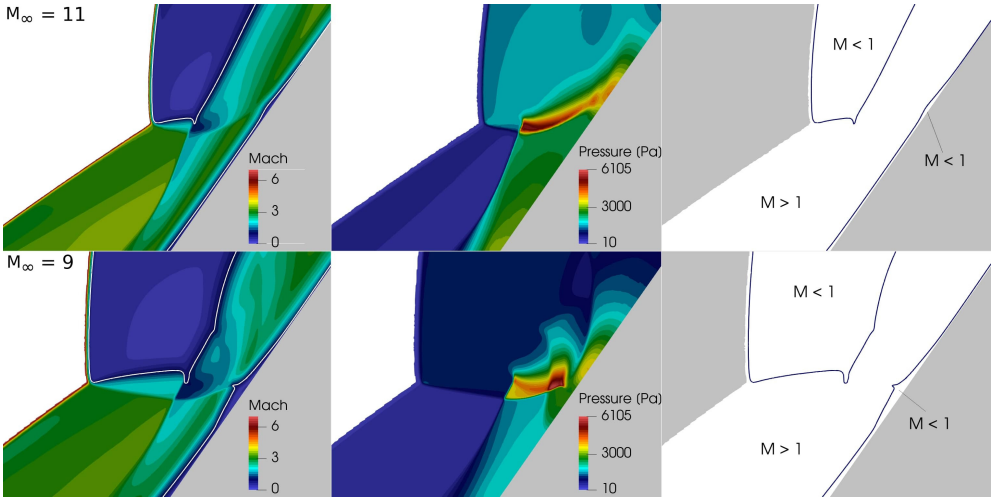

Figure 5.32: Close-up in the region of main interaction: $M_\infty = 11$ (top) and $M_\infty = 9$ (bottom) for a CO_2-N_2 flow over the 15°-55°double-wedge. Reproduced with permission from AIAA AVIATION Forum (2022). Copyright 2022 by the American Institute of Aeronautics and Astronautics [7].

The $M_\infty = 7$ case results in a periodic mechanism of shock interaction. The periodicity of the flow can be seen in the matching patterns of interaction between the first and fourth instant of time in Fig. 5.29. Comparing to the larger values of freestream Mach number, $M_\infty = 11$ and $M_\infty = 9$, the separation bubble increases significantly. The shock angles are also much larger and the location of the triple-point is substantially further downstream, towards the expansion corner. Instead of the steady type V regular reflection pattern obtained for $M_\infty = 11$ and $M_\infty = 9$, the stronger shocks lead to an oscillating type V pattern that continuously changes between a Mach reflection and a regular reflection of the reattachment and transmitted shocks. It is relevant to notice that, for this case, very large regions of the domain result in subsonic flow. Similarly to the previous cases, subsonic velocities are found in the separated boundary layer, near the compression corner as well as location of shock impingement, and behind the bow shock. For $M_\infty = 7$, an additional subsonic pocket is seen behind the Mach stem, for the first, second and fourth instants of time.

Periodic mechanisms of shock interaction have been analysed before in various works [4,9–11].

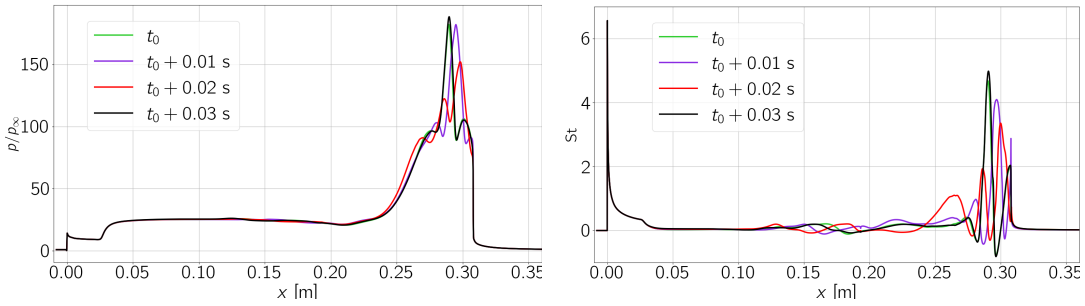

Figure 5.33: Instantaneous surface quantities distribution for the $M_\infty = 7$ flow over the 15°-55°geometry. Normalised pressure (left), Stanton number (right). Reproduced with permission from AIAA AVIATION Forum (2022). Copyright 2022 by the American Institute of Aeronautics and Astronautics [7].

Unsteadiness in the viscous type V interaction has been explained by the strong coupling between the recirculation bubble, the impinging shock and the bow shock. As the reflected shock impinges on the surface of the aft wedge and separates the boundary layer, the resulting adverse pressure gradient travels upstream through the subsonic portion of the boundary layer, and feeds the vortex dynamics inside the recirculation bubble. As the main region of interaction travels downstream, the impinging shock becomes weaker, the vortex energy inside the separation bubble decays and the motion of the whole shock system changes direction.

Figure 5.33 shows the instantaneous distribution of surface quantities for the 15°-55°double-wedge with $M_\infty = 7$ case. The periodicity of the flow pattern is here confirmed by the matching distributions of normalized pressure and Stanton number for the instants of time t_0 and $t_0 + 0.03$ s. In the normalized surface pressure plot, it can be seen that, between t_0 and $t_0 + 0.01$ s, the point of impingement travels downstream and the pressure peak intensity decreases. At $t_0 + 0.02$ s, this effect is further emphasized, and the reattachment shock already travels slightly upstream, which would correspond to the stage of decaying vortex energy (the reattachment shock is indicated by the pressure increase in the region $0.235 - 0.270$ m). The Stanton number distribution is slightly more difficult to analyse in the main region of interaction due to the numerous local minima and maxima associated to reattachment and separation regions. However, the fluctuations in the vicinity of the compression corner are a strong indicator of the unsteady vortex dynamics inside the recirculation bubble.

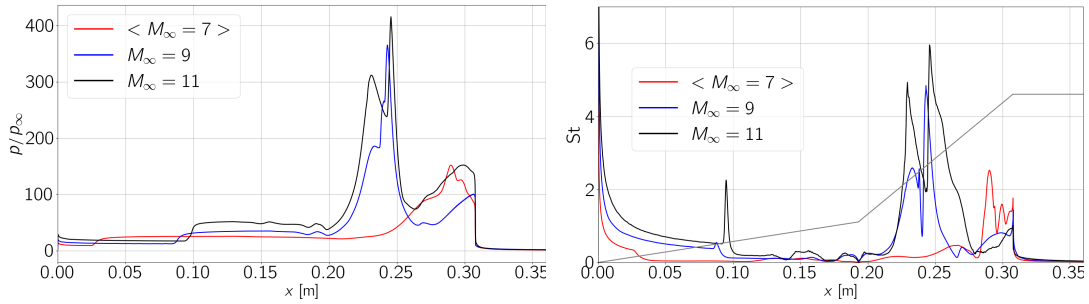

Figure 5.34: Comparison of surface quantities distribution for different freestream Mach numbers for the 15°-55°geometry. For $M_\infty = 7$, the time average is plotted. Normalised pressure (left), Stanton number (right). Reproduced with permission from AIAA AVIATION Forum (2022). Copyright 2022 by the American Institute of Aeronautics and Astronautics [7].

A comparison of surface properties for all 15°-55°cases, Mach 11, 9 and 7 is shown in Fig. 5.34. For the unsteady case, a time average is plotted. The differences in the pattern of interaction between $M_\infty = 11$ and $M_\infty = 9$ are reflected on the distribution of surface quantities. Up until the compression corner at $x = 0.193$ m, the plots are qualitatively identical. For $M_\infty = 11$, downstream of the corner, the normalized surface pressure exhibits two peaks, associated with boundary layer reattachment and shock impingement. The Stanton number distribution follows the same behaviour, with a significant decay between the two peaks, corresponding to boundary layer reattachment in the compression corner and shock induced boundary layer separation, respectively. The surface pressure of the $M_\infty = 9$ cases continuously increases from the first separation point at $x = 0.085$ m, as a result of the successive shocks: compression corner separation and detachment shocks, as well as separation and detachment shocks due to impingement. The Stanton number distribution for the case $M_\infty = 9$, at the bottom of Fig. 5.34, is also indicative of these four shocks: 1) flow separation due to the compression corner shown by the small peak and followed by decreasing Stanton number at $x = 0.088$ m, 2) subsequent reattachment peak at $x = 0.233$ m, 3) flow separation due to shock impingement indicated by the very narrow peak and subsequent decrease at $x = 0.238$ m and 4) reattachment downstream of the region of shock impingement at $x = 0.243$ m.

Similarly to the previous geometries, decreasing freestream Mach number leads to overall lower distributions of surface normalized pressure and Stanton number. Even though the red line

corresponds to a time-averaged solution, by looking at Fig. 5.33, we conclude that this is also the case for the instantaneous distributions. The maximum instantaneous normalized pressure is approximately 188 for $t_0+0.03$ s, which is 1.9 and 2.2 smaller than the largest peaks obtained for, respectively, $M_\infty = 9$ and $M_\infty = 11$. For the Stanton number, the maximum instantaneous value is 5 for $t_0 + 0.03$ s, which is 1.1 and 2 larger than maximum Stanton number values obtained, respectively, for $M_\infty = 9$ and $M_\infty = 11$.

In Fig. 5.34, it is also interesting to notice that the location of shock impingement travels upstream from $M_\infty = 11$ to $M_\infty = 9$, and downstream from $M_\infty = 9$ to $M_\infty = 7$. This is because between Mach 11 and 9 the size of the recirculation bubble and shock interaction pattern is quite similar, except for the larger separation region in the location of impingement for $M_\infty = 9$, that pushes the triple-point and the region of main interaction upstream. From $M_\infty = 9$ to $M_\infty = 7$ the size of the recirculation bubble becomes much larger and the main region of the interaction, including shock impingement, occurs closer to the expansion corner. Particularly in the case of the Stanton number distributions, vortex dynamics in the recirculation bubble is indicated by the fluctuations of surface heating from approximately $x = 0.088$ m to $x = 0.219$ m.

5.4.2 Thermal nonequilibrium effects

In this section, the role of nonequilibrium processes in defining the type of interaction is detailed in relation to the case of 15°-40°and 15°-45°wedges. The nonequilibrium effects in the case of the 15°-50°and 15°-55°cases are conceptually equivalent to those of the 15°-45°geometry. For all cases, a measure of thermal nonequilibrium is given by the contours of $T - T_v$, with white regions indicating thermal equilibrium where $T - T_v \approx 0$ (Figs. 5.17, 5.22, 5.25, 5.28).

As aforementioned, from the general theory of inviscid gas dynamics, higher Mach numbers tend to reduce the oblique shock angle and the bow shock standoff distance. When real effects play a significant role, this tendency is further emphasized: higher freestream Mach numbers lead to increasing nonequilibrium effects behind the shock, i.e., a larger amount of internal energy is transferred to the vibrational modes and dissociation reactions are more likely to occur, which overall contributes to increasing post-shock density and decreasing shock angles as well as the bow shock standoff distance [4].

The flow revealed to be chemically frozen for all the three different Mach numbers since tem-

peratures are not high enough to trigger dissociation. However, as seen at the bottom row of Fig. 5.17, the flowfield is in thermal nonequilibrium. The largest difference between translational and vibrational temperatures is obtained for $M_\infty = 11$, in the flow region just behind the bow shock. It is also for the case of higher Mach number that the difference between temperatures is the lowest further downstream as we approach the wall (dark blue contours for $M_\infty = 11$ vs. cyan/blue contours for $M_\infty = 7$). This is due to the higher post-shock pressures resulting from higher freestream Mach number, that contribute to accelerating the process of internal energy transfer between translational and vibrational modes further downstream of the bow shock, as a result of a larger number of molecular collisions. Just downstream of the detachment shock there is another region of strong thermal nonequilibrium – stronger for higher freestream Mach – which, following the same reasoning, is due to larger post-shock translational temperatures resulting from the higher freestream Mach number. In the compression corner, contrary to what is observed downstream of the bow shock, the flow gets closer to a state of thermal equilibrium with decreasing freestream Mach number. Results show that thermal equilibrium tends to be reached in regions of separated flow, where viscous effects are dominant as well as the influence from the isothermal thermal equilibrium wall. The flow times scales associated to low subsonic velocities become much larger than the times associated to vibrational relaxation. As the separated flow region enlarges with decreasing freestream Mach number, there is more thermal equilibrium in the compression corner for lower freestream Mach.

For the 15°-45°case, most part of the flowfield is in thermal nonequilibrium, as seen at the bottom row of Fig. 5.22. Contrary to the 15°-40°double-wedge, regardless the value of Mach number, the flow displays some regions where thermal equilibrium is reached (white regions). Thermal equilibrium is seen for $M_\infty = 9$ and $M_\infty = 7$ in separated flow regions. It is also seen that larger portions of the domain are in thermal equilibrium near the compression corner. Towards the expansion corner, the opposite trend is observed: as Mach number increases, which results in higher post-shock pressures, the process of internal energy transfer between translational and vibrational modes accelerates, leading to larger regions of thermal equilibrium downstream of the bow shock.

When it comes to the 15°-50°and 15°-55°geometries, no major differences are seen in the parametric study regarding the behaviour of thermal nonequilibrium effects, relative to the trends

seen for the 15°-40°and 15°-45°geometries. The behaviour of nonequilibrium effects in the context of viscous shock interaction patterns over double-wedges can be summarized as follows. There are mainly two effects playing a role in how thermal equilibrium is reached: low velocities causing flow times scale to become significantly larger than vibrational relaxation time scales; high pressures leading to more molecular collisions and therefore accelerating the process of energy exchange between vibrational and translational modes. Results have shown that:

- just behind a shock, higher freestream Mach number leads to higher post-shock translational temperature, and therefore a larger difference between translational and vibrational temperature, which means stronger thermal nonequilibrium;
- as the energy exchange process gradually occurs downstream of a shock towards the wall/expansion corner, the effect of higher pressure obtained for higher Mach number seems to prevail, and the difference between temperatures (degree of thermal nonequilibrium) is smaller for higher freestream Mach number;
- in regions of separated flow, where viscous effects are dominant, as well as the influence from the isothermal thermal equilibrium wall, the effect of flow times scales becoming significantly larger than vibrational relaxation time scales due to subsonic velocity prevails. Because the separated flow region is larger for lower freestream Mach number, it is concluded that, in the compression corner, larger regions of thermal equilibrium are obtained for lower freestream Mach number.

The summary of viscous shock interaction patterns obtained in study II is presented in Table 5.6:

Table 5.6: Viscous shock interactions, study II: summary of shock interaction patterns.

Geometry	$M_\infty = 11$	$M_\infty = 9$	$M_\infty = 7$
15°-40°	type VI	type VI	type VI
15°-45°	type VI	type VI + type VI	type VI + type VI
15°-50°	type VI + type VI–type V transition with RR reflection	type VI + type VI–type transition with RR reflection	type VI + type V with RR reflection + shock impingement pattern, Fig. 1.3b
15°-55°	type VI + type V with RR reflection	type VI + type V with RR reflection + shock impingement pattern, Fig. 1.3b	type VI + type V with RR reflection + shock impingement pattern, Fig. 1.3b

Chapter 6

Final Remarks

Motivated by the exploration of Mars and subsequent need for robust design of high-speed vehicles that perform missions to this planet, the thesis work serves as an initial endeavor to understand mechanisms of shock interaction in nonequilibrium carbon-dioxide dominated flows, as per the research aim stated reiterated below:

Research aim. The aim of the present work is the characterization and classification of shock interaction structures in hypersonic carbon-dioxide flows over double-wedges, while also investigating associated aerodynamic/thermal surface loads and the role of nonequilibrium effects. The scope of the thesis focuses on high-enthalpy flow, inviscid and viscous laminar, in thermochemical nonequilibrium with no ionization.

Section 6.1 summarises the three numerical studies that constitute the detailed analysis of high-enthalpy CO_2-N_2 flows over double-wedge geometries, each addressing the associated research question formulated in Chapter 1. Section 6.2 presents the main conclusions drawn from each of the numerical studies. Lastly, while the work contained in this thesis addresses the aforementioned research questions, further research is necessary to extend the study of nonequilibrium carbon-dioxide shock interactions to additionally focus on important physical phenomena not covered in the scope of this thesis - recommendations for future work are outlined in Section 6.3.

6.1 Summary of the numerical analysis

Chapter 4 presents numerical simulations performed to assess inviscid shock interactions structures and the role of thermochemical nonequilibrium. Simulations of hypersonic Mach 9 invisicid flow over a 15°-45°double-wedge were performed for a air-5 and a CO_2-N_2 mixture, with two different values of freestream temperature $T_\infty = 300$ K and $T_\infty = 1000$ K, considering a two-temperature model. A comparison of the previous cases with results obtained considering a perfect ideal gas model is provided to highlight the impact of nonequilibrium effects.
The first study in Chapter 5 aims at assessing viscous shock interaction patterns and the role of vibrational relaxation. Numerical simulations are conducted for a hypersonic Mach 9 viscous flow over four different double-wedge geometries, where the aft wedge angle is incremented: 15°-40°, 15°-45°, 15°-50°and 15°-55°configurations. Furthermore, results obtained with the two-temperature model accounting for vibrational relaxation are compared to two other models with simplifying assumptions: the perfect ideal gas model which neglects vibrational excitation altogether, and the thermally perfect gas model that implicitly account for vibrational excitation assuming thermal equilibrium.
The second study in Chapter 5 focuses on understanding the response of viscous shock interaction patterns in nonequilibrium carbon-dioxide dominated flows to changes the in the freestream Mach number. The same four different geometries simulated for Mach 9 nonequilibrium flow are compared to a lower and higher value of this parameter, respectively $M_\infty = 7$ and $M_\infty = 11$.

6.2 Conclusions

Research question 1

The numerical results presented in Chapter 4 reveal a large impact of nonequilibrium effects on the inviscid patterns of shock interaction, for both air-5 and CO_2-N_2 mixtures. The patterns obtained with a perfect ideal gas model completely differed from the ones obtained with a nonequilibrium two-temperature model accounting for vibrational relaxation and finite-rate chemistry. While the mechanism of shock interaction for the CO_2-N_2 resulted in a 7-shock type V with a perfect ideal gas model and a type VI with the nonequilibrium model for both values of freestream temperature, the air-5 mixtures resulted in a 9-shock type V for the perfect ideal

gas model, a 7-shock type V for the nonequilibrium model with $T_\infty = 300$ K and a type VI for the nonequilibrium model with $T_\infty = 1000$ K. These results allow to conclude that, while the freestream temperature parameter has a major influence on the nonequilibrium patterns of interaction for the air-5 mixture, the impact of the freestream temperature on the shock interaction pattern in the CO_2-N_2 flow is negligible for the range of conditions studied.

Results show that the type of interaction in the CO_2-N_2 flow is the same for the lower and higher freestream temperatures due to vibrational relaxation being much faster for the CO_2-N_2 mixture. The faster vibrational relaxation is explained by the lower characteristic vibrational temperature of the double degenerate mode of this triatomic molecule, compared to the diatomic molecules in the air mixture, N_2 and O_2. Thermal equilibrium is therefore established much faster and the CO_2-N_2 flow is mostly in thermal equilibrium downstream of the corner shock. For both mixtures, increasing the freestream temperature leads to stronger thermal nonequilibrium just behind the shocks, but faster relaxation and therefore larger regions of the flow where the mixture has reached thermal equilibrium.

Contrary to the case of air, chemical reactions are frozen with the lower freestream temperature for the CO_2-N_2 mixture case. The latter result shows that the onset of chemical activity occurs later for the CO_2-N_2 mixture, as the freestream temperature is increased. For both mixtures, nonequilibrium chemical effects become relevant for the larger temperature case with dissociation and exchange reactions gradually taking place behind the shock waves. When part of the kinetic energy is absorbed towards breaking molecular bonds, the temperature decreases, leading to lower shock angles and a flow pattern that is closer to the wall. Furthermore, dissociation reactions in the CO_2-N_2 flow with $T_\infty = 1000$ K contribute to increasing post-shock normalized pressures even when shock angles are lower than for the $T_\infty = 300$ K case.

Overall, the numerical study of inviscid shock interactions reveals that, as the freestream temperature increases, nonequilibrium effects become more relevant leading to a higher degree of dissociation and vibrational excitation of the molecules, and the pattern of interaction tends to become less complex and characterized by lower shock angles. This trend is seen when the freestream temperature is increased from 300 K to 1000 K (in the nonequilibrium cases), as well as when comparing a perfect ideal gas model to the nonequilibrium one. As vibrational excitation and chemical dissociation are accounted for and increase with temperature, a larger

amount of the kinetic energy of the flow is converted into vibrational and chemical energy, respectively. The shocks are therefore less strong, the internal translational energy behind the shocks is smaller and so is the translational temperature. The present conclusions lead to the need to understand the influence of vibrational relaxation on carbon-dioxide shock interaction patterns in more detail (isolated from chemical effects), which also motivated research question 2.1.

Research question 2.1

The nonequilibrium viscous shock interactions modelled in Chapter 5 are significantly more complex than the inviscid ones obtained in Chapter 4. Modelling viscous effects results in the presence of additional flow features such as boundary layer, flow separation, recirculation bubble, and discontinuities such as shock waves and contact discontinuities become diffused. The additional flow features generate additional shock waves that lead the shock interaction mechanism to be more intricate.

The first numerical study in Chapter 5 shows that increasing the aft wedge angle results in earlier boundary layer separation along the surface of the first wedge, leading to a larger region of flow separation in the corner between the two wedges and therefore a larger angle of the detachment shock. This trend leading to a larger angle of the detachment shock influences the shock interaction to be stronger and, overall, characterized by a larger number of shocks with larger angles, further downstream of the corner. The geometries with higher angles for the aft wedge, 50°and 55°, result in different configurations of the type V pattern, marked by shock impingement along the surface of the aft wedge. The SWBLI resulting from shock impingement is stronger for the higher angle. This causes the boundary layer to separate and additional detachment and reattachment to be generated, which results in additional complexity of the shock interaction mechanism.

Across all simulated geometries, the flow is mostly in thermal nonequilibrium. The strongest difference between vibrational and translational temperatures occurs just behind the bow shock for all cases and is larger for the larger aft angles. However, also as angle increases, larger regions of thermal equilibrium are obtained, either behind the bow shock or in regions of flow separation. Behind bow shocks, velocities are lower for stronger shocks, therefore the flow

residence time increases and becomes much larger than vibrational relaxation time, leading to a state of thermal equilibrium. Likewise, thermal equilibrium tends to be reached in other regions of low velocity such as separated regions, either in the vicinity of the compression corner or regions of flow separation due to shock impingement on the surface of the second wedge, that are also larger for larger aft angles.

For all geometries, the three models result in different shock interaction patterns. The study shows that less internal energy being transferred from the translational to the vibrational degrees of freedom results in a larger deviation of the flow across a shock wave, and larger post-shock temperatures are obtained. The larger deviation of the flow is associated with stronger shocks, lower post-shock velocities, earlier boundary layer separation and larger flow separation region in the corner. The perfect ideal gas model, which assumes no vibration excitation, results in the stronger interactions and more complex patterns types characterized by a larger number of flow features, followed by the nonequilibrium two-temperature model that accounts for the relaxation time necessary for the energy absorption process to occur. The least complex mechanisms of shock interaction, characterized by lower shock angles and a flow pattern that is more attached to the wall, are obtained with the thermally perfect gas model, which enforces instantaneous energy partition between the two energy modes and therefore enhances the effect of energy absorption by vibrational excitation. The numerical study also revealed that, for strong and complex enough interactions, the mechanism of interaction might turn out unsteady, as was the case of the 15°-55°double-wedge simulated with a perfect ideal gas model. It is known that, below a certain threshold value for the angle of the aft wedge, the flow reaches steady state after shock establishment time. The results from this numerical study show that accounting for vibrational excitation stabilizes the flow and delays this threshold, even more for the case of the thermally perfect gas model that enforces thermal equilibrium.

Since the changes in mechanism of shock interaction occur further from the wall, the qualitative distribution of surface quantities only depends on the shock interaction type. The distributions of surface properties are characterized by heat flux drops along the flow separated region as well as regions where an expansion wave impinges the surface of the second wedge. The largest peaks of pressure and surface heating occur when the flow gradually reattaches to the wall through the reattachment shock, or in regions of shock impingement for the more com-

plex types of interaction that were obtained. Despite the overall trend for more complex and stronger shock interactions in the case of the perfect ideal gas model, the more gradual flow separation and reattachment obtained with this model results in wider and lower pressure and surface heating peaks. The thermally perfect gas model results in weaker shocks and larger post-shock velocities, yielding a thinner boundary layer upon reattachment, which in turn results in the most severe surface loads of heat flux and pressure. Larger flow separation regions in the corner cause the reattachment peaks of pressure and surface heating to occur further downstream along the surface of the aft wedge, i.e., peaks of surface loads tend to occur further downstream as less internal energy is absorbed towards vibrational excitation. While the different models have a large impact on the flow features as well as distributions of surface quantities, i.e., location and intensity of pressure and heat flux peaks, the surface plateau pressure and heating in the post-leading shock and separation regions are not significantly affected. This is due to the relatively low temperatures obtained in these regions and minimal activation of the vibrational modes.

It is overall concluded that vibrational relaxation plays an active role in the mechanisms of shock interference for carbon-dioxide dominated flows, since the assumptions of different simplified models result in significant differences in terms of qualitative flow patterns as well as distributions of surface aerothermal loads.

Research question 2.2

The theory of inviscid compressible fluid mechanics states that for a flow over a single wedge, increasing the freestream Mach number causes the oblique attached shock wave, or the detached bow shock, to move closer to the body. When real gas or high-temperature effects become relevant, this tendency is further emphasized: higher freestream Mach numbers lead to increased nonequilibrium conditions behind the shock, i.e., a larger amount of internal energy is transferred to the vibrational modes and dissociation reactions are more likely to occur, which overall contributes to increasing post-shock density and smaller shock angles. In the case of the flow over a double-wedge, which presents two compression corners, different shock waves interact with each other and complex non-linear changes in the flow are expected to take place when freestream conditions vary.

The second numerical study in Chapter 5 revealed that the larger adverse pressure gradient (associated to larger shock angles) travelling upstream through the thicker boundary layer causes the detachment point to occur further upstream for decreasing values of freestream Mach. The earlier separation point results in larger size of flow separation region in the compression corner. Impingement of shocks characterized by larger angles along the surface of the second wedge also lead to stronger SWBLIs and flow separation regions. It is concluded that decreasing Mach number, associated to increased separation regions, results in additional detachment and reattachment shocks that add complexity to the types of flow pattern and lead to overall stronger shock interactions. For larger aft angles, there seems to be a threshold of the Mach number below which the flow becomes unsteady due to a strong coupling between the separated region and the entire shock system. When it comes to surface properties, larger separation regions resulting from lower Mach number lead to a more gradual boundary layer reattachment and lower and wider peaks of pressure and heat flux. Along the whole surface of the geometry, decreasing Mach number yields larger shock angles, lower post-shock velocities resulting in a thicker boundary layer and lower surface heating. Across all the simulated values of freestream Mach number, the response of the obtained shock interaction patterns to the variation of the aft wedge angle follows the conclusions drawn in the first numerical study of Chapter 5 and stated in the answer to **Research question 2.1**.

The analysis of thermal nonequilibrium in the context of viscous shock interaction patterns while varying the freestream Mach number showed that there are mainly two effects playing a role in how thermal equilibrium is reached: low velocities leading to flow times scale that are significantly larger than vibrational relaxation time scales; high pressures leading to more molecular collisions and acceleration of the energy exchange between vibrational and translational modes. Just behind a shock wave, higher freestream Mach number leads to higher post-shock translational temperature and stronger thermal nonequilibrium. As the energy exchange gradually occurs downstream of a shock towards the wall/expansion corner, the effect of higher pressure obtained for higher Mach number prevails and the degree of thermal nonequilibrium is smaller for higher freestream Mach number. In regions of separated flow, where viscous effects are dominant, as well as the influence from the isothermal thermal equilibrium wall, the effect of flow times scales becoming significantly larger than vibrational relaxation time scales due

to subsonic velocity prevails. Because the separated flow region is larger for lower freestream Mach number, it is concluded that, in the compression corner, larger regions of thermal equilibrium are obtained for lower freestream Mach number.

All in all, it is concluded that the effect of decreasing the freestream Mach number on the patterns of shock interaction and surface properties follows the same trend as the one resulting from increasing the angle of the second wedge and from simulating the flow with a gas model where less energy is absorbed by vibrational excitation, and contrary to the trend resulting from increasing the freestream temperature: flow separation regions and shock angles become larger, leading to more complex and stronger mechanisms of interaction. Accounting for thermal nonequilibrium effects, i.e., vibrational relaxation, shows to stabilize the entire shock system, by delaying the threshold for which the mechanism of interaction would become unsteady if vibrational excitation were to be neglected. Conversely, the opposite trend occurs relative to the case where thermal equilibrium is assumed.

6.3 Future work

This thesis represents a first step towards understanding the flow physics in nonequilibrium shock interaction patterns in carbon-dioxide dominated flows over double-wedges. While the work contained in this thesis addresses the aforementioned research questions, hypersonic nonequilibrium flows are characterized by multiple and complex physical phenomena. Understanding the role of each relevant physical process and the coupling between different processes on the mechanisms of shock interaction is necessary for robust design of high-speed vehicles built to travel the atmosphere of Mars. Given the complex internal structure of the CO_2 triatomic molecule and its three vibrational modes, expanding the current investigation on the role thermal nonequilibrium should consider more detailed multi-temperature models (three- and four-temperature models) and possibly the state-to-state approach in view of achieving convergence of the numerically obtained flow physics, in the scope of continuum-based macroscopic approaches. The recommended following step would be to investigate chemical nonequilibrium

effects and the influence of vibrational-dissociation coupling and ionization reactions on the viscous patterns of shock interaction and associated surface aerothermal loads.

The scope of the current thesis was limited to laminar two-dimensional hypersonic flows, but a comprehensive understanding of realistic shock interaction flows would require extending the current study to assess the impact of changing the Reynolds number and how transition to turbulence and turbulence physics affects mechanisms of shock interaction. While the two-dimensional double-wedge canonical geometry is extremely useful to lay the groundwork for the knowledge on shock interaction phenomena in nonequilibrium CO_2 flows, axisymmetric and three-dimensional simulations must be performed to understand the behavior of shock interactions in real high-speed vehicle shapes.

Appendix A

SU2-NEMO and mutation++ library

All the simulations carried out throughout this research project were performed with the CFD solver SU2-NEMO [12], a recent extension of SU2 [91]. SU2 is an open-source software suite developed to solve partial differential equations (PDEs) and PDE-constrained optimization problems. In order to capture the complex physics of nonequilibrium flows [92], an effort has been undertaken to enhance the nonequilibrium modeling capabilities in SU2, culminating in the NonEquilibrium MOdeling (NEMO) code base within the SU2 framework. This effort has extended the SU2 base code to include additional conservation equations to capture the physics of multi-component reacting flows in thermodynamic and chemical nonequilibrium, as per the equation system presented in Section 3.1.2. Extensive validation demonstrating the code's capability of modelling a variety of hypersonic flow physics is presented in [12, 93]. For details on software architecture and modularity, as well as available numerical and physical methods, the reader is referred to [12, 93].

The set of Navier-Stokes equations for hypersonic flows is not mathematically closed since it requires the modelling of the transport fluxes (shear viscosity, heat flux and diffusion fluxes), an adequate definition of the internal energy and the characterization of the source terms accounting for chemical reactions and energy relaxation in the fluid. SU2-NEMO includes a native thermochemical library containing the necessary thermo-chemistry models for specific mixtures (argon, N_2, air-5). In order to tackle the need to model a CO_2-based gas mixture, part of the work undertaken in this research project focused on enabling SU2-NEMO to simulate a hypersonic flow with any given mixture of gases. The numerical implementation carried

out in the present work extended SU2-NEMO by linking to the Mutation++ (MUlticomponent Thermodynamic And Transport properties for IONized gases) library [30]. Mutation++ is a well-validated library developed, updated, and configuration-managed by the von Karman Institute for Fluid Dynamics, utilizing high-fidelity models for nonequilibrium processes in reacting mixtures. Mutation++ provides the capability to compute thermodynamic, chemical kinetic, and transport properties for any given gas mixture. An illustration of the coupling between the CFD code SU2-NEMO and the Mutation++ library is given in Fig. A.1. For each iteration of the numerical solver, the thermochemical local state-vector $\mathbf{U} = [\rho_s \;\; (\rho e - \frac{1}{2}u^2) \;\; \rho e^{ve}]^T$ is provided to Mutation++, that in turn computes the necessary physicochemical properties as function of the local state of the mixture.

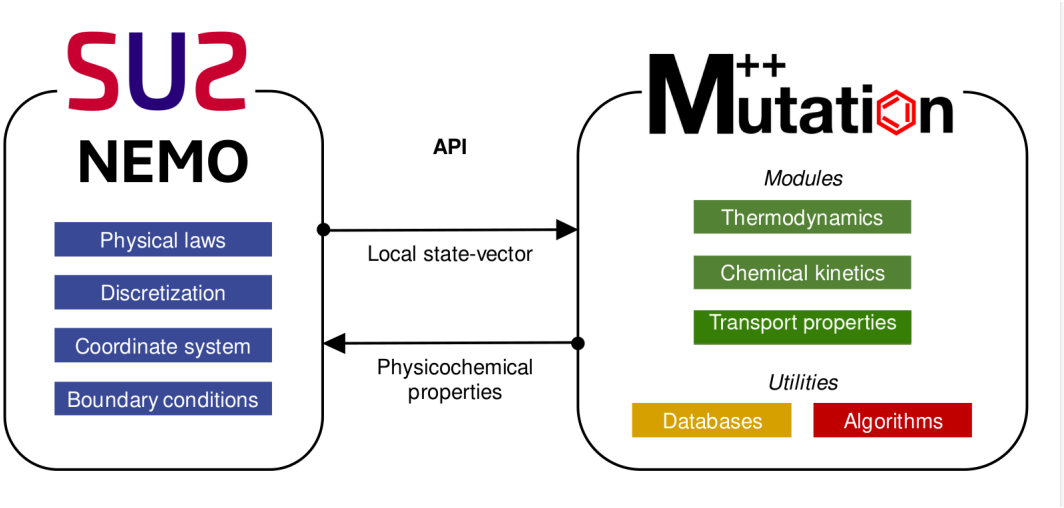

Figure A.1: Overview of the coupling between SU2-NEMO and the Mutation++ library - adapted from [30]

Appendix B

Anisotropic mesh adaptation

The flow physics encountered in double-wedge flows is rather complex, including flow features such as shock waves, boundary layer, contact discontinuities, etc. These features are very localized, highly directional and characterized by sharp gradients, typically separating regions of nearly uniform flow. To guarantee minimum computational cost in accurately capturing shock interaction mechanisms, automatic anisotropic mesh adaptation is used to generate meshes. Anisotropic meshes allow for a clustering of nodes and stretching of the elements in such a way that element faces are well-aligned with the flow features and no significant increase in number of nodes is necessary to improve the accuracy of the solution.

In this work, mesh adaptation is performed with the pyAMG library developed by INRIA [94–97]. PyAMG is a fast, robust and automatic tool that performs anisotropic mesh adaptation for complex geometries generating multi-scale and multi-direction phenomena in the flowfield. Given an initial mesh and associated CFD solution, a metric field is computed from interpolation error and surface geometric approximation. The Mach number is chosen as a variable to compute the metric field since all the flow features translate to Mach number gradient and are therefore recognized by the adaptation process. The metric field provides information about the desired element sizes and orientations in order to drive adaptation. For a finite volume solution, the interpolation error of any particular flow variable is second-order in space and can be approximated by the Hessian $H(\mathbf{x})$. The Hessian is computed by pyAMG using a double $\mathbf{L}^2$-projection [98]. The absolute value of the Hessian is used to ensure that the metric field is positive definite, and is given by

$$|\mathcal{H}| = \mathcal{R}\,|\Lambda|\,\mathcal{R}^{\mathsf{T}}.$$

The optimal metric used in the adaptation procedure is given by the $\mathbf{L}^p$-norm normalization of the Hessian for a desired mesh complexity $\mathcal{N}$:

$$\mathcal{M}(\mathbf{x}) = \mathcal{N}^{\frac{2}{3}} \left(\int_\Omega (\det |H(\mathbf{x})|)^{\frac{p}{2p+3}}\, \mathrm{d}\Omega \right)^{-\frac{2}{3}} (\det |H(\mathbf{x})|)^{-\frac{1}{2p+3}}\, |H(\mathbf{x})| \tag{B.1}$$

where the constraint mesh complexity $\mathcal{N}$ controls the desired number of DOFs in the output mesh, $\left(\int_\Omega (\det |H(\mathbf{x})|)^{\frac{p}{2p+3}}\, \mathrm{d}\Omega \right)^{-\frac{2}{3}}$ is a global normalization used to reach the desired number of DOFs, and $(\det |H(\mathbf{x})|)^{-\frac{1}{2p+3}}$ is a local normalization which gives the sensitivity to small solution variations, and is dependent on the choice of norm. For example, the $\mathbf{L}^1$-norm can be used to better capture small amplitude variations and has been shown to be effective for supersonic applications [99]. PyAMG performs successive local mesh modifications such as edge collapse, point insertion, edge swapping and point smoothing until the output mesh meets the metric requirements, as well as some mesh quality constraints to ensure the stability and enhance the performance of the CFD solver. The solution is then interpolated onto the new mesh. More information about the process as well as detailed mathematical formulation can be found in [97].

Appendix C

Code validation

The effectiveness and accuracy of the CFD solver SU2-NEMO in predicting complex flows under hypersonic conditions is examined. As with other computational physics codes, validation of the choice of governing equations and numerical models is crucial to demonstrate the suitability of the framework to provide a reliable solution to the problem in question. Code-to-code comparison is performed for the two first cases. The first case focuses on the implementation work carried out in this research project to ensure the accuracy of the numerical solution produced by the SU2-NEMO when coupled to the external library Mutation++ with respect to the modelling of thermochemical nonequilibrium. The remaining cases refer to a series of benchmark test-cases for which numerical results are compared against available experimental data, to illustrate the capability of the solver to accurately model relevant physical phenomena in hypersonic flow. Some of the data presented for validation is a product of collaborative work with other authors and appropriate referencing is provided for those - cases C.2, C.3, C.4, C.5 and C.6.

C.1 Zero-dimensional thermal bath

The zero-dimensional adiabatic thermal bath is a canonical case in the hypersonics community since it isolates the impacts of thermal nonequilibrium and finite-rate chemistry [100,101]. This case is specifically suitable to validate the implementation work done for this thesis, that concerned the coupling of SU2-NEMO to an external thermochemistry library. The Mutation++

library is called within the SU2-NEMO framework to provide mixture properties for a given nonequilibrium state of the gas, which corresponds to each mesh node within each solver iteration. Since the code has been designed to ensure modularity, the class that deals with the link to the external library is completely independent from the spatial integration over the domain of interest, which is instead handled by the numerical solver. The zero-dimensional nonequilibrium thermal bath evolving over time from a given initial condition is ideal to isolate the mixture nonequilibrium processes from the rest of the numerical solver, and therefore verify that SU2-NEMO and Mutation++ are correctly coupled.

A heat bath in thermochemical nonequilibrium was simulated using the standard 5-species air model (Air-5) with initial conditions seen below in Table C.1. Results obtained with SU2-NEMO/Mutation++ are compared to results generated using the well-established LeMANS code [102]. The thermal bath is simulated using a 5x5 structured mesh with symmetry planes on each side. An unsteady explicit time-stepping strategy is used for these cases. The results for temperature relaxation and dissociation can be seen in Fig. C.1a and C.1b.

Table C.1: Air-5 thermal bath initial conditions.

T_{tr} [K]	T_{ve} [K]	P_{∞} [atm]	$Y[N_2]$ [%]	$Y[O_2]$ [%]	Y[NO] [%]	Y[N] [%]	Y[O] [%]
15,000	300	20.42	0.767	0.233	0.0	0.0	0.0

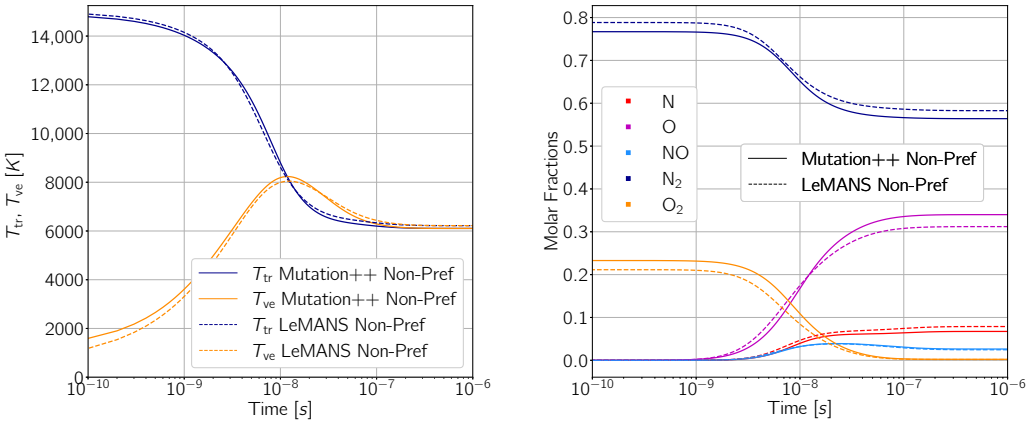

(a) Vibrational-electronic relaxation.

(b) Dissociation.

Figure C.1: Air-5 thermal bath thermochemical nonequilibrium time-evolution.

Both the SU2-NEMO/Mutation++ and LeMANS simulation data [103] show significant agree-

ment, reaching an equilibrium temperature of 6200 K at 3.5×10^{-7} seconds, as seen in Figure C.1a. The differences between the non-preferential and preferential models are significant: the non-preferential models predict greater peak T_{ve} values relative to the preferential models - 11.3% for SU2-NEMO/Mutation++, and 11.8% for LeMANS. Further, both the SU2-NEMO/Mutation++ models predict higher peak temperatures than the LeMANS models, with a peak increase of 3.5% in the non-preferential model vibrational temperature. The differences are directly correlated with the dissociation in the Air-5 models. In Figure C.1b, the impact of the preferential dissociation is noticeable, as well as the differences between the codes. In general, the preferential models begin dissociating at a slower rate, due to the preference for higher T_{ve}. This is most most notable in atomic oxygen, around 10^{-8} seconds. The percent of oxygen in the flow is tabulated in Table C.2.

Table C.2: Atomic oxygen percentage at 10^{-8} s.

	Non-Preferential	Preferential
SU2-Mutation++	14.91%	13.27%
LeMANS	17.48%	15.42%

Notably, SU2-NEMO/Mutation++ is dissociating at a slower rate than LEMANs. This is believed to be caused by differences in implementations of each code. In summary, the link between SU2-NEMO and the thermochemical library Mutation++ is validated against results obtained with the LeMANS code. As expected, the models perform similarly, with minor differences seen for the relaxation times.

C.2 Cylinder

The first validation case is the canonical hypersonic flow past a cylinder. Since the shock layer is subjected to nonequilibrium chemical and vibrational relaxation, this test-case is widely used in the aerospace community to validate and verify physico-chemical models implemented in CFD solvers [104], given the geometrical simplicity yet non-trivial flow physics. The simulated freestream conditions are shown in Table C.3. The simulations were performed on the two grids shown in Fig. C.2. The grids have the same structured boundary layer grid, with 200 equally spaced elements along the cylinder surface, and 135 elements in the normal direction, starting

with a first element height of 1×10^{-8} m from the surface and linearly growing in the normal direction with a progression rate of 1.075. The anisotropic mesh in Fig. C.2b is the result of an adaptation process of an initial isotropic mesh. The adaptation was performed using the Mach number of the steady-state solution to compute the Hessian matrix for the anisotropic metric. The number of nodes and elements can be seen in Table C.4.

Table C.3: Freestream and wall values for the cylinder case.

T_∞ [K]	901
T_w [K]	300
ρ_∞ [kg/m^3]	1.547e-03
V_∞ [m/s]	5956
Y[N]	6.5e-07
Y[O]	0.2283
Y[NO]	0.01026
Y[N_2]	0.75431
Y[O_2]	0.00713

Table C.4: Grid details for the cylinder case.

Grid	Nodes	Elements
Isotropic grid - level 0	166,694	394,534
Anisotropic grid - level 1	244,132	803,567
Anisotropic grid - level 2	339,852	1,329,244
Structured grid	141,000	189,744

The pressure at the surface is plotted in Fig. C.3a for the two grids, and compared to experimental data obtained from the High Enthalpy Shock Tunnel Göttingen, HEG [105], using 17 pressure transducers and thermocouples, covering a circumferential angle of $\pm$ 60° to measure surface pressure and heat flux distributions. The solution obtained for both grids is in good agreement with the experimental data. For a better comparison between the two grids, only a small region near the stagnation point is considered. Since the solution is not known before the generation of the structured grid, it is not possible to guarantee the local alignment of the structured grid elements with the shock wave as the distance from the stagnation line increases, therefore predicting with higher accuracy the surface quantities near the stagnation point. Both the structured and anisotropic grids show a similar pressure profile.

Similar plots near the stagnation point are obtained for the heat flux distribution in Fig. C.3b.

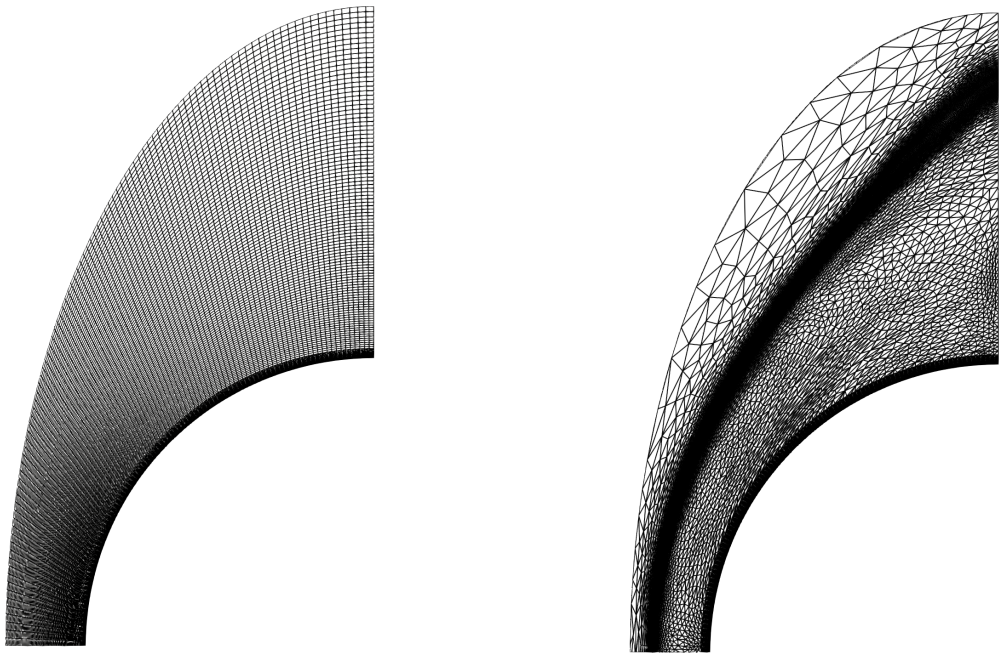

(a) Structured. (b) Unstructured anisotropic.

Figure C.2: Grids overview for the cylinder case [37].

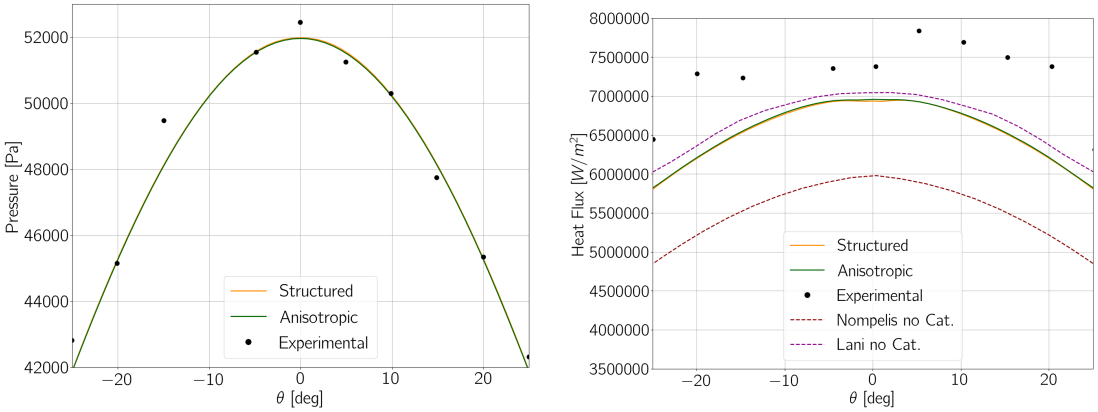

(a) Pressure. (b) Heat flux.

Figure C.3: Surface quantities plot for the cylinder [37].

The results obtained from using an anisotropic grid are identical to the solution from a structured grid. The heat flux distribution from the numerical simulations is underestimated when compared to the experimental data, due to the fact that there is no catalytic effect applied at the wall. Nevertheless, the results obtained in this work are comparable with the non-catalytic simulation results of Andrea Lani and are in better agreement than the results of Nompelis [104].

C.3 Shock wave boundary layer interaction

Accurate prediction of flow separation and turbulent heating augmentation is crucial for the analysis and design of hypersonic vehicles, particularly for endo-atmospheric flight. Besides being an excellent candidate for validation of turbulence modeling, shock wave boundary layer interaction over a compression corner is a dominant feature in the flow physics investigated in this thesis. The double-wedge geometry essentially refers to two subsequent compression corners, and the SWBLI present in each of the corners has a major influence on the overall pattern of shock interaction. Validating SU2-NEMO against the canonical case of the flow past a compression corner is a fundamental building block for the reliable solution of a hypersonic flow over the more complex double-wedge geometry. One example case of compression corner flow is the NASA Turbulence Modeling Resources (TMR) high-speed axisymmetric shock wave boundary layer (ASWBLI) test case. This geometry involves an conical/ogive cylindrical forebody with an axisymmetric flared compression corner, seen in Figure C.4. This test case is based on a set of experiments performed by Kussoy and Horstman at NASA Ames Research Center, where experimental measurements of surface pressure and heat flux were obtained for a range of compression angles between 20 and 35 degrees [106].

In this study, a three-dimensional mesh constituting a 1°wedge of a body of revolution is used, with periodic boundary conditions employed for each side. The mesh consists of $514,082$ nodes and $256,000$ quadrilateral volume elements with a wall spacing of 2.5 μm. This represents the finest grid available from the NASA TMR website, and has been demonstrated to produce grid independent solutions [107]. The flare angle chosen for this study is 20°, with the entirety of the body using an isothermal wall. Freestream values are applied at the inlet and top boundary while a standard extrapolation is used in the supersonic portion of the outlet. The freestream

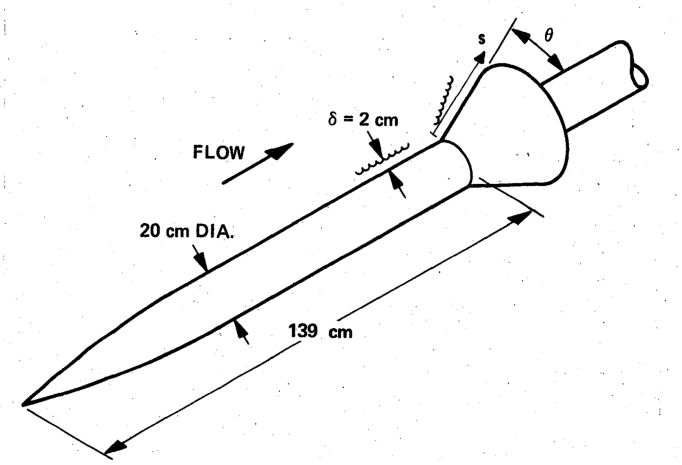

Figure C.4: Diagram of experimental configuration for axisymmetric shock wave boundary layer interaction [106].

conditions were chosen to be consistent with Georgiadis et al. [107] for simulating the flow without the conical forebody, and are provided in Table C.5. The Native Air-5 gas model was employed for this case.

Table C.5: ASWBLI freestream conditions.

M_∞	P_∞ [Pa]	T_∞ [K]	T_{wall} [K]	$Y[N_2]_\infty$	$Y[O_2]_\infty$	$Y[NO]_\infty$	$Y[N]_\infty$	$Y[O]_\infty$
7.11	550.13	80.0	311.0	0.77	0.23	0.0	0.0	0.0

Contours of Mach number over the compression corner are given in Figure C.5a. A curved oblique shock caused by the axisymmetric compression corner can be observed. At the base of the compression, there is a region of re-circulation associated with the boundary layer separation due to the impinging shock. This region can often go under-predicted if the numerical dissipation is too large. Subsequent results for this study are normalized by the surface values 6 cm upstream from the compression corner. As such, boundary layer profiles of x-velocity, Figure C.6a, and total translational temperature, Figure C.6b, are taken at this station for comparison. Numerical results are compared against available experimental data as well as numerical data obtained with the NASA code WIND-US [108]. As expected, there is little difference between the boundary layer profiles of SU2-NEMO and WIND-US. Also shown are distributions of surface pressure, Figure C.7b, and heat flux, C.7a, normalized by the values taken 6 cm prior

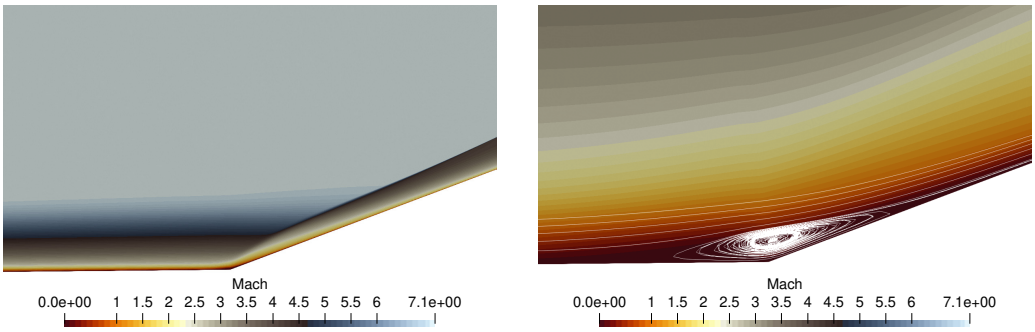

(a) Compression corner. (b) Recirculation streamlines.

Figure C.5: ASWBLI Mach contours over the compression corner [12].

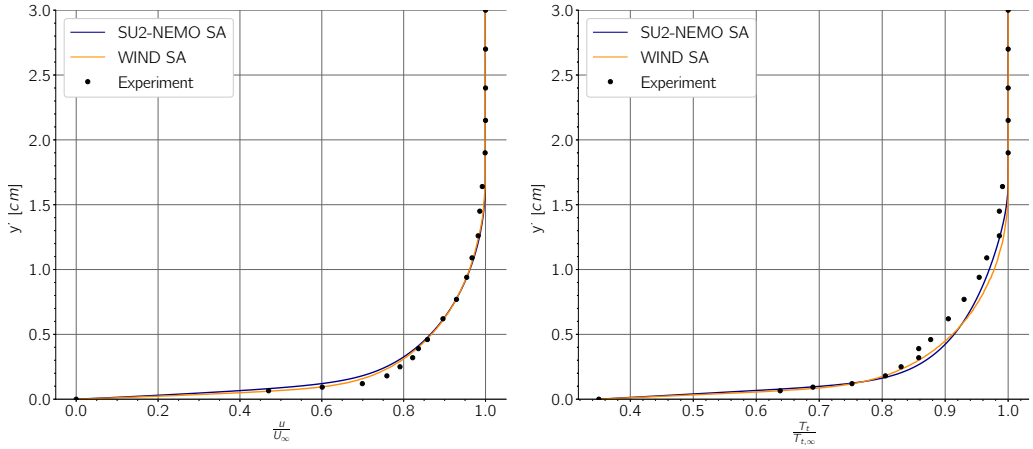

(a) Velocity profile. (b) Total temperature profile.

Figure C.6: Boundary layer profile 6 cm before the compression corner [12]. Comparison with experimental [106] and numerical [107] results.

the compression corner. The numerical results show close agreement in heat flux and surface pressure distribution in the vicinity of the shock, with some differences in the post-shock flow features. In particular, we note both sets of of numerical results underpredict the normalized pressure on the surface of the flare. SU2-NEMO predicts surface heat fluxes in a similar trend as WIND-US until 3 cm from the compression. From here, SU2-NEMO predicts a consistently higher heat flux, reaching a peak value 9.85 times the reference value and 3.46% higher than WIND-US. However, both SU2-NEMO and WIND-US over-predict the local minimum at 7 cm, and fail to predict the second peak in heat flux. Differences in peak and post-shock heat flux prediction between SU2-NEMO and WIND-US may be attributed to differences in con-

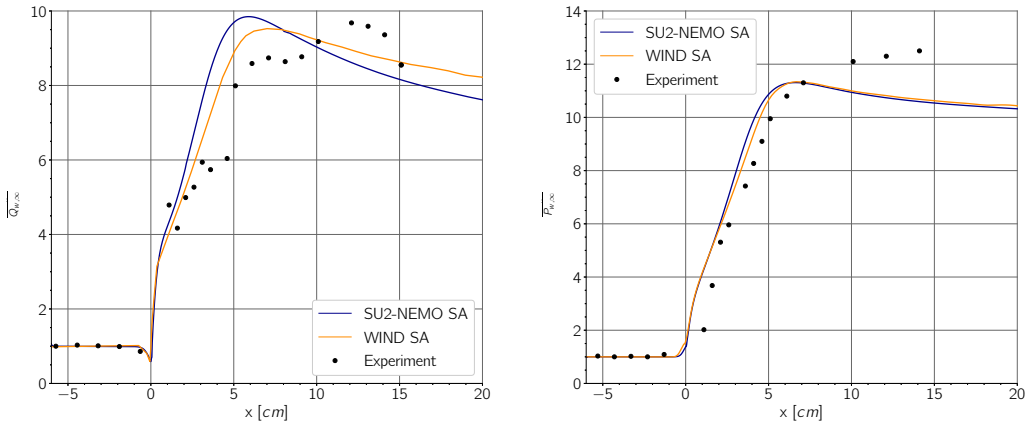

(a) Normalized surface heat flux.

(b) Normalized surface pressure.

Figure C.7: Normalized surface quantities across compression corner [12]. Comparison with experimental [106] and numerical [107] results.

vective scheme, as well as code-to-code differences. Further, it is noted that both simulation results fail to capture the second heat flux peak at 12 cm. Previous research by Georgiadis et al. found the turblent Prandtl number has a significant impact on the heat flux predictions. Using a variable Prandtl number in this case may lead to better agreement with experimental data. Experimental results are reported in [106]. In particular, Kussoy and Horstman estimate measurement uncertainties of $\pm 10\%$ for pressure and surface heat flux. While refinement and validation of the turbulence models remains an area of ongoing research and development effort in SU2-NEMO, these results show satisfactory agreement with numerical and experimental results, demonstrating SU2-NEMO's capability to model compression corner flows.

C.4 Proximal cylinders

The hypersonic flow around a complex vehicle geometry or several bodies often results in the presence of multiple shock waves, which are at the origin of shock-shock interactions and shock impingement on the surface of the body. In a flow around two proximal cylinders, the bow shock in front of the leading cylinder impinges on the bow shock caused by the second one, leading to complex flow patterns of shock interaction such as the ones investigated in this thesis. For the purpose of verifying SU2-NEMO's capability to simulate shock interactions, the flow around

two proximal cylinders is a used a second verification case, from which aerodynamic coefficients are compared with available numerical data. The freestream conditions are indicated in Table C.6 and the geometry set-up is illustrated in Fig. C.8.

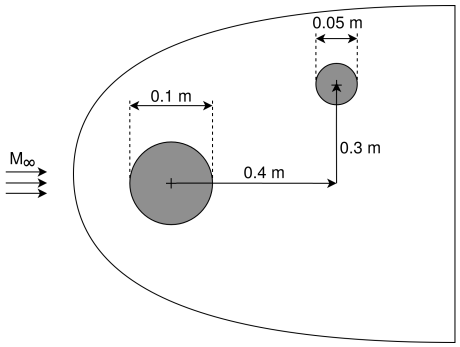

Figure C.8: Geometry configuration of the two-dimensional two-cylinder case [37].

Table C.6: Freestream and wall values of the two-cylinder case.

T_∞ $[K]$	210
T_w $[K]$	300
ρ_∞ $[kg/m^3]$	4.495e-05
V_∞ $[m/s]$	2911
N [%]	0
O [%]	0
NO [%]	0
N2 [%]	77
O2 [%]	23

The adapted anisotropic grid used in this simulation is illustrated in Fig. C.9 (left), showing a zoomed view in the region of interest, i.e., where the shock interaction occurs. The anisotropic unstructured grid is the result of an anisotropic mesh adaptation process starting from an isotropic uniform grid, following the approach described in Appendix B.

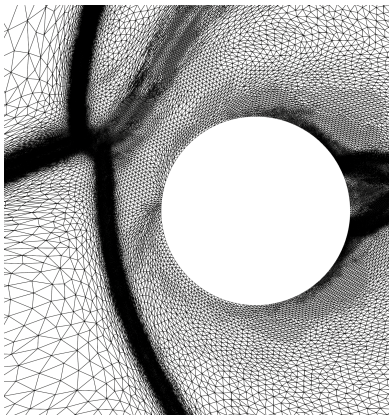

Figure C.9: Anisotropic adapted grid: zoomed view near the aft cylinder [37].

The temperature contours near the aft cylinder are illustrated in Fig. C.10. The sharply captured shock interaction pattern can be characterized as being of type VII according to the work of Yamamoto et al. [109], where the supersonic jet produced does not strike the body, but follows

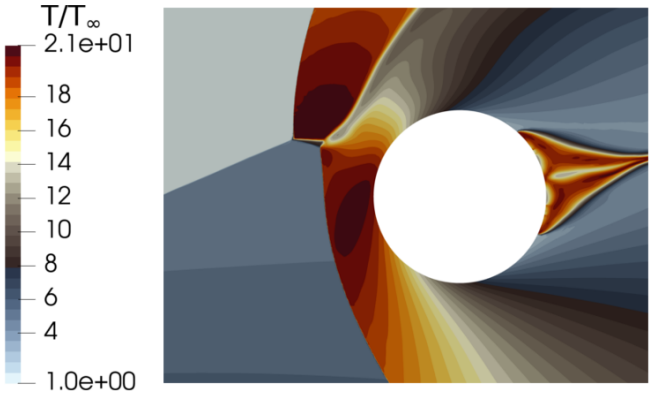

Figure C.10: Temperature contours near the aft cylinder: structured (left) and unstructured mesh (right) [37].

to the upper downstream region instead. A weak degree of the jet unsteadiness, a feature that is common for this type of interaction, can be observed from the somewhat oscillatory contours. The available numerical data for this test-case is obtained from the work of Laurence et al. [110]. The lift and drag coefficients provided by the SU2-NEMO solver using an inviscid formulation with the anisotropic grid are compared to the reference values in Fig. C.11 and Fig. C.12 respectively, showing good agreement with the available data.

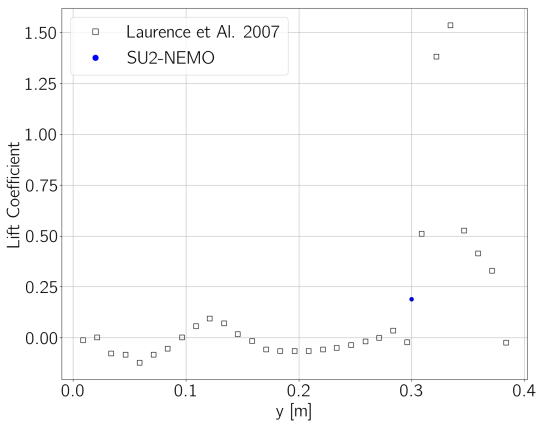

Figure C.11: Lift coefficient of the aft cylinder for a vertical displacement of 0.3 meters [37].

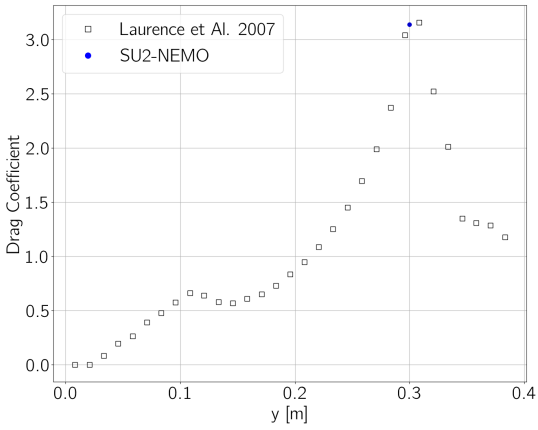

Figure C.12: Drag coefficient of the aft cylinder for a vertical displacement of 0.3 meters [37].

C.5 Proximal spheres

In this section, the simulation of a viscous hypersonic flow over a proximal-sphere configuration is validated. The shock interaction originates in the same manner as for the previous validation case but additional complexity arises from the three-dimensionality of the problem. The freestream flow conditions, wall temperature and species mass fractions for the simulation are written in Table C.7, and the case geometry is illustrated in Fig. C.13. Initially, an isotropic grid is used for the computation of the flowfield and prediction of the surface quantities. As for the case of the proximal cylinders, the corresponding solution and numerical grid are then used to drive a process of anisotropic grid adaptation. Details regarding the grids used for the simulation and convergence of the aerodynamic coefficients can be found in Table C.8. The final grid is illustrated in Fig. C.14, where a higher level of local mesh refinement and element orientation at the shock waves and shock-shock interaction region can be observed.

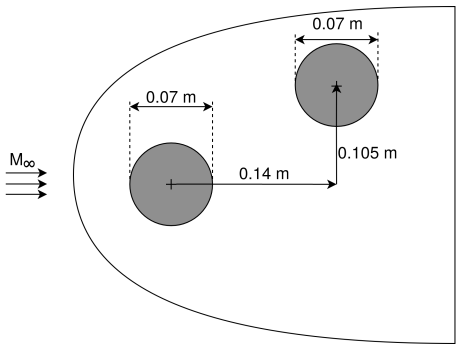

Figure C.13: Geometry configuration of the three-dimensional two-sphere case [37].

Table C.7: Freestream and wall values for the two-sphere case.

T_∞ [K]	55.56
T_w [K]	293.15
P_∞ [Pa]	125.61
V_∞ [m/s]	1048
$Y[\mathrm{N}]_\infty$	0
$Y[\mathrm{O}]_\infty$	0
$Y[\mathrm{NO}]_\infty$	0
$Y[\mathrm{N_2}]_\infty$	0.77
$Y[\mathrm{O_2}]_\infty$	0.23

Table C.8: Grid details for the two-sphere case.

Grid	Nodes	Elements	C_L	C_D
Isotropic grid - level 0	4,834,102	12,045,150	-0.13926	0.29303
Anisotropic grid - level 1	6,799,812	23,739,949	-0.13982	0.29383
Anisotropic grid - level 2	8,337,524	32,954,899	-0.14196	0.29755
Anisotropic grid - level 3	9,767,945	41,532,117	-0.14150	0.29682

Figure C.15 shows the numerical Schlieren on the left and Mach contours on the right for the final grid. The shock discontinuity and the shock-shock interaction pattern of type IV, according to Edney's criteria [6], are sharply captured. A comparison between the numerical Schlieren

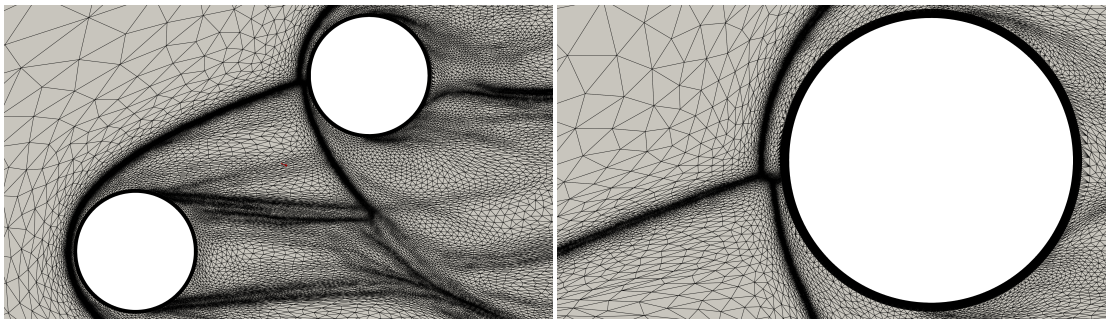

Figure C.14: Detailed visualization of the final anisotropic grid used for the two-sphere case [37].

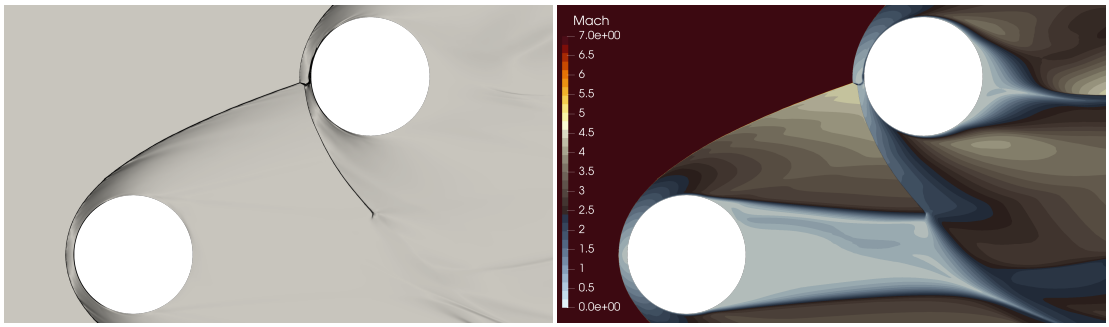

Figure C.15: Schlieren and Mach contours of the two-sphere case for the final grid [37].

of the most refined anisotropic grid and the experimental Schlieren [111] obtained from experiments conducted at the hypersonic wind tunnel H2K at DLR Institute of Aerodynamics and Flow Technology is shown in Fig. C.16. Overlaying the Schlieren images at the region of the shock-shock interaction, it can be visualized the clear superposition of the experimental and numerical shock waves, supporting the validity of SU2-NEMO to perform three-dimensional shock interaction simulations.

C.6 Free-flying ring

Another three-dimensional but still geometrically simple hypersonic flow test-case leading to shock interaction physics is the free-flying ring. Despite being a simple geometry, the ring is a good representation of an inter-stage element of a rocket. The approach of anisotropic grid adaptation reported in some of the previous cases is also applied here. The freestream conditions for the simulation of an N_2 flow are indicated in Table C.9. Figure C.17 shows

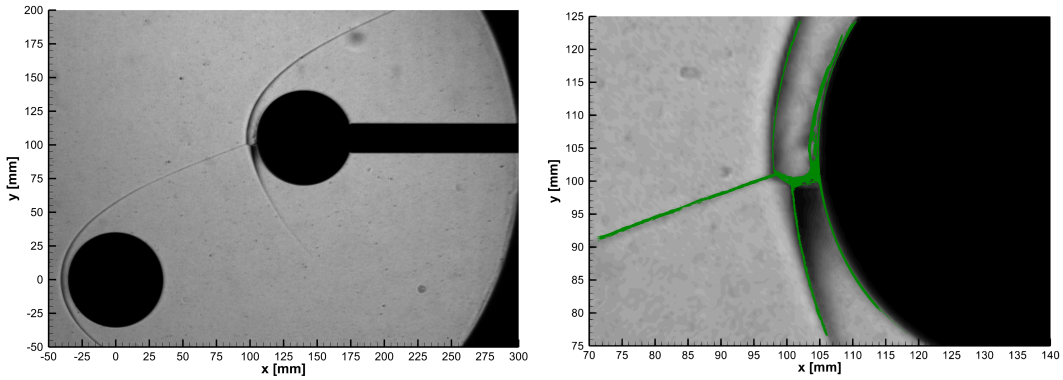

Figure C.16: Experimental Schlieren (left) and superposition of experimental and numerical Schlieren in green (right) at the shock-shock interaction region [37].

contours of Mach number for each level of adaptation (level 0 - top left, level 1 - top right, level 2 - bottom left, level 3 - bottom right) for an angle of attack of 45°. The presence of a strong shock wave along the perimeter of the ring leads to complex interaction of flow features, such as shock self-impingement. Using the hypersonic wind tunnel Longshot at the Von Karman Institute, Grossir et al. [112] conducted experimental work for the free-flying ring problem. The aerodynamic coefficients obtained with SU2-NEMO are compared with available experimental results in Fig. C.18 for the different angles of attack. A good agreement is obtained, further highlighting the capability of SU2-NEMO to reproduce complex flow physics involving shock-shock interaction.

Table C.9: Free-flying ring freestream conditions.

α [°]	V_∞	P_∞ [Pa]	T_∞ [K]
0, 30, 45, 90	2046	560.7	75

C.7 Bedford wing-body

The validation case presented in this section refers to a more realistic geometry of a hypersonic vehicle - the conceptual fuselage-and-wing Bedford body [114]. The winged configuration with symmetric lenticular wing section, is illustrated in Fig. C.19. In the context of this research project, this is most likely the most complex validation case for shock-shock and shock-

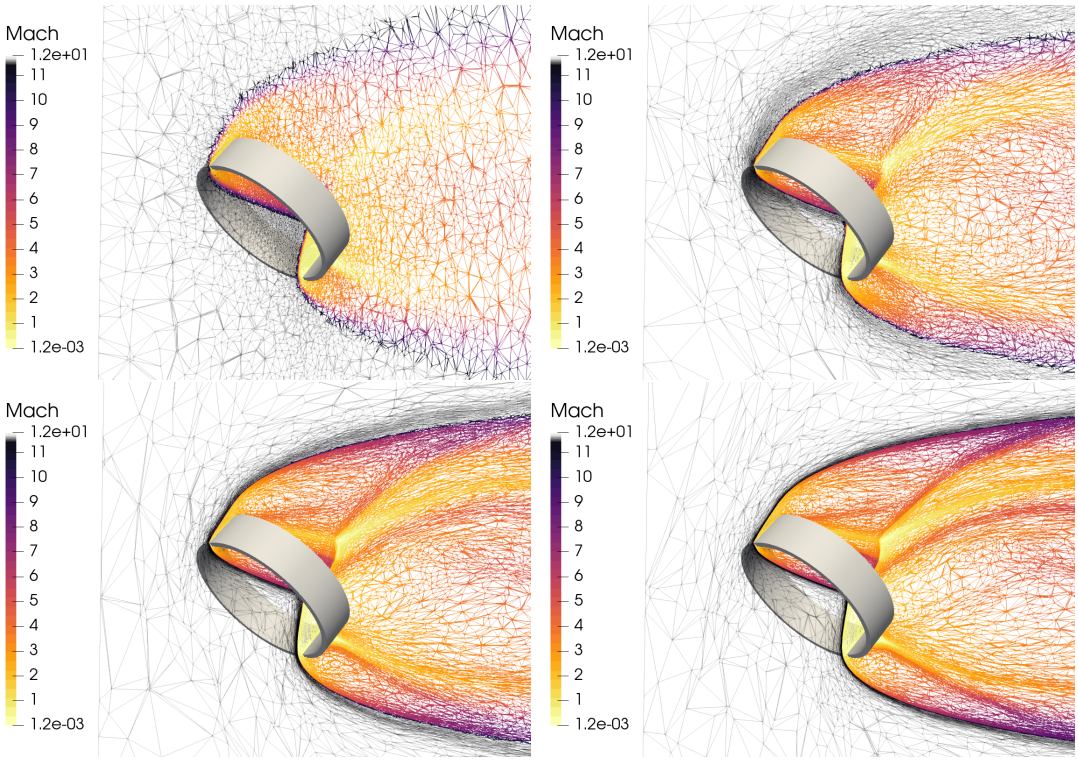

Figure C.17: Grid adaptation for a ring with 45° angle of attack [113].

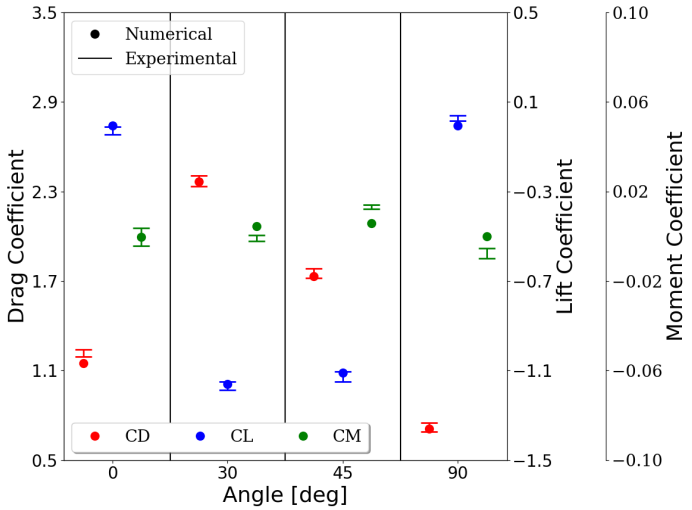

Figure C.18: Ring aerodynamic coefficients for different angles of attack [113].

boundary-layer interactions: besides the inherent complexity of the problem associated to its three-dimensionality, the fuselage-wing configuration generates highly intricate flow physics. An annotated flowfield is shown in Fig.C.20, where a schematic of the flow features that are

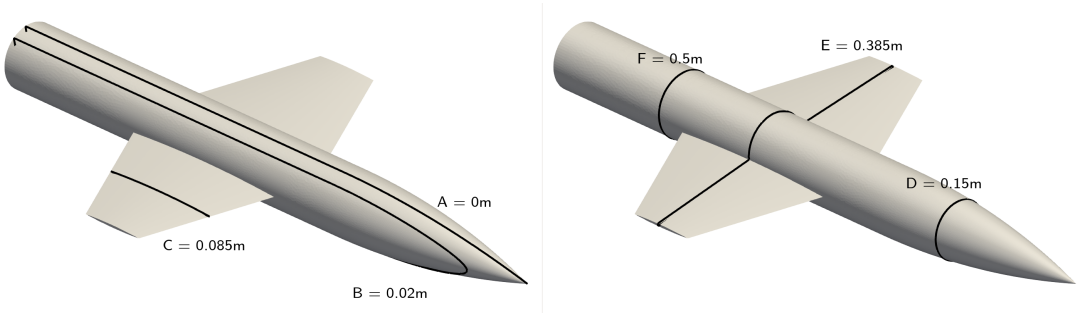

Figure C.19: Bedford wing-body: Section planes for visualisation along X and Y planes [34].

encountered in the flow surrounding the Bedford vehicle is presented. For the angle of attack of $\alpha = 20°$, the main flow features are the shock wave generated at the nose tip (stronger in the lower part of the vehicle), the shock wave that is generated at the leading edge towards the lower part of the wing and the interaction between the two. Several expansion regions can also be found: downstream of the nose shock, at the upper part of the wing and at the tip of the wing. Boundary layer separation occurs at different locations resulting from shock impingement (wing and fuselage), flow incidence on the fuselage, wing-body junction, wing trailing edge typical separation and wake in the rear part of the vehicle.

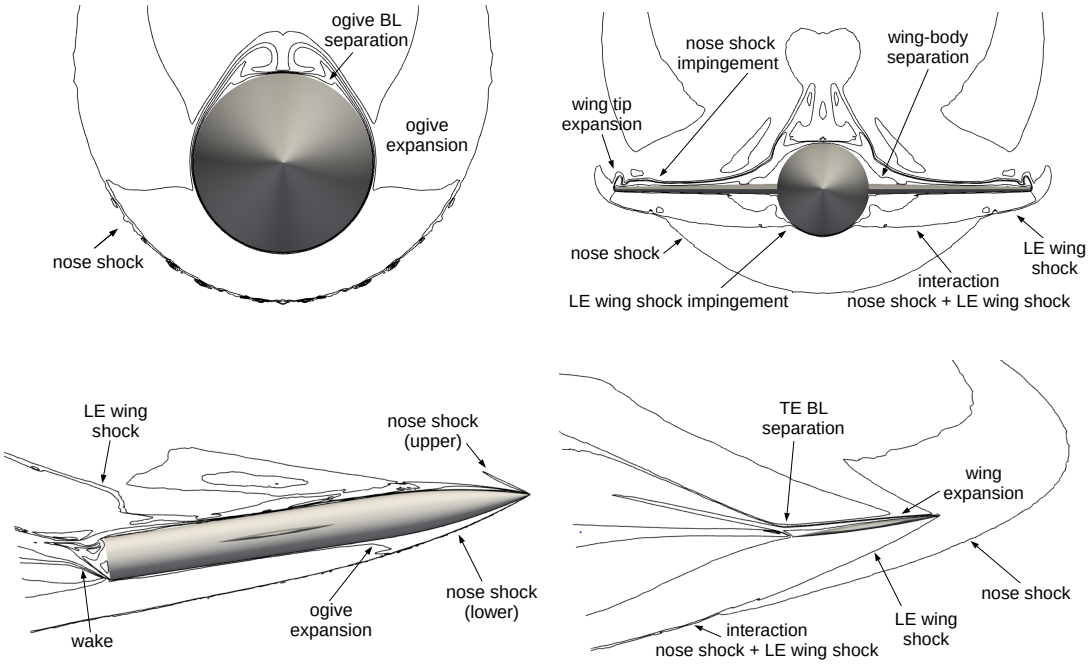

Figure C.20: Schematic of features encountered in the flowfield surrounding the Bedford vehicle [34].

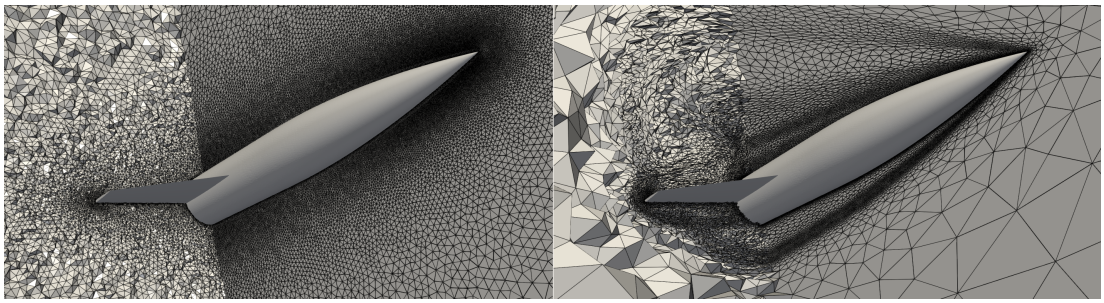

Figure C.21: Original and adapted meshes [34].

Table C.10 reports the conditions for which the simulations were performed. In this work, a hybrid meshes is used, with a quasi-structured region consisting of prismatic elements capturing the boundary layer and the remaining part of the domain discretized in an unstructured manner with tetrahedral elements. The unstructured region of the initial grid is composed by isotropic tetraheadra and the adaptation process follows the anisotropic grid adaptation approach previously explained in this thesis. For this specific case, adaptation is done only for the unstructured region and the boundary layer mesh is kept the same.

Table C.10: Bedford freestream conditions.

α [°]	M_∞	Re_∞	T_∞ [K]	$Y[\mathrm{N}]_\infty$	$Y[\mathrm{O}]_\infty$	$Y[\mathrm{NO}]_\infty$	$Y[\mathrm{N_2}]_\infty$	$Y[\mathrm{O_2}]_\infty$
20	4	91,786	300	0	0	0	0.77	0.23

Fig. C.22 shows contours of Mach number for different sections along the longitudinal and spanwise directions. Fig. C.23 reports a comparison of the aerodynamic coefficients with available experimental data. Good agreement is obtained for the final grid, validating the numerical results.

C.8 Wedge

Despite the large number of experimental studies carried out to validate the numerical modelling of hypersonic flows with mixtures of air and nitrogen, little work has focused on the specific mixture of CO_2 studied in this work. The following validation case refers to the two-dimensional wedge placed symmetrically in a uniform hypersonic flow of reacting carbon dioxide, as illustrated in Fig. C.24. The hypersonic flow over this simple geometry leads to the appearance of

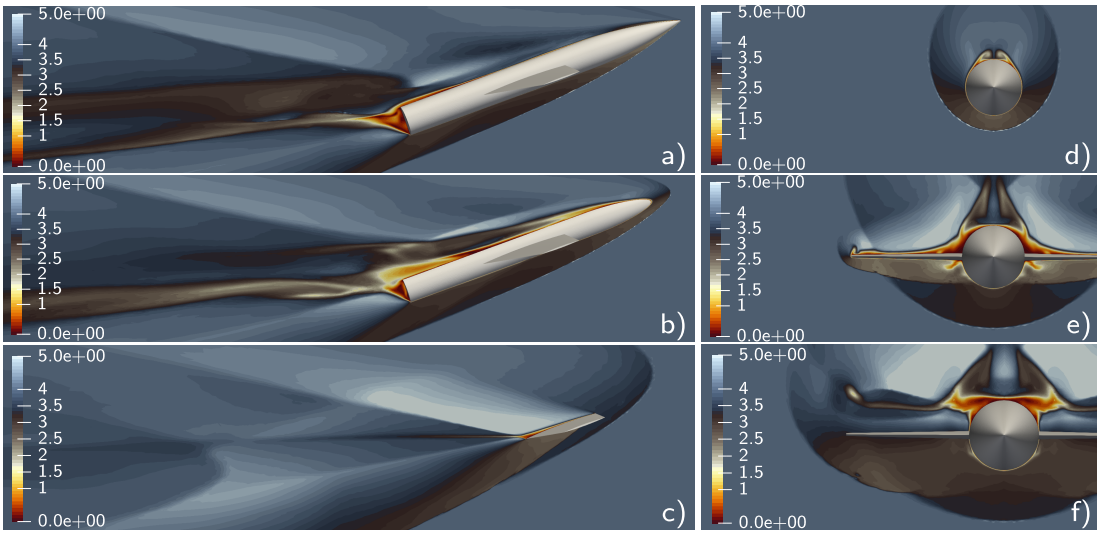

Figure C.22: Bedford wing-body Mach number contours at 20deg incidence and Mach 4. Y-axis sections (left), X-axis sections (right) [34].

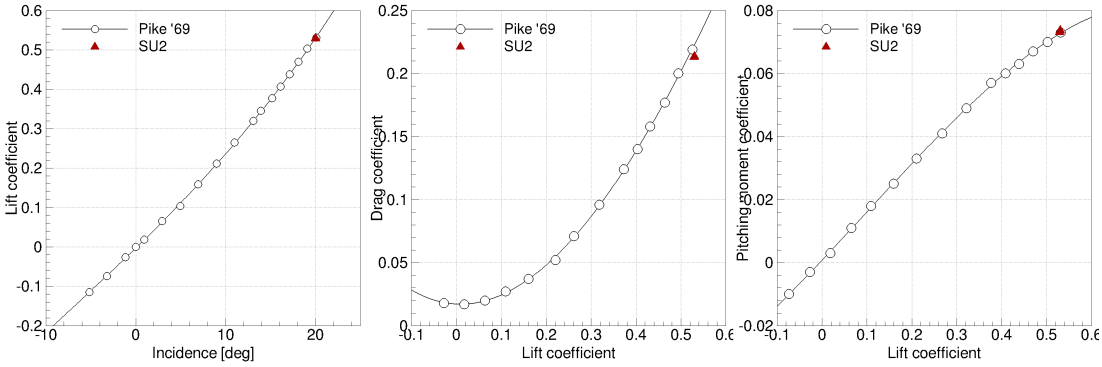

Figure C.23: Bedford wing-body at Mach 4: comparison of aerodynamic coefficients with wind tunnel data [34].

a shock wave that is detached for large enough half-wedge angles. Similar to the cylinder case, the shock layer is subjected to significant nonequilibrium chemical and vibrational relaxation that has an influence on the shock standoff distance. The validation case is taken from the work of Hornung and Smith [115], who have performed experiments in the large free-piston shock tunnel T3 using a symmetric finite-length wedge model of varying half-angle. Numerical reference data is also available from two-dimensional simulations performed by Candler [56]. The freestream conditions used in the study are shown in Table C.11. Given the flowfield symmetry, simulations carried out with SU2-NEMO considered only the upper half of the computational domain.

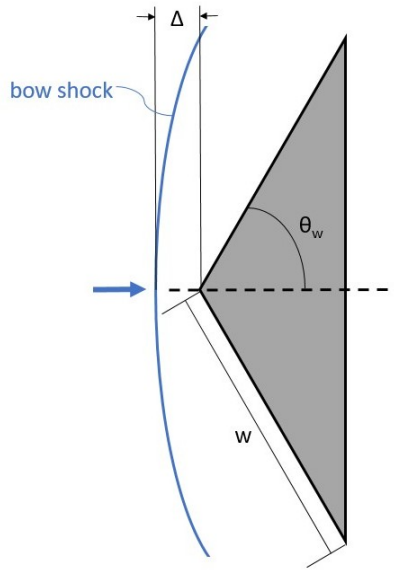

Figure C.24: Wedge geometry.

Table C.11: Freestream conditions for the wedge simulation.

M_∞	6
P_∞ [Pa]	2441.5
T_∞ [K]	1960
$Y[\mathrm{C}]_\infty$	0
$Y[\mathrm{N}]_\infty$	0
$Y[\mathrm{O}]_\infty$	0.07
$Y[\mathrm{C_2}]_\infty$	0.0
$Y[\mathrm{N_2}]_\infty$	0.0
$Y[\mathrm{O_2}]_\infty$	0.176
$Y[\mathrm{CN}]_\infty$	0
$Y[\mathrm{CO}]_\infty$	0.428
$Y[\mathrm{NO}]_\infty$	0.0
$Y[\mathrm{CO_2}]_\infty$	0.326

Figure C.25 shows a comparison of bow shock standoff distance data for different half-wedge angles. Numerical results obtained with SU2-NEMO are validated against experimental data [115] and verified against simulations performed by Candler [56]. The shock standoff distance is measured in the stagnation line, where nonequilibrium effects are expected to be more pronounced. Results obtained with SU2-NEMO are found to be in satisfactory agreement with the other two sets of data, with the case of the stronger bow shock (for a half-wedge angle of 65°) showing the largest discrepancy against both numerical and experimental reference values. The differences seen between experimental and SU2-NEMO data can be explained in part due to

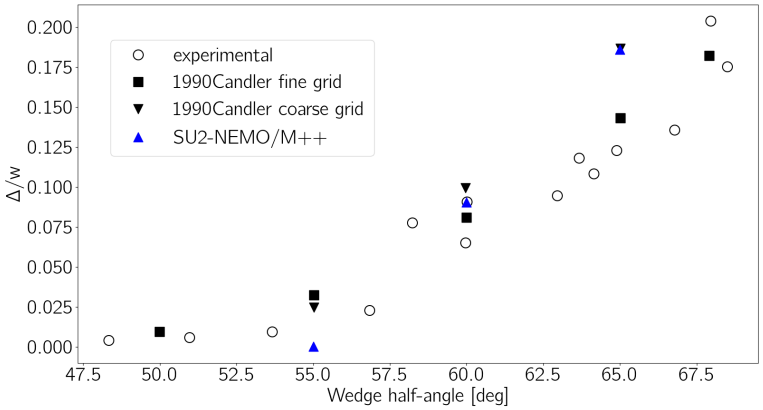

Figure C.25: Comparison of normalized shock standoff distance between numerical and experimental data.

the effect of the finite transverse length of the 3D model used in the experiments. Furthermore, the mechanism of reaction used in SU2-NEMO, as seen in Table C.11, allows for reactions involving nitrogen, which could lead to production of chemical species that are not found in the experiment. The discrepancies between sets of numerical data can be attributed to different choices in terms of the physical model. A different mechanism of reaction is considered, where a mixture of 8 species is used in the work of Candler, while SU2-NEMO aditionally considers C_2 and CN. Relaxation times for CO_2 have also been modeled differently, with the Millikan and White model [82] being used in SU2-NEMO against the Camac model [75] used in the reference work. Finally, SU2-NEMO calculates reaction rate constants with the Park model [59] while Candler takes reaction rates from the work of Evans *et al.* [116].

C.9 Double-cone

The last validation case investigates the carbon-dioxide high-speed flow over the 25°-55°double-cone, illustrated in Fig. C.26. The flow over a double-cone configuration typically results in a complex shock-shock and shock-boundary-layer interaction which is known to be sensitive to thermal and chemical nonequilibrium. The freestream conditions are indicated in Table C.12 and have been taken from the thesis of Knisely [27]. In his thesis, experiments for the flow over a double-cone were performed in the Hypervelocity Expansion Tube (HET) and the T5

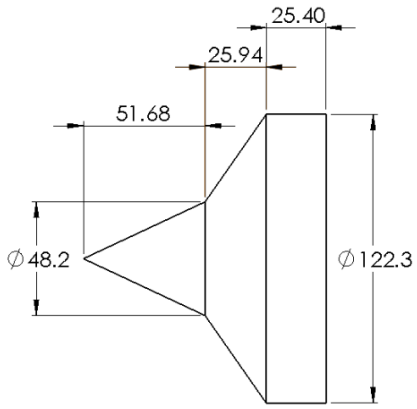

Figure C.26: Geometrical configuration for the double-cone (dimensions in mm).

hypervelocity shock tunnel for different gas mixtures. Numerical results obtained with SU2-NEMO for an axisymmetric simulation are compared with available data for surface heat flux measurements of the laminar boundary layer and with numerical predictions obtained with the DPLR code [117].

Table C.12: Double-cone freestream conditions.

M_∞	P_∞ [Pa]	T_∞ [K]	$Y[O_2]_\infty$	$Y[O]_\infty$	$Y[CO_2]_\infty$	$Y[CO]_\infty$	$Y[C]_\infty$	$Y[C_2]_\infty$
4.41	12300	1530	0.1152	0.0038	0.6726	0.2084	0.0	0.0

Contours of Mach number obtained with SU2-NEMO are shown in Fig. C.27 and a graphical comparison of numerical schlieren between SU2-NEMO and experimental data is provided in Fig. C.28. In agreement with the experimental results of Knisely [27], the CO_2 flow over the double-cone results in a type V shock interaction pattern. The flow pattern defined by the appearance of the seven shock interaction structure arises from the interaction between the leading shock generated at the nose and the reattachment shock in the vicinity of the compression corner. Besides these two shocks interacting in a regular-reflection structure, a separation shock is seen at the location of boundary layer separation along the surface of the first wedge, ahead of the corner. Even though the same pattern of interaction is obtained, the graphical comparison shown in Fig. C.28 reveals significant discrepancies regarding the location of certain flow features such as the triple-point, the bow shock position and the points of boundary layer de-

tachment and reattachment. The flow reproduced experimentally by Knisely has been identified as transitional, whereas the SU2-NEMO simulation capabilities are limited to flow modeling in the laminar regime. Not capturing the transition to turbulence in the numerical simulation could explain the discrepancies observed, as the location of the afore-mentioned flow features largely depends on the behavior of the boundary layer and how the adverse pressure gradient travels upstream through its subsonic region. Excellent agreement is obtained for the position of the oblique leading shock, which is not influenced by transition to turbulence.

The surface heat flux profile can be broken down into four general sections: the laminar boundary layer, separated flow region, reattachment-impingement region, and post-reattachment region. In Fig. C.29, data obtained with SU2-NEMO is compared against experimental measurements and numerical results obtained with the DPLR code. For the latter, the axisymmetric simulation was performed for a single cone geometry (equivalent to simulating the laminar flow region in the double-cone case). For the laminar region, a very good agreement is found between all three sets of data. The DPLR results differ from SU2-NEMO and experiments from the point of boundary layer detachment, since this flow feature does not occur for the single-cone geometry. The different locations of boundary layer detachment between SU2-NEMO and experimental results is evident in this plot, with flow separation occurring at $s/L = 0.75$ for the experiment and at $s/L = 0.93$ for the numerical solution. From this point on, simulating transitional and turbulent flow with laminar flow models is expected to significantly impact the wall heat flux and the agreement between results becomes poor. Nonetheless, for the flow region where the flow is laminar, very good agreement is found between all three sets of data, demonstrating the accuracy of SU2-NEMO and its coupling with the Mutation++ library in predicting hypersonic laminar flow physics using CO2-based mixtures.

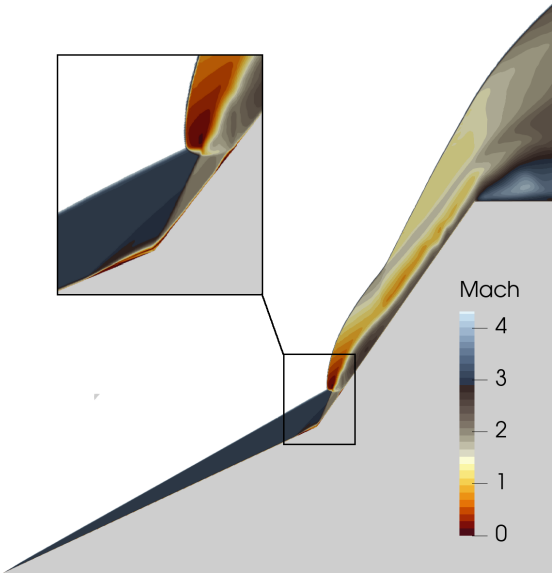

Figure C.27: Contours of Mach number for the CO_2 flow over the double-cone.

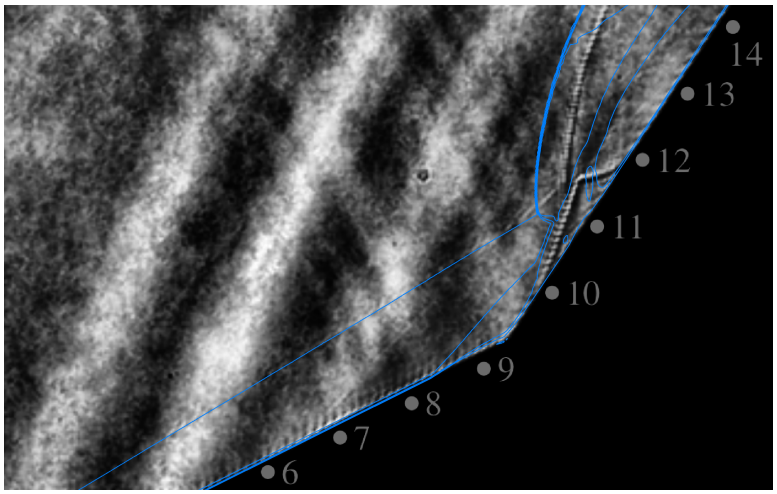

Figure C.28: Graphical comparison of numerical schlieren contours with experimental data [27].

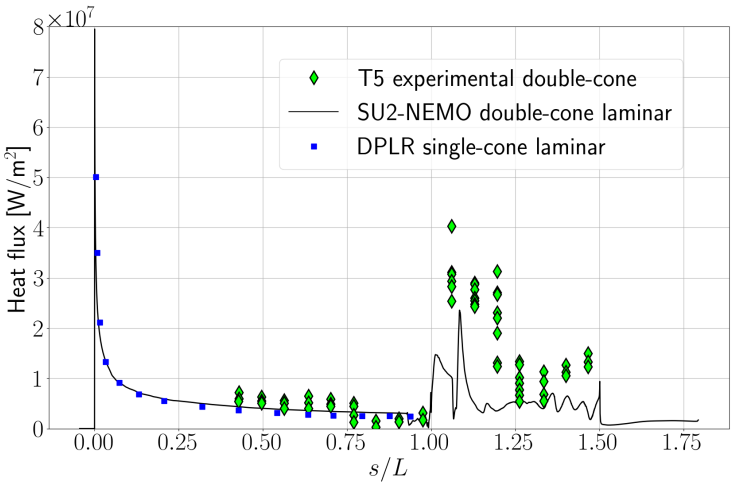

Figure C.29: Comparison of surface heat flux predictions with experimental data.

Bibliography

[1] Joe. D Watts. Flight experience with shock impingment and interference heating on the x-15-a research airplane. Technical Paper TM X-1669, NASA, 10 1968.

[2] Ahmet Durna and Bayram Celik. Time-periodic shock interaction mechanisms over double wedges at Mach 7. *Shock Waves*, 29, 03 2019. 10.1007/s00193-018-0864-7.

[3] J. Olejniczak, M. Wright, and G. Candler. Numerical study of inviscid shock interactions on double-wedge geometries. *Journal of Fluid Mechanics*, 352:1–25, 12 1997. 10.1017/S0022112097007131.

[4] C. Garbacz, F. Morgado, and M. Fossati. Effect of thermal nonequilibrium on the shock interaction mechanism for carbon dioxide mixtures on double-wedge geometries. *Physics of Fluids*, 34(2):026108, 2022. 10.1063/5.0078233.

[5] Cindy Albertson and Venki Venkat. Shock interaction control for scramjet cowl leading edges. *AIAA/CIRA 13th International Space Planes and Hypersonics Systems and Technologies Conference*, May 2005. AIAA paper 2005-3289, 10.2514/6.2005-3289.

[6] B. Edney. Anomalous heat transfer and pressure distributions on blunt bodies at hypersonic speeds in the presence of an impinging shock. Technical Report FFA-115, The Aeronautical Research Institute of Sweden (1968).

[7] Catarina Garbacz, Fábio Morgado, and Marco Fossati. Response of shock interaction patterns to different freestream conditions in carbon-dioxide flows over double-wedges. *AIAA AVIATION Forum*, June 2022. AIAA Paper 2022-3277, 10.2514/6.2022-3277.

[8] Carson L. Running, Thomas J. Juliano, Joseph S. Jewell, Matthew P. Borg, and Roger L. Kimmel. Hypersonic shock-wave/boundary-layer interactions on a cone/flare. *Experimental Thermal and Fluid Science*, 109:109911, 2019. 10.1016/j.expthermflusci.2019.109911.

[9] Ahmet Selim Durna, Mohamad El Hajj Ali Barada, and Bayram Celik. Shock interaction mechanisms on a double wedge at Mach 7. *Physics of Fluids*, 28(9):096101, 2016. 10.1063/1.4961571.

[10] D. Vatansever and B. Celik. Unsteady shock interaction mechanisms of high enthalpy reacting flows over double wedges at Mach 7. *Physics of Fluids*, 33(5):056110, 2021. 10.1063/5.0050202.

[11] Gaurav Kumar and Ashoke De. Role of corner flow separation in unsteady dynamics of hypersonic flow over a double wedge geometry. *Physics of Fluids*, 33(3):036109, 2021. 10.1063/5.0040514.

[12] Walter T. Maier, Jacob T. Needels, Catarina Garbacz, Fábio Morgado, Juan J. Alonso, and Marco Fossati. Su2-nemo: An open-source framework for high-mach nonequilibrium multi-species flows. *Aerospace*, 8(7), 2021. 10.3390/aerospace8070193.

[13] Ioannis Nompelis. *Computational study of hypersonic double-cone experiments for code validation*. PhD thesis, The University of Minnesota, 2004.

[14] James B. Scoggins. *Development of numerical methods and study of coupled flow, radiation, and ablation phenomena for atmospheric entry*. PhD thesis, Von Karman Institude for Fluid Dynamics, 2017.

[15] Michael Wright, Karl Edquist, Chun Tang, Brian Hollis, Paul Krasa, and Charles Campbell. A review of aerothermal modeling for mars entry missions. *48th AIAA Aerospace Sciences Meeting Including the New Horizons Forum and Aerospace Exposition*, January 2010. AIAA Paper 2010-443, 10.2514/6.2010-443.

[16] Leonardo C. Scalabrin. *NUMERICAL SIMULATION OF WEAKLY IONIZED HYPERSONIC FLOW OVER REENTRY CAPSULES*. PhD thesis, The University of Michigan, 2007.

[17] Sangdi Gu and Herbert Olivier. Capabilities and limitations of existing hypersonic facilities. *Progress in Aerospace Sciences*, 113:100607, 03 2020. 10.1016/j.paerosci.2020.100607.

[18] A. Swantek. *The role of aerothermochemistry in double cone and double wedge flows*. PhD thesis, University of Illinois, 2012.

[19] T. Hashimoto. Experimental investigation of hypersonic flow induced separation over double wedges. *Journal of Thermal Science*, 18:220–225, 2009. 10.1007/S11630-009-0220-4.

[20] David A. Stewart and Y. K. Chen. Hypersonic convective heat transfer over 140-deg blunt cones in different gases. *Journal of Spacecraft and Rockets*, 31:735–743, 1994. 10.2514/3.26506.

[21] Brian R. Hollis and John N. Perkins. High-enthalpy and perfect-gas heating measurements on a blunt cone. *Journal of Spacecraft and Rockets*, 33(5):628–634, 1996. 10.2514/3.26812.

[22] M. Netterfield, F. Mazoue, L. Marraffa, D. Kastell, and G. Eitelberg. Experiments and computations on a blunt body in a high enthalpy CO_2 flow. 31st Thermophysics Conference, AIAA Paper 96-1804, 1996. 10.2514/6.1996-1804.

[23] C. Wen. *Hypervelocity flow over spheres*. PhD thesis, California Institute of Technology, 1996.

[24] Manu Sharma, Andy Swantek, William Flaherty, Joanna Austin, Sriram Doraiswamy, and Graham Candler. Evaluation of hypervelocity carbon dioxide blunt body experiments in an expansion tube facility. 49th AIAA Aerospace Sciences Meeting including the New Horizons Forum and Aerospace Exposition, AIAA paper 2011-136, 2011. 10.2514/6.2011-136.

[25] S. Gu. *Mars Entry Afterbody Radiative Heating: An Experimental Study of Nonequilibrium CO_2 Expanding Flow*. PhD thesis, The University of Queensland, 2017.

[26] D. Liao, Liu Jik, J. Huang, H. Jian, A. Xie, and Z. Wang. Measurement and numerical simulation of shock standoff distances over hypersonic spheres in CO_2 in a ballistic range. *Shock Waves*, 30, 03 2020. 10.1007/s00193-019-00923-1.

[27] Andrew M. Knisely. *EXPERIMENTAL INVESTIGATION OF NONEQUILIBRIUM AND SEPARATION SCALING IN DOUBLE-WEDGE AND DOUBLE-CONE GEOMETRIES*. PhD thesis, The University of Illinois at Urbana-Champaign, 2016.

[28] J. Urzay. The physical characteristics of hypersonic flows. Technical report, Center for Turbulence Research, Stanford University, Stanford CA 94305, 2020.

[29] C. Windisch, B. U. Reinartz, and S. Müller. Investigation of unsteady Edney type IV and VII shock-shock interactions. *AIAA Journal*, 54(6):1846–1861, 2016. 10.2514/1.J054298.

[30] James B. Scoggins, Vincent Leroy, Georgios Bellas-Chatzigeorgis, Bruno Dias, and Thierry E. Magin. Mutation++: MUlticomponent Thermodynamic And Transport properties for IONized gases in C++. *SoftwareX*, 12:100575, 2020. 10.1016/j.softx.2020.100575.

[31] Catarina Garbacz, Marco Fossati, Walter Maier, Juan J. Alonso, James Scoggins, Thierry Magin, and Thomas D. Economon. Numerical study of shock interference patterns for gas flows with thermal nonequilibrium and finite-rate chemistry. *AIAA Scitech Forum*, January 2020. AIAA Paper 2020-1805, 10.2514/6.2020-1805.

[32] Catarina Garbacz, Fabio Morgado, Marco Fossati, James Scoggins, Thierry Magin, and Michele Capriati. Influence of thermochemical modelling of $CO_2 - N_2$ mixtures on the shock interaction patterns at hypersonic regimes. *AIAA AVIATION Forum*, August 2021. AIAA Paper 2021-2849, 10.2514/6.2021-2849.

[33] C Garbacz, WT Maier, JB Scoggins, TD Economon, T Magin, JJ Alonso, and M Fossati. Shock interactions in inviscid air and CO_2-N_2 flows in thermochemical non-equilibrium. *Shock Waves*, pages 1–15, 2021. 10.1007/s00193-021-00999-8.

[34] Catarina Garbacz, Fábio Morgado, Marco Fossati, Walter T. Maier, Brian C. Munguía, Juan J. Alonso, and Adrien Loseille. Parametric study of nonequilibrium shock interference patterns over a fuselage-and-wing conceptual vehicle. *AIAA Journal*, 59(12):4905–4916, 2021. 10.2514/1.J060470.

[35] Sergey F. Gimelshein, Ingrid J. Wysong, Alexander J. Fangman, Daniil A. Andrienko, Olga V. Kunova, Elena V. Kustova, Catarina Garbacz, Marco Fossati, and Kyle Hanquist. Kinetic and continuum modeling of high-temperature oxygen and nitrogen binary mixtures. *Journal of Thermophysics and Heat Transfer*, 36(2):399–418, 2022. 10.2514/1.T6258.

[36] Sergey F. Gimelshein, Ingrid J. Wysong, Alexander J. Fangman, Daniil A. Andrienko, Olga V. Kunova, Elena V. Kustova, Fabio Morgado, Catarina Garbacz, Marco Fossati, and Kyle M. Hanquist. Kinetic and continuum modeling of high-temperature air relaxation. *Journal of Thermophysics and Heat Transfer*, 36(4):1–23, 2022. 10.2514/1.T6462.

[37] Fábio Morgado, Catarina Garbacz, and Marco Fossati. Impact of anisotropic mesh adaptation on the aerothermodynamics of atmospheric reentry. *AIAA Journal*, 60(7):3973–3989, 2022. 10.2514/1.J061071.

[38] P. Halder, K. P. Sinhamahapatra, and N. Singh. Type-VI and type-V shock-shock interactions on double-wedge geometries using AUSM+ on unstructured grid. *International Journal of Hypersonics*, 1:225–244, 12 2010. 10.1260/1759-3107.1.4.225.

[39] Z. M. Hu, R. S. Myong, Y. R. Yang, and T. H. Cho. Reconsideration of inviscid shock interactions and transition phenomena on double-wedge geometries in a M_∞=9 hypersonic flow. *Theoretical and Computational Fluid Dynamics*, 24(6):551–564, Dec 2010. 10.1007/s00162-010-0188-4.

[40] Prakash Thirunavukkarasu and Shankar Ghosh. *Numerical Simulation of High Temperature Effects on High Enthalpy Flow Over Double Wedge Geometry*. AIAA Scitech 2019 Forum, San Diego, CA, AIAA Paper 2019-1904 (2019). 10.2514/6.2019-1904.

[41] Ozgur Tumuklu, Deborah A. Levin, and Joanna M. Austin. Shock-shock interactions for a double wedge configuration in different gases. *53rd AIAA Aerospace Sciences Meeting*, 2015. 10.2514/6.2015-1520.

[42] Ozgur Tumuklu, Deborah A. Levin, Sergey F. Gimelshein, and Joanna M. Austin. Factors influencing flow steadiness in laminar boundary layer shock interactions. *AIP Conference Proceedings*, 1786(1):050005, 2016. 10.1063/1.4967555.

[43] Giuseppe Pezzella, Donato de Rosa, and R. Donelli. Computational analysis of shock wave boundary layer interactions in non-equilibrium hypersonic flow. 20th AIAA International Space Planes and Hypersonic Systems and Technologies Conference, AIAA Paper 2015-3578 (2015). 10.2514/6.2015-3578.

[44] G. Ben-Dor, E. I. Vasilev, T. Elperin, and A. V. Zenovich. Self-induced oscillations in the shock wave flow pattern formed in a stationary supersonic flow over a double wedge. *Physics of Fluids*, 15(12):L85–L88, 2003. 10.1063/1.1625646.

[45] Dieter Mewes and Franz Mayinger, editors. *Direct Simulation Monte-Carlo (DSMC) Method*, pages 275–315. Springer Berlin Heidelberg, Berlin, Heidelberg, 2005.

[46] E. V. Kustova and E. A. Nagnibeda. State-to-state kinetic theory approach for transport and relaxation processes in viscous reacting gas flows. *AIP Conference Proceedings*, 1333(1):1371–1376, 2011. 10.1063/1.3562834.

[47] G. Tchuen, M. Fogue, Y. Burtschell, D.E. Zeitoun, and G. Ben-Dor. Shock-on-shock interactions over double-wedges: comparison between inviscid, viscous and nonequilibrium hypersonic flow. In Klaus Hannemann and Friedrich Seiler, editors, *Shock Waves*, pages 1497–1502, Berlin, Heidelberg, 2009. Springer Berlin Heidelberg.

[48] G. Tchuen, Y. Burtschell, and D. E. Zeitoun. Numerical study of the interaction of type IVr around a double-wedge in hypersonic flow. *Computers & Fluids*, 50(1):147 – 154, 2011. 10.1016/j.compfluid.2011.07.002.

[49] J. Li, Yujian Zhu, and Xisheng Luo. Thermochemical non-equilibrium effects on type VI-V transition in hypersonic double-wedge flow. In Riccardo Bonazza and Devesh Ranjan, editors, *29th International Symposium on Shock Waves 1*, pages 167–172, Cham, 2015. Springer International Publishing.

[50] Mehrnaz Rouhi Youssefi. Assessment of CFD capability for hypersonic shock wave laminar boundary layer interactions. *Aerospace*, 4:25, 06 2017. 10.3390/aerospace4020025.

[51] Jiaao Hao and Chih-Yung Wen. Effects of vibrational nonequilibrium on hypersonic shock-wave/laminar boundary-layer interactions. *International Communications in Heat and Mass Transfer*, 97:136–142, 2018. 10.1016/j.icheatmasstransfer.2018.07.010.

[52] Amna Khraibut and Sudhir Gai. *Flow Steadiness Over a Double Wedge at Mach 7 Including Effect of Trailing Edge Expansion*. 2018. 10.2514/6.2018-5388.

[53] On the influence of non equilibrium in the free stream conditions of high enthalpy oxygen flows around a double-cone. *Acta Astronautica*, 201:247–258, 2022. https://doi.org/10.1016/j.actaastro.2022.09.017.

[54] Michael E. Holloway, Kyle M. Hanquist, and Iain D. Boyd. Assessment of thermochemistry modeling for hypersonic flow over a double cone. *Journal of Thermophysics and Heat Transfer*, 34(3):538–547, 2020. 10.2514/1.T5792.

[55] Assessment of CFD capability for prediction of hypersonic shock interactions. *Progress in Aerospace Sciences*, 48-49:8–26, 2012.

[56] Graham Candler. Computation of thermo-chemical nonequilibrium martian atmospheric entry flows. 5th Joint Thermophysics and Heat Transfer Conference, AIAA paper 90-1695, 1990. 10.2514/6.1990-1695.

[57] Nikos Mastorakis, Sávio Edisson, and Amílcar Pimenta. Thermochemical non-equilibrium entry flows in mars in three-dimensions - part I - structured solutions. *Advances In Applied And Pure Mathematics*, pages 210–233, 05 2014.

[58] Julien Annaloro and Arnaud Bultel. Vibrational and electronic collisional-radiative model in CO_2-N_2-Ar mixtures for mars entry problems. *Physics of Plasmas*, 26(10):103505, 2019. 10.1063/1.5114792.

[59] Chul Park, John T. Howe, Richard L. Jaffe, and Graham V. Candler. Review of chemical-kinetic problems of future NASA missions, II: Mars entries. *Journal of Thermophysics and Heat Transfer*, 8(1):9–23, 1994. 10.2514/3.496.

[60] E.V. Kustova and E.A. Nagnibeda. On a correct description of a multi-temperature dissociating CO_2 flow. *Chemical Physics*, 321(3):293–310, 2006. 10.1016/j.chemphys.2005.08.026.

[61] E. V. Kustova, E. A. Nagnibeda, Yu. D. Shevelev, and N. G. Syzranova. Non-equilibrium supersonic CO_2 flows with real gas effects near a blunt body. *AIP Conference Proceedings*, 1084(1):831–836, 2008. 10.1063/1.3076591.

[62] Alena Kosareva and E. Nagnibeda. Vibrational-chemical coupling in mixtures CO_2/CO/O and CO_2/CO/O_2/O/C. *Journal of Physics: Conference Series*, 815:012027, 02 2017. 10.1088/1742-6596/815/1/012027.

[63] Alena Kosareva and E. Nagnibeda. Multi-temperature models for shock heated flows of CO_2/CO/O mixture. 7th European Conference for Aeronautics and Aerospace Sciences (EUCASS), 2017. 10.13009/EUCASS2017-222.

[64] Yuriy Shevelev. *Numerical Modeling of Hypersonic Aerodynamics and Heat Transfer Problems of the Martian Descent Modules*. 03 2018. 10.5772/intechopen.71666.

[65] A. A. Kosareva. Non-equilibrium vibrational and chemical kinetics in shock heated carbon dioxide. *AIP Conference Proceedings*, 1959(1):060009, 2018. 10.1063/1.5034670.

[66] E. V. Kustova, E. A. Nagnibeda, Yu. D. Shevelev, and N. G. Syzranova. Non-equilibrium kinetics and transport processes in a hypersonic flow of CO_2/CO/O_2/C/O mixture. *AIP Conference Proceedings*, 1333(1):1227–1232, 2011. 10.1063/1.3562811.

[67] E.V. Kustova and E.A. Nagnibeda. Kinetic model for multi-temperature flows of reacting carbon dioxide mixture. *Chemical Physics*, 398:111–117, 2012. https://doi.org/10.1016/j.chemphys.2011.05.019.

[68] A. A. Kosareva and E. A. Nagnibeda. On the influence of kinetic models on parameters of CO_2/CO/O_2/C/O mixture flows behind shock waves. *AIP Conference Proceedings*, 2132(1):130001, 2019. 10.1063/1.5119621.

[69] Transport properties of a reacting gas mixture with strong vibrational and chemical nonequilibrium. *Chemical Physics*, 233(1):57–75, 1998. https://doi.org/10.1016/S0301-0104(98)00092-5.

[70] I. Armenise and E.V. Kustova. State-to-state models for CO_2 molecules: From the theory to an application to hypersonic boundary layers. *Chemical Physics*, 415:269–281, 2013. https://doi.org/10.1016/j.chemphys.2013.01.034.

[71] E.V. Kustova, E. Nagnibeda, and I. Armenise. Vibrational-chemical kinetics in mars entry problems. *The Open Plasma Physics Journal*, 7:76–87, 06 2014. 10.2174/1876534301407010076.

[72] I. Armenise and E.V. Kustova. On different contributions to the heat flux and diffusion in non-equilibrium flows. *Chemical Physics*, 428:90–104, 2014. https://doi.org/10.1016/j.chemphys.2013.11.003.

[73] Amal Sahai, Bruno Lopez, Christopher Johnston, and Marco Panesi. Novel approach for CO_2 state-to-state modeling and application to multidimensional entry flows. 01 2017. 10.2514/6.2017-0213.

[74] J. D. Anderson Jr. *Hypersonic and High Temperature Gas Dynamics*. American Institute of Aeronautics and Astronautics, Inc., second edition, 2006.

[75] M. Camac. CO_2 relaxation processes in shock waves. *Fundamental Phenomena in Hypersonic Flow*, pages 195–215, Cornell U.P., Ithaca, N.Y. 1966.

[76] E. Kustova, M. Mekhonoshina, and A. Kosareva. Relaxation processes in carbon dioxide. *Physics of Fluids*, 31(4):046104, 2019. 10.1063/1.5093141.

[77] P.A. Gnoffo, R.N. Gupta, and J.L. Shinn. Conservation equations and physical models for hypersonic air flows in thermal and chemical nonequilibrium. page 158, 1989. NASA Technical Paper 2867.

[78] Chul Park. Review of chemical-kinetic problems of future NASA missions. I - earth entries. *Journal of Thermophysics and Heat Transfer*, 7(3):385–398, 1993. 10.2514/3.431.

[79] Iole Armenise, Philippe Reynier, and Elena Kustova. Advanced models for vibrational and chemical kinetics applied to Mars entry aerothermodynamics. *Journal of Thermophysics and Heat Transfer*, 30(4):705–720, 2016. 10.2514/1.T4708.

[80] C. Park. Assessment of two-temperature kinetic model for ionizing air. *Journal of Thermophysics and Heat Transfer*, 3(3):233–244, 1989. 10.2514/3.28771.

[81] L. Landau and E. Teller. *Physik Zeitschrift der Sowjetunion*, 10:34–38, 1936.

[82] R. C. Millikan and D. R. White. Systematics of vibrational relaxation. *The Journal of Chemical Physics*, 39(12):3209–3213, 1963. 10.1063/1.1734182.

[83] J. D. Ramshaw and C. H. Chang. Friction-weighted self-consistent effec- tive binary diffusion approximation. *Journal of Non-Equilibrium Ther- modynamics*, 21(3):223–232, 1996. 10.1515/jnet.1996.21.3.223.

[84] C. R. Wilke. A viscosity equation for gas mixtures. *The Journal of Chemical Physics*, 18(4):517–519, 1950. 10.1063/1.1747673.

[85] Arnold Eucken. Über das wärmeleitvermögen, die spezifische wärme und die innere reibung der gase. *Phys. Z*, 14(8):324–332, 1913.

[86] Meng-Sing Liou and Christopher J. Steffen. A new flux splitting scheme. *Journal of Computational Physics*, 107(1):23–39, 1993. 10.1006/JCPH.1993.1122.

[87] Bram van Leer. Flux-vector splitting for the euler equations. In *Eighth International Conference on Numerical Methods in Fluid Dynamics*, volume 170. Springer, 1982. 10.1007/3-540-11948-5$_6$6.

[88] Chul Park, Richard L. Jaffe, and Harry Partridge. Chemical-kinetic parameters of hyperbolic earth entry. *Journal of Thermophysics and Heat Transfer*, 15(1):76–90, 2001. 10.2514/2.6582.

[89] Ji Li, Yujian Zhu, and Xisheng Luo. On type VI-V transition in hypersonic double-wedge flows with thermo-chemical non-equilibrium effects. *Physics of Fluids*, 26(8):086104, 2014. 10.1063/1.4892819.

[90] A. S. Durna and B. Celik. Effects of double-wedge aft angle on hypersonic laminar flows. *AIAA Journal*, 58(4):1689–1703, 2020. 10.2514/1.J058754.

[91] T. D. Economon, F. Palacios, S. R. Copeland, T. W. Lukaczyk, and J. J. Alonso. SU2: An open-source suite for multiphysics simulation and design. *AIAA Journal*, 54(3):828–846, 2016. 10.2514/1.J053813.

[92] F. Palacios, S. Copeland, A. Lonkar, and J. Alonso. Adjoint-based goal-oriented mesh adaptation for nonequilibrium hypersonic flows. *51st AIAA Aerospace Sciences Meeting including the New Horizons Forum and Aerospace Exposition 2013*, 01 AIAA Paper 2013-0552, 2013. 10.2514/6.2013-552.

[93] Walter T. Maier, Jacob T. Needels, Juan J. Alonso, Fábio Morgado, Catarina Garbacz, Fábio Morgado, Marco Fossati, Ozgur Tumuklu, and Kyle Hanquist. Development of physical and numerical nonequilibrium modeling capabilities within the SU2-NEMO code. *AIAA AVIATION Forum*, June 2023. AIAA Paper 2023-3488, 10.2514/6.2023-3488.

[94] A. Loseille and R. Loehner. Boundary layer mesh generation and adaptivity. 2011. 10.2514/6.2011-894.

[95] Adrien Loseille and Victorien Menier. Serial and parallel mesh modification through a unique cavity-based primitive. In Josep Sarrate and Matthew Staten, editors, *Proceedings of the 22nd International Meshing Roundtable*, pages 541–558, Cham, 2014. Springer International Publishing. 10.1007/978-3-319-02335-9$_3$0.

[96] Adrien Loseille, Victorien Menier, and Frédéric Alauzet. Parallel generation of large-size adapted meshes. *Procedia Engineering*, 124:57 – 69, 2015. 24th International Meshing Roundtable.

[97] Adrien Loseille. Unstructured mesh generation and adaptation. In Rémi Abgrall and Chi-Wang Shu, editors, *Handbook of Numerical Methods for Hyperbolic Problems - Applied and Modern Issues*, pages 263–302. Elsevier, 2017. 10.1016/bs.hna.2016.10.004.

[98] M-G Vallet, C-M Manole, Julien Dompierre, S Dufour, and François Guibault. Numerical comparison of some hessian recovery techniques. *International Journal for Numerical Methods in Engineering*, 72(8):987–1007, 2007.

[99] Loic Frazza. *3D anisotropic mesh adaptation for Reynolds Averaged Navier-Stokes simulations.* PhD thesis, 2018.

[100] Iain D. Boyd and Eswar Josyula. State resolved vibrational relaxation modeling for strongly nonequilibrium flows. *Physics of Fluids*, 23(5):057101, 2011. 10.1063/1.3584128.

[101] Thomas J. Scanlon, Craig White, Matthew K. Borg, Rodrigo C. Palharini, Erin Farbar, Iain D. Boyd, Jason M. Reese, and Richard E. Brown. Open-source direct simulation monte carlo chemistry modeling for hypersonic flows. *AIAA Journal*, 53(6):1670–1680, 2015. 10.2514/1.J053370.

[102] Leonardo C. Scalabrin. *Numerical Simulation of Weakly Ionized Hypersonic Flow over Reentry Capsules*. PhD thesis, University of Michigan, 2007.

[103] Sergey F. Gimelshein, Ingrid J. Wysong, Alexander J. Fangman, Daniil A. Andrienko, Olga V. Kunova, Elena V. Kustova, Catarina Garbacz, Marco Fossati, and Kyle Hanquist. Kinetic and continuum modeling of high temperature relaxation of O_2 and N_2 binary mixtures. *Journal of Thermophysics and Heat Transfer (preprint - under review).*

[104] Doyle Knight, José Longo, Dimitris Drikakis, Datta Gaitonde, Andrea Lani, Ioannis Nompelis, Bodo Reimann, and Louis Walpot. Assessment of CFD capability for prediction of hypersonic shock interactions. *Progress in Aerospace Sciences*, 48-49:8–26, 2012. Assessment of Aerothermodynamic Flight Prediction Tools.

[105] Sebastian Karl, Jan Martinez Schramm, and Klaus Hannemann. High enthalpy cylinder flow in heg: A basis for CFD validation. In *33rd AIAA Fluid Dynamics Conference and Exhibit*, page 4252, 2003. 10.2514/6.2003-4252.

[106] Marvin I. Kussoy and Clifford C. Horstman. Documentation of two- and three-dimensional hypersonic shock wave/turbulent boundary layer interaction flows. Technical Report 19890010729, National Aeronautics and Space Administration, 1989.

[107] Nicholas J. Georgiadis, Christopher L. Rumsey, and George P. Huang. Revisiting turbulence model validation for high-mach number axisymmetric compression corner flows. In *53rd AIAA Aerospace Sciences Meeting*, page 0316, 2015. AIAA paper 2015-03, 10.2514/6.2015-0316.

[108] Nicholas Georgiadis, Dennis Yoder, Charles Towne, William Engblom, V. Bhagwandin, Dennis Lankford, G. Power, and Chris Nelson. *Wind-US Code Physical Modeling Improvements to Complement Hypersonic Testing and Evaluation*. 10.2514/6.2009-193.

[109] Satoru Yamamoto, Norinao Takasu, and Hideo Nagatomo. Numerical investigation of shock/vortex interaction in hypersonic thermochemical nonequilibrium flow. *Journal of Spacecraft and Rockets*, 36(2):240–246, 1999. 10.2514/2.3438.

[110] S. Laurence, R. Deiterding, and H. Hornung. Proximal bodies in hypersonic flow. *Journal of Fluid Mechanics*, 590:209 – 237, 2007. 10.1017/S0022112007007987.

[111] Ali Gülhan Sebastian Willems, Patrick Seltner. Shock-shock interaction test case. *ESA ATD3 Workshop*, 2018.

[112] Guillaume Grossir, Daniela Puorto, Zdeněk Ilich, S. Paris, Olivier Chazot, Sébastien Rumeau, Martin Spel, and Julien Annaloro. Aerodynamic characterization of space debris in the VKI longshot hypersonic tunnel using a free-flight measurement technique. *Experiments in Fluids*, 61, 06 2020. 10.1007/s00348-020-02995-7.

[113] Fabio Morgado, Sai Abhishek Peddakotla, Julie Graham, Massimiliano Vasile, and Marco Fossati. A multi-fidelity framework for aerothermodynamic modelling and simulation of destructive atmospheric entry. *AIAA Journal*, 2024. Accepted for publication.

[114] J. Pike. Wind tunnel tests on six wing-body models at M=4. Technical report, Aeronautical Research Council. ARC/CP-1074, 1969.

[115] H. G. Hornung and G. H. Smith. The influence of relaxation on shock detachment. *Journal of Fluid Mechanics*, 93(2):225–239, 1979. 10.1017/S0022112079001865.

[116] Schexnayder Jr. C.J. Evans, J.S and W.L. Grose. Effects of nonequilibrium ablation chemistry on viking radio blackout. *Journal of Spacecraft and Rockets*, 11(2):84–88, 1974. doi.org/10.2514/3.62013.

[117] Michael J. Wright, Graham V. Candler, and Deepak Bose. Data-parallel line relaxation method for the navier-stokes equations. *AIAA Journal*, 36(9):1603–1609, 1998. 10.2514/2.586.